New Phase Transition Mechanisms in Compressed Silica

A Thesis submitted in partial fulfillment of the requirements for the degree of Doctor of Philosophy at George Mason University

by

Qingyang Hu
Master of Science
George Mason University, 2014

Director: Howard Sheng, Associate Professor
School of Physics, Astronomy and Computational Science

Fall Semester 2014
George Mason University
Fairfax, VA

ACKNOWLEDGEMENTS

I am indebted to my thesis advisor, Prof. Howard Sheng for his guidance, support and training I have received during my dissertation research. I would also like to sincerely thank my friends, Adam Cadien, Alex Koufos and Dr. Weixiao Ji, for their encouragement and help in completing my research.

I would further like to acknowledge valuable discussions and insights I have received from my predoctoral fellowship advisor, Dr. Ho-kwang Mao at the Geophysical Laboratory, Carnegie Institution of Washington. I greatly appreciate the help I have received from Dr. Jinfu Shu, Dr. Wenge Yang, Dr. Xujie Lü, Dr. Li Zhang, Dr. Huiyang Gou and Dr. Zhenling Yang at the Carnegie Institution of Washington, for helping me carry out my experiments and analyze experimental data.

I am grateful to the members of my dissertation committee, Dr. Estela Blaisten-Barojas, Dr. Dimitrios A. Papaconstantopoulos, Dr. Fernando E. Camelli and Dr. Maria Emelianenko for their valuable comments and willingness to carefully read the thesis.

The research described in this dissertation was sponsored in part through the grant No. DMR-0907325 with the National Science Foundation. The work at Carnegie Institution of Washington was sponsored by EFree, an Energy Frontier Research Center funded by the U.S. Department of Energy, Office of Science, Office of Basic Energy Sciences under Award Number DE-SC0001057.

TABLE OF CONTENTS

Page

LIST OF TABLES

LIST OF FIGURES

LIST OF ABBREVIATIONS

Gigapascal ..... GPa
X-ray Diffraction ..... XRD
Pressure Induced Amorphziation ..... PIA
Density Functional Theory ..... DFT
Molecular Dynamics ..... MD
Diamond Anvil Cells ..... DAC
Weight percent ..... wt %
kilobar ..... kbar
Long Range Translational Order ..... LRO
Beest, Kramer and van Santen ..... BKS
Self-Consistent Field ..... SCF
Local Density Approximation ..... LDA
Generalized Gradient Approximation ..... GGA
Becke exchange functional and the Lee-Yang-Parr correlation functional ..... BLYP
Projector Augmented-wave ..... PAW
Car-Parrinello ..... CP
Nudged Elastic Band ..... NEB
Collective variable CV
Minimum-Energy Path ..... MEP
Vienna Ab Initio Simulation Package ..... VASP
Transition States Tools VASP ..... VTST
Density Functional Perturbation Theory ..... DFPT

ABSTRACT

NEW PHASE TRANSITION MECHANISMS IN COMPRESSED SILICA

Qingyang Hu, Ph.D

George Mason University, 2014

Dissertation Director: Dr. Howard Sheng

Silicon dioxide, also known as silica, is a fundamental constituent of the Earth interior. Silica exists in many crystal structures, but with the same chemical composition. These crystal forms are termed as silica polymorphs. Phase transitions among silica polymorphs have long been a focus of theoretical and experimental pursuits, for their great significance in geophysics and materials science. Pressure alters the atomic arrangements through phase transformations and establishes a new dimension in the phase diagrams of many compounds. Pressurizing silica to extreme conditions, *e.g.*, up to several tens of gigapascals (GPa), not only helps discover new silica phases that are stable in deep Earth, but also sheds new light on the elusive densification mechanism of this rudimentary oxide material.

This thesis focuses on pressure-induced behavior of compressed silica at room temperature (*i.e.*, 300 K), with an emphasis on two silica polymorphs: coesite and α-

quartz. To this end, extensive experimental and computational efforts have been undertaken in this thesis, aiming to tackle two major unsolved issues in this area: the nature of the phase transition between different silica polymorphs and the general densification mechanism of silica-like materials.

The theoretical research in this thesis employs state-of-the-art first-principles computational calculations, combining *in situ* synchrotron radiation experiments, to characterize silica solids under high pressure. The combined theoretic and experimental treatment has been tested on a variety of compressed solid systems previously and is found powerful in solving a number of puzzles pertaining to the phase behavior of silica. The main research results are summarized as follows:

a) Compressing single-crystal coesite SiO_2 under hydrostatic pressures of 26~53 gigapascal (GPa) at room temperature, a new polymorphic phase transition mechanism is discovered by means of single-crystal synchrotron X-ray diffraction (XRD) experiment and first-principles computational modeling. The transition features the formation of multiple previously unknown triclinic phases of SiO_2 on the transition pathway as structural intermediates, which eventually transforms into the monoclinic post-stishovite phase. The metastable phases are similar in volume and degenerate in free-energy, but distinct in structures and X-ray diffraction patterns. Coexistence of the low-symmetry phases results in extensive splitting of the original coesite x-ray diffraction peaks that appear with dramatic peak broadening and weakening, thus resembling an amorphous material. Also discovered is the long-sought but never confirmed Si in five-coordination

populated in the metastable phases. This work provides new insights into the structural transition of SiO_2 crystal under high pressures, and clarifies the issue of the pressure-induced amorphization (PIA) of coesite, which has often been cited as an archetypal example of the PIA phenomena in general.

b) The second part of my thesis is centered on the phase transition of compressed α-quartz. Two competing transition pathways of α-quartz under high pressure are uncovered, being reconstructive *vis-à-vis* displacive in their respective nature, toward different new phases. By means of *in situ* single-crystal X-ray diffraction experiment (0-60 GPa) in conjunction with advanced *ab initio* modeling, I demonstrate that, under quasi-static compression conditions at room temperature, compressed α-quartz transits via an intermediate metastable phase (quartz II) emerging at 26 GPa *en route* to a new monoclinic-type post-stishovite structure. Under conditions where this thermally activated transition is kinetically frustrated, it is found that the ultimate stability of α-quartz is controlled by its phonon instability, constituting alternatively a displacive transition mechanism of α-quartz into a new post-quartz phase. The discovery of the two competing transition pathways, achievable at the same pressure range but under different kinetic conditions, puts into perspective of previously seemingly discordant results of compressed α-quartz, and helps clarify the role of phonon softening played in phase transition, paving way to understanding the complex phase behavior of a vast silicate family in geologically important conditions.

This thesis makes contributions to the fundamental understanding of the phase transition

mechanisms of silica. Since silica is considered as an archetypal compound in studying tetrahedrally bonded materials such as silicates as well as other silica-like materials, this thesis work has far-reaching implications to many branches of materials science and geophysics.

The thesis is structured as follows. In Chapter II, I give a brief outline to the various crystalline structures of silica and describe the general concepts in its pressure-induced behaviors. A short discussion about the computational approaches to model the pressure effects of silica is followed, based on the literature as well as my own studies. In Chapter III an introduction of the theoretical background that serves as the foundation of my simulations and experiments is illustrated. The basics of the density functional theory (DFT) and how it is incorporated into modern supercomputing are recapitulated. This chapter also covers the basics of first-principles molecular dynamics (MD), and the use of barrier-crossing algorithms and lattice dynamics to investigate the dynamical properties associated with silica phase transitions. On the experimental side, a review of structural characterization methods utilized in this thesis, *e.g.*, X-ray diffraction techniques and the high pressure loading instrument - the diamond anvil cell (DAC), are provided at the end of the chapter.

Having introduced the preliminaries in Chapters II and III, the original contributions of the thesis are presented. The pressure-induced behavior of coesite is dealt with in Chapter IV, where the technical details and results from my experimental and computational

research are illustrated. Chapter V is dedicated to the description of the competing transition pathways in α-quartz, where a comprehensive study on the pressure-dependent X-ray diffraction spectrum, equation-of-state, lattice dynamics simulation and first-principles MD with barrier crossing algorithms is presented.

I. INTRODUCTION

Pressure alters the physical and chemistry properties of materials and allows phase transitions to occur that defy much of our understandings under the ambient condition[1-3]. One of the archetypal compounds used for high pressure research is silicon-dioxide[4,5], which builds up 50 weight percent (wt %) of Earth's bulk based on the chondritic model and exhibits complicated phase transitions under a variety of pressure and temperature conditions[6-12]. The efforts in interpreting the nature of silica phase transition not only provide a densification mechanism for this fundamental compound, but also have universal significance in interpreting the phase transition of many other oxide materials. From a different perspective, the driving force for the intense study of the pressure-induced behavior of silica also arises from its important role in explaining global plate movement, which is one of the major thrusts in geophysics and materials science.

In this chapter, I will begin with a brief introduction to the structures of reported SiO_2 polymorphs, followed by a summary of previous findings and problems encountered in the studies of the pressure effect of silica. I will also provide an overview about computational modeling methods to deal with such problems.

1.1 A review of silica structures

Materials in the solid state can exist in either the crystalline or the amorphous form.

A crystal is a solid whose atoms are arranged in an ordered pattern well-defined by its long-range translational order (LRO). In contrast, an amorphous solid lacks LRO and atomic packing thereof is disordered. According to thermodynamic laws, crystals are stable phases in nature. The formation of amorphous solids, however, is usually a kinetically driven process under non-equilibrium formation conditions. For instance, the conventional route to form an amorphous solid involves melt liquid-quenching, where the liquid vitrifies into a glass (*i.e.*, an amorphous solid) due to insufficient relaxation time to form a crystal.

1.1.1 SiO_2 phase diagram

As a dominant constituent of the Earth's crust and mantle and a ubiquitous technological material with an extremely wide range of applications, the structure varieties of silica are of great interest to the broad audience of materials science.

Silica exists in many crystalline forms as well as the amorphous form. These minerals have different structures, different symmetry and different physical properties, *etc.*, but all with one same composition - SiO_2. A brief phase diagram[13] showing the variety of silica polymorphs under 12 GPa is given in Fig. 1.1, where at least six silica polymorphs have been confirmed by both experiments and simulations[14-17].

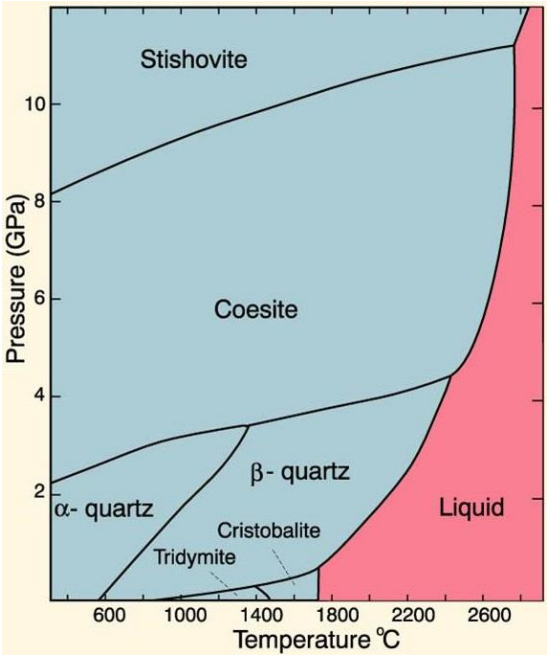

Figure 1.1. Pressure-temperature phase diagram of silica up to 12 GPa. The phase boundaries are based on the work by Swamy *et al.*[13].

1.1.2 Four-coordinated silica structures

Among those silica polymorphs, the ambient silica α-quartz naturally exists in many mines, known as the Tripoli or powder quartz. It has a trigonal crystal system (space group $P3_121$) with 9 atoms (3 silicon and 6 oxygen atoms) in one unit cell. Three corner-linked Si-O tetrahedra signify the structure, each of which is made of one center silicon atom, surrounded by four oxygen atoms (Fig. 1.2). α-quartz is very stable at ambient condition until the pressure is raised to 35 kilobar (kbar) at 1050 K, where the first high-pressure polymorph of silica was synthesized, named after the chemist Loring Coes. Jr. in 1953[14].

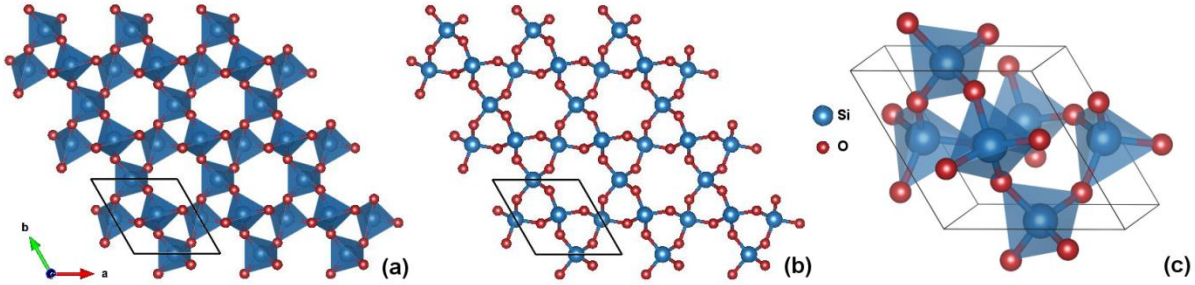

Figure 1.2. Structural representations of α-quartz at ambient conditions: (a) with Si-O polyhedra. (b) viewed in a ball-stick model. (c) A 3-dimensional view for one unit cell. The black box indicates one α-quartz unit cell.

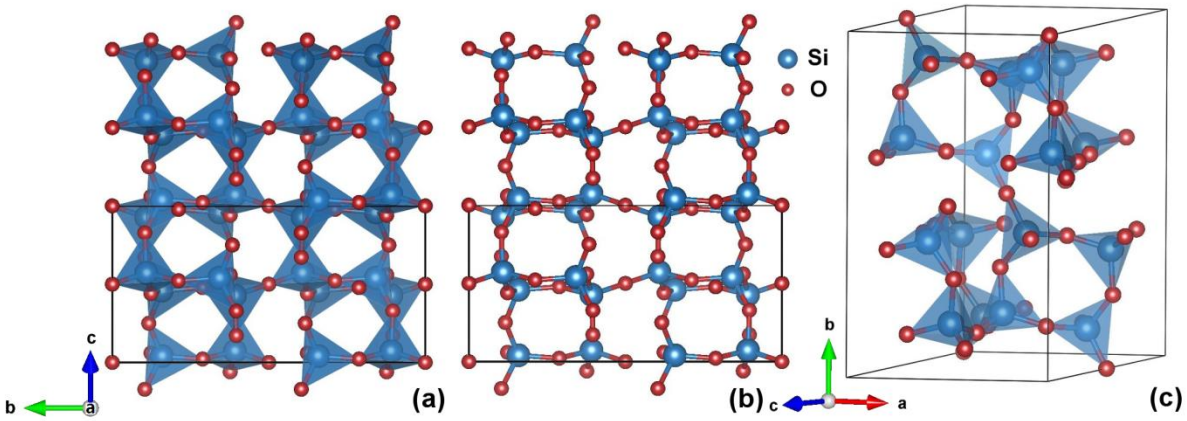

Figure 1.3. Structural representations of coesite at ambient conditions: (a) Si-O polyhedra. (b) viewed in the ball-stick model. (c) A 3-dimensional view for one unit cell. The black box sketches out one coesite unit cell.

Coesite has a monoclinic structure (space group C2/c) with a greater size unit cell, where 16 pairs of SiO_2 unit (48 atoms) are packed in one unit cell, built with corner-sharing tetrahedra rings. It has a unique 4-member-ring structure, distinguishing it from

the 6-member-ring structure of α-quartz (Fig. 1.3). Both α-quartz and coesite have great densification potential since their silicon atoms are in low chemical coordination. Therefore α-quartz and coesite are chosen as the main silica candidates in my thesis.

1.1.3 Highly coordinated silica structures.

The Si-O tetrahedral structure is unstable at high pressure and has a tendency to transform into the six-coordinated octahedral structure[15-20]. While many packing forms of silica octahedra are theoretically available, three of them (see Fig. 1.4a-c) are most cited as they are reported stable at individual pressure ranges[8,12,15]. Stishovite[15] is the first reported six-coordinated silica polymorph with space group $P4_2/mnm$. The layered octahedra unit cell contains six oxygen atoms and exists as the stable SiO_2 form in lower mantle regime. At center mantle pressure, two six-folded silica polymorphs, known as the $CaCl_2$-type[8] (space group Pnnm) and the α-PbO_2-type[12] (space group Pbcn) post-stishovite are mentioned in the literature. The polyhedra representations in Fig. 1.4bc show how the edge-sharing octahedra chains form along the *c*-axis of the high-pressure silica polymorphs.

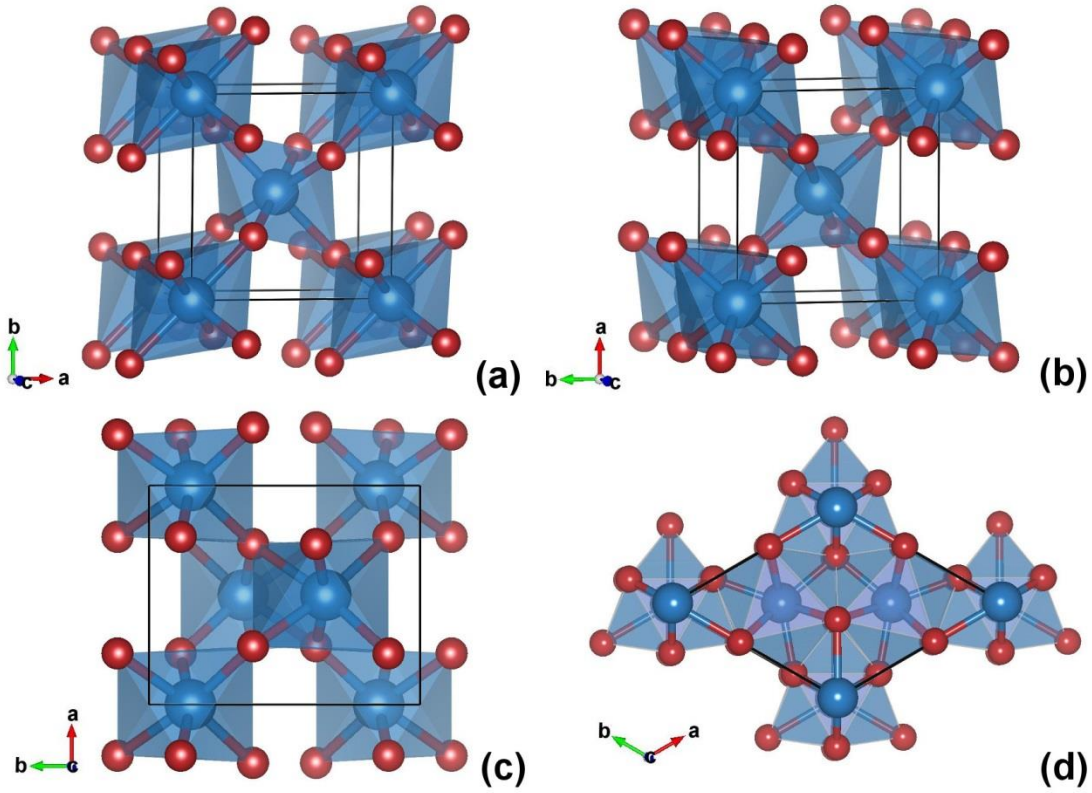

Figure 1.4. Structural representations of various high-pressure silica polymorphs: (a) stishovite at 10 GPa. (b) $CaCl_2$-type post-stishovite at 63 GPa. (c) α-PbO_2-type post-stishovite at 40 GPa. (d) Fe_2P silica at 700 GPa from simulations.

Four silica units at the corner of $CaCl_2$-type post-stishovite create a straight octahedra chain. While in the α-PbO_2-type post-stishovite, two octahedra in the center of the unit cell completes in a zigzag ABAB stacking. Beyond Earth core pressures (*e.g.* in deep interiors of Jupiter), computational simulation predicts that the hexagonal Fe_2P type (Fig. 1.4d) is the stable silica form above 700 GPa[11], where the silicon atoms are coordinated with 9 oxygen atoms. The space group is P62m and 9 atoms (3 Si + 6 O) are closely packed in one unit cell.

1.1.4 Silica samples studied in this thesis

In short, a plethora of crystal structures exhibit in the SiO_2 system at different pressure and temperature conditions[8,11-15]. Although the crystal structures of silica high-pressure polymorphs have been subject to extensive research in the past, exactly how four-coordinated silica transforms under high pressure has not been clearly understood[5,6,10]. It motivated us to investigate two major silica polymorphs: α-quartz and coesite, and to revisit their phase transitions at room temperature and study the transition mechanism from four Si-O coordinated to six-coordinated silica polymorphs.

1.2 Pressure-induced behaviors of silica

1.2.1 Pressure-induced amorphization: the history

One of the challenges in the high-pressure research of silica is its phase transition to an amorphous state upon compression. Besides quenching from melts, there have been tremendous scientific interests in such a novel phase transition in which a crystal directly transforms into a glass *in the solid state*, termed as solid-state amorphization[20]. The pressure-induced amorphization (PIA) – referring to the transition from crystal to glass driven by high pressure conditions was first discovered in ice by Mishima *et al.*[22]. In his research, the diffraction pattern of crystalline ice was greatly smoothed and weakened at liquid nitrogen temperature (77K) and 220 kbar pressure, indicating the loss of LRO in ice I_h. The same phenomenon was confirmed by Strässle *et al.* in his neutron diffraction study (see Fig. 1.5), where the amorphization was shown by the evolution of neutron diffraction patterns in compressed ice[23]. The discovery of PIA in ice opened up a new era

in high pressure research. Studies on PIA were soon extended to numerous other materials[24], including silicate minerals[25-30], other organic[31-33] and inorganic materials[34-44].

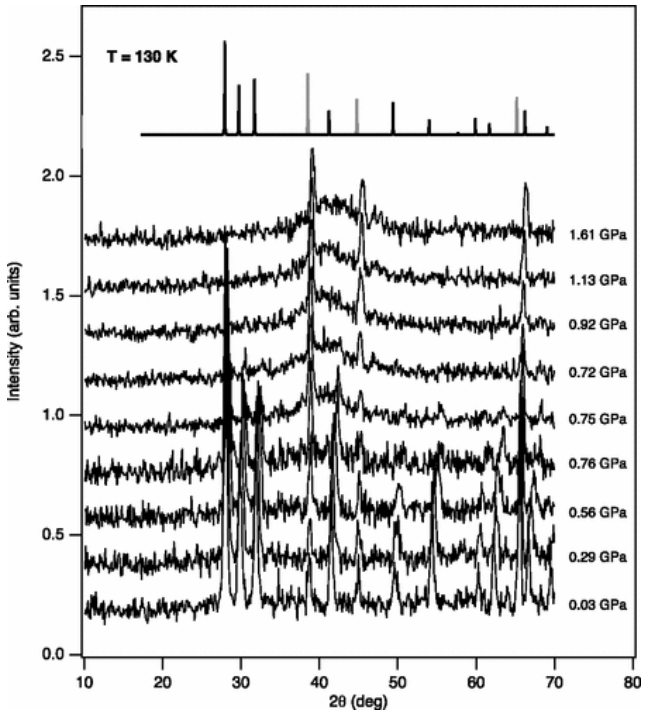

Figure 1.5. Neutron diffraction patterns showing the gradual amorphization of ice I_h phase with increasing pressure at 130 K. Patterns are compared with calculated peaks position in upper figure. (Figure is taken from ref. 22)

1.2.2 Historic research work on α-quartz

The PIA phenomenon complicates our understanding on the phase transition of compressed silica. At room temperature, pioneering energy-dispersive X-ray diffraction studies of compressed polycrystalline α-quartz showed it collapses to an *amorphous*

structure above 25 GPa[24]. In the same paper, the high pressure polymorph of silica – coesite also exhibits amorphization around 30 GPa. Both PIA phenomena were observed in powder silica samples, where the halos on the diffraction patterns disappeared. In the discussions of small thermal activation[24], the amorphization was reasoned to originate from the elastic instability on the crystal potential surface.

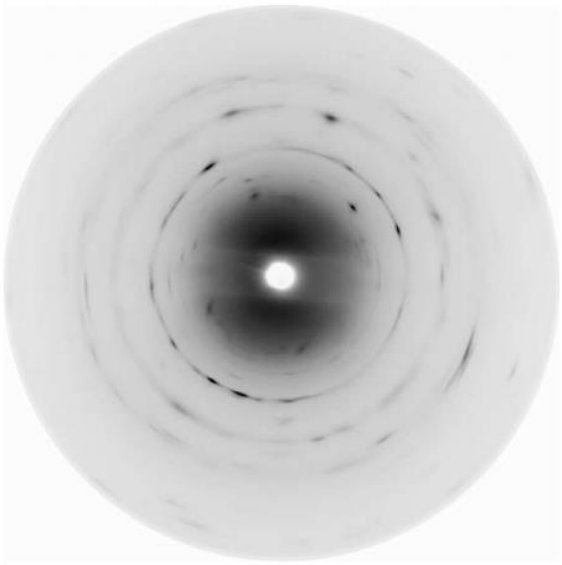

Figure 1.6. X-ray diffraction pattern of the $P2_1/c$ type monoclinic post-quartz at 45 GPa. The figure is taken from ref. 10.

However, ensuing experiments on α-quartz renewed our understanding on the established PIA phenomenon. Slow compression experiments carried out by Tsuchida and Yagi revealed that quartz transformed into poorly crystalized stishovite at 60 GPa[6]. The pressure range surpassed the PIA pressure by ~30 GPa and suggested a crystalline type

phase transition can occur at room temperature. At 22 GPa, Kingma *et al.* found additional diffraction peaks appeared, coexisting with low-quartz peaks[45]. Named as the quartz II phase in her paper, the new silica phase later discovered has the C2 space group and has alternating layers of silicon tetrahedra and octahedra[46,47]. A similar observation was confirmed by Haines *et al.*, who also compressed α-quartz to 45 GPa and found the coexistence of quartz II and a new monoclinic silica phase[10] (see the powder diffraction pattern in Fig. 1.6). In his paper, the so-called post-quartz phase has 6 SiO_2 units in the unit cell and it was suggested that a hydrostatic experimental condition is very important to the observed phase transition.

No sooner after the discovery of PIA in experiment, Binggeli[48] *et al.* employed first-principles simulation and found a geometrically optimized silica polymorph above 60 GPa. The oxygen atoms in this structure have a b.c.c. like sublattice and the silicon atoms can either occupy the tetrahedral or the octahedral sites. Mechanism-wise, they claimed the PIA in α-quartz is due to the elastic instability raised from phonon mode softening at the K point in the Brillouin zone at 19 GPa by pair potentials[49-51] and 32 GPa from *ab initio* calculations[52] (A phonon, or a quasiparticle, represents an excited state in the quantum mechanical quantization of the modes of vibration of elastic structure of interacting particles). By following the evolution of elastic moduli as a function of pressure, Tse *et al.* [53] also explained that PIA in quartz is due to mechanical instability in the crystal. Later on, Dean and co-workers suggested that the silicon atoms could be easily displaced from tetrahedral sites to octahedral sites at high pressure[54].

Aside from static calculations, molecular dynamics with first-principles schemes

revealed that silica densification followed a two-step mechanism and the amorphization observed in experiment was interpreted as a result of the large shear stress on silica unit cells[16,55]. The two-stage mechanism confirmed that the formation of the previously reported b.c.c like sublattice[48] is controlled by the strong repulsion between large oxygen anion, and the cations redistribute into the newly created interstices, leading to an abrupt coordination change.

The exact structure of the quartz II phase has been long sought in the studies of silica. By annealing α-quartz from a major phonon instability in first-principles molecular dynamics, Wentzcovich *et al.* produced a combined edge-sharing octahedra and five-coordinated cuboid silica phase[56]. Later studies employing pair potential models suggested a C2 structure of quartz II, in which silicon tetrahedra link silicon octahedra layers[46,47]. In 2006, studied with the metadynamics approach, the quartz II phase was reported to feature 3×2 octahedra chains[57]. It is worthwhile to note that by implementing such a barrier-crossing algorithm, Martoňák *et al.* suggested α-quartz actually proceeds with a direct crystalline transition into the stishovite structure at 15 GPa[57,58]. Such a crystalline phase transition contradicts with early X-ray diffraction experiments[24]. Nonetheless, it suggests that the phase transition in compressed quartz be a more complicated process than the previously observed amorphization.

1.2.3 Compression experiments on coesite and simulations

Angel *et al.*[59] revealed an anomalous compression mechanism in compressing single-crystal coesite under 11 GPa, where the second derivatives of bulk moduli exhibit an initial softening with increasing pressure. Later researches also showed that the five

Si-O-Si angles continue to decrease upon compression, leading to the rotation of silicon polyhedra[60]. At higher pressures, compressed coesite lost its XRD signals and became an amorphization-like structure above 30 GPa[24]. By examining the microstructure under electric microscope and Raman spectrometry, Kingma *et al.* [28] predicted that some degree of atomic packing ordering was still kept in the amorphized structure. However, such ordering was unable to be explicitly observed experimentally or simulated at that time. Until recently, Cernok *et al.* [61]suggested compressed coesite actually transforms into a crystalline phase at 34 GPa, although the exact atomic structure was not shown.

From first-principles MD with the metadynamics algorithm, coesite was shown to transform into an α-PbO_2-type post-stishovite structure at 22 GPa and 600 K[57,58], where a small energy barrier (0.18 *a.u.*/SiO_2 unit) was overcome. In the evolution of the transition, six-coordinated octahedra gradually take form and the *b*-axis was predicted as the most compressible axis (Fig. 1.7).

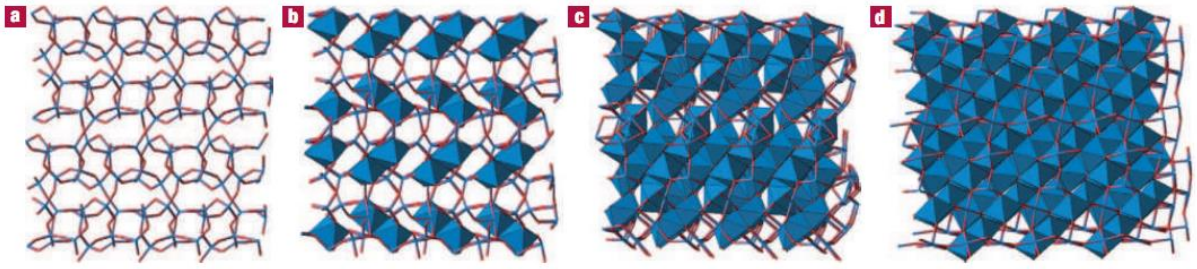

Figure 1.7. Phase transition from coesite to α-PbO_2-type post-stishovite. Structural evolution during the transition from coesite (a) to the α-PbO_2-type post-stishovite (d). Intermediate states (b) and (c) show the initial growth and competition of chains of octahedra in different planes. The figure is taken from ref. 57.

The new post-stishovite structure has an edge-sharing octahedra structure and the new lattice was reported to form with preferred layering on the (120) plane. The lattice was suggested to be reconstructed since the resultant phase has no topological relationship with its parent phase. Despite the scarcity of experimental evidence, these theoretical works hint at a new transition mechanism different than the PIA in compressed coesite.

Comprehensively, the interpretation of PIA evolves with the applications of new experimental techniques, especially the application of advanced structural characterization techniques (*e.g.* synchrotron radiation), pressurization instrumentation (*e.g.* diamond anvil cells[62]), electronic microscopy techniques[63-65] and faster supercomputers. Therefore I am motivated to employ state-of-the-art experimental and theoretical techniques to uncover the underlying phase transition mechanism of coesite in this thesis.

1.2.4 An outstanding question: Is PIA real?

Though many experiments and simulations have been carried out in the last decade, the mystery of PIA in silica still persists as the exact structural nature of the *amorphous* or *amorphous-like* phase is not known. There is much renewed interest in revisiting the phase transition in silica, which is the main driving force of the thesis.

I propose a new transition mechanism in this thesis, in an effort to clarify the long-standing mystery of PIA in silica. Compressed silica at room temperature actually transforms into metastable states, *en route* to their high-pressure structures. Those metastable structures usually have topotaxial relationships with the parent silica crystal

and serves as the transition intermediates bridging the phases with different silicon coordination numbers. The metastable crystalline phases of silica could be equally important and more intriguing than the stable crystalline phases. High pressure and low temperature create conditions that favor the denser packing from 4- to 5- to 6-coordination[66,67] while hinder the true equilibrium and preserve metastable intermediate states. Therefore the possibility of the formation of a fully disordered phase must be reputed because it lacks long-distance atomic diffusion[28], advocating that a portion of crystal ordering should still be present. In general, previous results from both experimental and computational works indicate the nature of the formation of the intermediate phase is still puzzling and plentiful details remain to be uncovered. Herein lies the motivation for optimizing the experimental protocol as well as mapping out the energy landscape with advanced simulation techniques to uncover the true phase transition mechanism of silica.

1.3 Modeling the Si-O system

Modeling the Si-O force field for computational simulation is a long-pursued objective in computational science. An ideal potential model should include: a) Robust computational accuracy at any position on the phase diagram. b) Fast and well parallel scaled computing speed, supporting massive simulation comparable to macroscopic systems. While the first objective is achieved by first-principles theories, it is on the cost of much computational power and the size of the simulation system is restricted to hundreds of atoms. On the other hand, although empirical potential models are still far from perfect, they can afford the simulation of millions of atoms in millisecond time scale.

In this section, I will review the potential models in history based on their applicability of silica systems. By comparing the results under different settings, I seek to employ the most appropriate methods for my computational research on high-pressure silica.

1.3.1 Pair potentials

Empirical interatomic potentials were popular in the 1990s. For instance, Lasaga *et al.*[68] developed a pair-potential force field for silica from *ab initio* calculations, which enabled large-scale computer simulation. Though a plethora of other potentials have been published[69,70], the most successful and widely used semi-empirical model is probably the one established by van Beest, Kramer and van Santen (BKS)[71]. The BKS model could predict reasonable silica structural changes at low to medium pressures range (up to ~25 GPa). Studies based on the BKS model showed quartz transforms into an amorphous phase at 21 GPa[72]. Recently the BKS model was proved to be appropriate in predicting the high temperature phase transition of silica[73] and shockwave compression[74].

It is worth noting that, pair potentials due to their empirical nature may lead to unphysical behaviors. One caveat about the BKS model is that its validity for phase transitions in the transition boundaries and high-pressure regime has not yet to be confirmed. In Fig. 1.8, the BKS model predicts a phase boundary between coesite and the anatase-type silica at around 26 kbar (corresponds to 28 $Å^3/SiO_2$ unit in volume in Fig. 1.8). However, both experiments[5,45] and first-principles simulations[44] failed to support the existence of such a silica phase at the predicted pressure range. The artificial stability of the anatase-type silica phase therefore represents a so far unknown artifact of the BKS model.

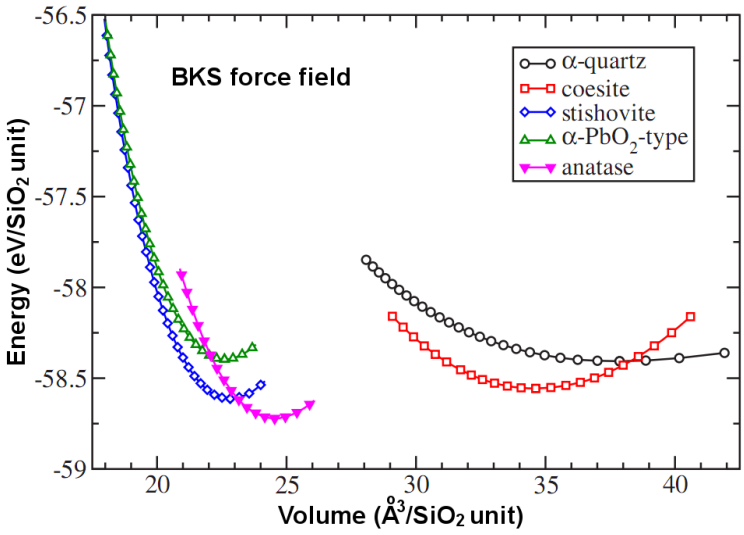

Figure 1.8. Equations of state of various silica polymorphs from BKS force field calculations (results taken from ref. 58). The predicted anatase-type silica phase contradicts with first-principles calculations[44] and experiments[5,45].

1.3.2 First-principles methods

Hence, correct prediction of the phase behavior of the materials and accurate assessments of their thermodynamic and kinetic properties under arbitrary thermodynamic conditions still necessitate computational models that are free of empirical factors. First-principles calculations enable more accurate atomistic simulations without relying on empirical interatomic potentials. The methods based on the density functional theory[75,76] are particularly useful in implementing reliable computer simulations in condensed matter physics. Literature DFT based first-principles studies on the hydrostatic compression of coesite showed a gradual softening in shear elastic moduli with increasing pressure, in contrast to the rising of its bulk modulus[77]. This observation implied that the high-pressure disordering in coesite may be coupled with its anomalous

lattice instability. Peral *et al.*[78] conducted an *ab initio* MD simulation on one of the silicate materials (zeolite) and suggested that PIA is the result of a first-order transition associated with very localized, weakly interacting structure (like silicon tetrahedra in silica) distortions that become unstable upon compression. Durandurdu conducted constant pressure first-principles MD and suggested hydrostaticity plays an important role in the crystalline phase transition. Under different degrees of hydrostatic conditions, silica could either transform to the anatase-type structure, stishovite or $CaCl_2$-type post-stishovite structures[79].

Needless to say, understanding the phase transition behavior of silica through first-principles simulation is of vital importance to the interpretation of its densification mechanism. As indicated in the previous section that the pair potentials available in literature may lack the capability of describing the transition from Si tetrahedra to octahedra, first-principles simulation approaches will be undertaken in this thesis.

REERENCES

1. Jayaraman, A. Diamond anvil cell and high-pressure physical investigations. *Rev. Mod. Phys.* **55**, 65-108 (1983).

2. Hemley, R. J. Erskine Williamson, extreme conditions, and the birth of mineral physics, *Phys. Today*, **59**, 50-56 (2006).

3. Mao, H-K & Hemley, R. J. The high pressure dimension in earth and planetary science. *Proc. Nat. Acad. Sci.* **104**, 9114-9115 (2007).

4. Minomura, S. & Drickamer, H. G. Pressure induced phase transitions in silicon, germanium and some III–V compounds. *J. Phys. Chem. Solids* 23, 451 (1962).

5. Hemley, R. J., C. T. Prewitt & K. J. Kingma, High-pressure behavior of silica, in *Reviews of Mineralogy* (eds. P. Heaney, Gibbs, G. V. & Prewitt, C. T.) 41-81 (Mineralogical Society of America, Washington, D.C., 1994).

6. Tsuchida, Y. & Yagi, T. New pressure-induced transformations of silica at room temperature. *Nature* **347,** 267-269 (1990).

7. Dubrovinsky, L. S., *et al*. Experimental and theoretical identification of a new high-pressure phase of silica. *Nature* **388**, 362-365 (1997).

8. Andrault, D., Fiquet, G. F, Guyot, F. & Hanfland, M. Pressure-induced Landau-type transition in stishovite. *Science* **282**, 720-724 (1998).

9. Goresy, A. E., Dubrovinsky, L., Sharp, T. G., Saxena, S. K. & Chen, M. A monoclinic post-stishovite polymorph of silica in the shergotty meteorite. *Science* **288**, 1632-1634 (2000).

10. Haines, J., Leger, J. M., Gorelli, F. & Hanfland, M. Crystalline post-quartz phase in silica at high pressure. *Phys. Rev. Lett.* **87**, 155503 (2001).

11. Tsuchiya, T. & Tsuchiya, J. Prediction of a hexagonal SiO_2 phase affecting stabilities of $MgSiO_3$ and $CaSiO_3$ at multimegabar pressures. *Proc. Natl. Acad. Sci.* **104**, 1252-1255 (2010).

12. Miyahara, M., *et al*. Discovery of seifertite in a shocked lunar meteorite. *Nat. Commun.* **4**, 1737 (2013).

13. Swamy, V., Saxena, S. K., Sundman, B. & Zhang, J. A therdynamic assessment of silica phase diagram. *J. Geophys. Res.-Sol. Ea.* **99**, 11787-11794 (1994).

14. Coes, L. A new dense crystalline silica. *Science* **118**, 131-132 (1953).

15. Stishov, S. M. & Popova, S. V. A new dense modification of silica. *Geochemistry* **10**, 923-926 (1961).

16. Yagi, T. High-pressure silica: Densification in two steps. *Nat. Mater.* **5**, 935-936 (2006).

17. Teter, D. M. & Hemley, R. J. High pressure polymorphism in silica. *Phys. Rev. Lett.* **80**, 2145-2148 (1998).

18. Hazen, R. M., Downs, R. T. & Finger, L. W. High-pressure framework silicates. *Science* **272**, 1769-1771 (1996).

19. Dmitriev, V. P., Toledano, P., Torgashev, V. I. & Salje E. K. H. Theory of reconstructive phase transitions between SiO_2 polymorphs. *Phys. Rev. B* **58**, 11911 (1998).

20. Stixrude, L. & Karki, B. Structure and freezing of $MgSiO_3$ liquid in earth's lower mantle. *Science* **310**, 297-299 (2005).

21. Johnson, W. L. Thermodynamic and kinetic aspects of the crystal to glass transformation in metallic materials. *Prog. Mat. Sci.*, **30** 81-134 (1986).

22. Mishima O., Calvert L. D. & Whalley E. 'Melting ice' at 77L amd 10 kbar: a new method of making amorphous solids. *Nature* **310**, 393-395 (1984).

23. Str ässle, T., *et. al*. Temperature dependence of the pressure-induced amorohization of ice Ih studied by high pressure neutron diffraction to 30 K. *Phys. Rev. B* 82, 094103 (2010).

24. Richet, P. & Gillet, P. Pressure-induced amorphization of minerals: a review. *Eur. J. Mineral*. **9**, 907-933 (1997).

25. Hemley, R. J., Jephcaot, A. P., Mao, H-K., Ming, L. C. & Manghnani, M. H. Pressure-induced amorphization of crystalline silica. *Nature* **334**, 52-54 (1988).

26. Richard, G. & Richet, P. Room temperature amorphization of fayalite and high-pressure properties of Fe_2SiO_4 liquid. *Geophys. Res. Lett.* **17**, 2093-2096 (1990).

27. Guyot, F. & Reynard, B. Pressure-induced structural modifications and amorphization in olivine compounds. *Chem. Geol.* **96**, 411-420 (1992).

28. Kingma, K. J., Meade, C., Hemley, R. J., Mao, H-K. & Veblen, D. R. Microstructural observations of alpha-quartz amorphization. *Science* **259**, 666-669 (1993).

29. Daniel, I., Gillet, P., Mcmillan, P. F., Wolf , G. F. & Verhelst M. High-pressure behaviors of anorthite: compression and amorphization. *J. Geophys. Res. B* **102**, 10313 (1997).

30. Ravindran, T. R., Arora, A. K. & Gopalakrishnan, R. Pressure-induced amorphization of bismuth orthosilicate. *J. Phys.: Condens. Matter* **14**, 6579-6589 (2002).

31. Rastogi, S., Newman, M. & Keller, A. Pressure-induced amorphization and disordering on cooling in a crystalline polymer. *Nature* **353**, 55-57 (1991).

32. Rastogi, S., Hohne, G. W. H. & Keller, A. Unusual pressure-induced phase behavior in crystalline poly(4-methylpentene-1): calorimetric and spectroscopic results and further implications. *Macromolecules* **32**, 8897-8909 (1999).

33. Chiba, A., *et al.*, Pressure-induced structural change of intermediate-range order in poly(4-methyl-1-pentene) melt. *Phys. Rev. E* **85,** 021807 (2012).

34. Kruger, M. B. & Jeanloz, R. Memory Glass: An Amorphous Material Formed from $AlPO_4$. *Science* **249**, 647-649 (1990).

35. Serghiou, G. C. & Hammack, W. S. Pressure-induced disordering in α-$SrZrF_6$: Implications for the role of the countercation in glassy $SrZrF_6$. *J. Chem. Phys.* **96**, 6911-6916 (1992).

36. Serghiou, G. C., Winters, R. R. & Hammack, W. S. *Phys. Rev. Lett.* **68**, 3311-3314 (1992).

37. Kawasaki, S. Takubo. H. & Yamanaka, T. In situ Obervation of the Pressure Induced Amorphization of GeO_2. *Proc. Japan Acad.* **68**, 151-154 (1992).

38. Murashov, V. V. Pressure-induced phase transition of quartz-type GaPO4, *Phys. Rev. B* **53**, 107-110 (1996).

39. Pasternak, M. P., *et al.*, Pressure-Induced Concurrent Transformation to an Amorphous and Crystalline Phase in Berlinite-Type FePO4. *Phys. Rev. Lett.* **79**, 4409-4412 (1997).

40. Lima, R. J. C., *et al.*, Phase transition in an occupationally disordered sulfate system. *Solid State Commun.* **126**, 339-342 (2003).

41. Kumar, R. S., *et al.*, Pressure induced structural phase transition in $AgSbTe_2$. *Phys. Rev. B* **72**, 060101 (2005).

42. Varga, T. *et al.*, Heats of Formation for Several Crystalline Polymorphs and Pressure-Induced Amorphous Forms of AMo_2O_8 (A = Zr, Hf) and ZrW_2O_8. *Chem. Mater.* **19,** 468-476 (2007).

43. Grocholski, B., Speziale, S. & Jeanloz, R. Equation of state, phase stability, and amorphization of SnI4 at high pressure and temperature. *Phys. Rev. B* **81,** 094101 (2010).

44. Levitas, V. L., Ma, Y., Selvi, E., Wu, J. & Patten, J. A. High-density amorphous phase of silicon carbide obtained under large plastic shear and high pressure. *Phys. Rev. B.* **85,** 054114 (2012).

45. Kingma, K. J., Hemley, R. J., Mao, H-K. & Veblen, D. R. New high-pressure transformation in alpha-quartz. *Phys. Rev. Lett.* **70**, 3927-3930 (1993).

46. Campañá, C., Müser, M. H., Tse, J, Herzbach, D. & Schöffel, P. Irreversibility of the pressure-induced phase transition of quartz and the relation between three hypothetical post-quartz phases. *Phys. Rev. B* **70**, 224101 (2004)

47. Campañá, C. & Müser, On finite-size effects in the simulation of high pressure, quartz-like structures. *High Pressure Res.* **24**, 517-523. (2004)

48. Binggeli, N. & Chelikowsky, J. R. Structural transformation of quartz at high pressures. *Nature* **353**, 344-346 (1991).

49. Binggeli, N. & Chelikowsky, J. R. Elastic instability in α-quartz under pressure. *Phys. Rev. Lett.* **69**, 2220-2223 (1991).

50. Chaplot, S. L. & Sikka, S. K. Comment on "Elastic instability in α-quartz under pressure", *Phys. Rev. Lett.* **71**, 2674 (1993).

51. Binggeli, N. & Chelikowsky, J. R. Reply on comment "Elastic instability in α-quartz under pressure" *Phys. Rev. Lett.* **71**, 2675 (1993).

52. Choudhury, N. & Chaplot, S. L. *Ab initio* studies of phonon softening and high-pressure phase transitions of α-quartz SiO_2. *Phys. Rev. B* **73**, 094304 (2006).

53. Tse, J. S. & Klug, D. D. Mechanical instability of α-quartz: A molecular dynamics study. *Phys. Rev. Lett*. **67**, 3559-3562 (1991).

54. Dean, D. W., Wentzcovich, R. M., Keskar, N., Chelikowsky, J. R. & Binggeli, N. Pressure-induced amorphization in crystalline silica: Soft phonon modes and shear instabilities in coesite. *Phys. Rev. B* **61**, 3303-3309 (2000).

55. Huang, L., Durandurdu., M & Keiffer. J. Transformation pathways of silica under high pressure. *Nat. Mater*. **5**, 977-981 (2006).

56. Wentzcovich, R. M., Silva, Chelikowsky, J. R. & Bingeli. N. A new phase and pressure induced amorphization in silica. *Phys. Rev. Lett*. **80**, 2149-2151 (1998).

57. Martoňák, R., Donadio D., Oganov A. R. and Parrinello M. Crystal structure transformations in SiO_2 from classical and *ab initio* metadynamics. *Nat. Mater.* **5**, 623-626 (2006)

58. Martoňák, R., Donadio, D., Oganov, A. R. & Parrinello, M. From four- to six-coordinated silica: Transformation pathways from metadynamics. *Phys. Rev. B* **76**, 014120 (2007).

59. Angel, R. J., Mosenfelder, J. L. & Shaw, C. S. J. Anomalous compression and equation of state of coesite. *Phys. Earth Planet. In*. **124**, 71-79 (2001).

60. Angel, R. J., Shaw, C. S. J., Gibbs, G. V. Compression mechanisms of coesite. *Phys. Chem. Minerals*. **30**, 167-176 (2003).

61. Cernok, A. *et. al.* Pressure-induced phase transition in coesite. *Am. Miner*. **90**, 755-763 (2014).

62. Jephcoat, A. P., Mao, H-K. & Bell, P. M., *Hydrothermal Experiment Techniques* Ch. 11, (Wiley- interscience, New York, 1987).

63. Max, K. & Kügler, J. Subjective Light Pattern Spectroscopy in the Electroencephalic Range. *Nature (London).* **184**, 1823-1824 (1959).

64. McMullan, D. A forgotten French scanning electron microscope and a forgotten text on electron optics. *Proc. Roy. Microsc. Soc.* **23**, 283-288 (1988).

65. Binnig, G., Quate, C. F. & Gerber, Ch. Atomic force microscope. *Phys. Rev. Lett.* **56** 930–933 (1986).

66. Badro, J., Barrat, J-L. & Gillet, P. Numerical simulation of α-quartz under nonhydrostatic compression: memory glass and five-coordinated crystalline phases. *Phys. Rev. Lett.* **76**, 772-775 (1996).

67. Badro, J., *et al*. Theoretical study of a five-coordinated silica polymorph. *Phys. Rev. B* **56**, 5797-5805 (1997).

68. Lasaga, A. C. & Gibbs. G. V. Applications of quantum mechanical potential surfaces to mineral physics calculations. *Phys. Chem Miner.* **14**, 107-117 (1987).

69. Lasaga, A. C. & Gibbs. G. V. Quantum mechanical potential surfaces and calculations on minerals and molecular clusters, I, STO-3G and 6–31 G results, *Phys. Chem Miner*. **16**, 29-41 (1988).

70. Tsuneyuki, S., Tsukada, M., Aoki, H. & Matsui, Y. First-Principles Interatomic Potential of Silica Applied to Molecular Dynamics. *Phys. Rev. Lett.* **61**, 869 (1988).

71. van Beest, B. W. H., Kramer,G. J. & van Santen, R. A. Force fields for silicas and aluminophosphates based on *ab initio* calculations. *Phys. Rev. Lett*. **64**, 1955-1958 (1990).

72. Murashov, V. V. & Svishchev, I. M. Quartz family of silica structures: a comparative study of quartz, moganite and orthorhombic silica, and their phase transformations. *Phys. Rev. B* **57**, 5639-5649 (1997).

73. Kimizuka, H., Kaburaki, H. & Kogure, Y. Molecular-dynamics study of the high-temperature elasticity of quartz above the α-β phase transition. *Phys. Rev. B* **67**, 024105 (2003).

74. Farrow, M. R. & Probert, M. I. J. Structural transformations in laser shock-loaded quartz. *J. Appl. Phys.* **135**. 044508 (2011).

75. Hohenberg, P. & Kohn, W. Inhomogeneous electron gas. *Phys. Rev*. **136**, B864-B871 (1964).

76. Parr, R. G. Density functional theory. *Ann. Rev. Phys. Chem.* **34**, 631-656 (1983).

77. Kimizuka, H., Ogata, S. & Li, J. Hydrostatic compression and high-pressure elastic constants of coesite silica. *J. Appl. Phys*. **103**, 053506 (2008).

78. Peral, I. & Iniguez, J. Amorphization Induced by Pressure: Results for Zeolites and General Implications. *Phys. Rev. Lett.* **97**, 225502 (2006).

79. Durandurdu, M. Formation of an anataselike phase in silica under anisotropic stress: An *ab initio* constant-pressure study. *Phys. Rev. B* **80** 024102 (2009).

II. THEORETICAL APPROACH

2.1 Density functional theory

The density functional theory (DFT) is a quantum mechanical modeling method in solving the electronic structure of ionic systems[1-4]. With this theory, the potential energy of the system can be determined by functionals, *i.e.* functions of another function, which in DFT is the spatially dependent electron density.

2.1.1. Total energy in density functional theories

DFT finds its firm theoretical justification in the Hohenberg-Kohn theorems[1], which are summarized as below:

a). The ground-state energy of a many-electron system is a unique functional of its electron density.

b). The energy functional is minimized at its correct ground-state electron density.

A typical expression for a ground-state interacting system of electrons with classical nuclei fixed at position $\{\mathbf{r_i}\}$ is written as:

$$\mathrm{E}[\{\phi_\mathrm{i}\}] = \mathrm{E}_k[\{\phi_\mathrm{i}\}] + \int V_{ext}\,(\mathbf{r_i})n(\mathbf{r_i})d\mathbf{r_i} + \frac{1}{2}\int V_H\,(\mathbf{r_i})n(\mathbf{r_i})d\mathbf{r_i} + \mathrm{E}_{xc}[n] \qquad (2.1)$$

The ground state of the system can be obtained by minimizing the value of $\mathrm{E}[\{\phi_\mathrm{i}\}]$, which is the so-called Kohn-Sham energy[2]. Equation (2.1) is an explicit functional of the

set of auxiliary functions $\{\phi_i\}$, the Kohn-Sham orbitals that satisfy the orthonormality relation $\langle\phi_i|\phi_j\rangle = \delta_{ij}$. The ground associated electronic one-body density or ground-state charge density $n(\mathbf{r_i})$ is built from occupied orbitals,

$$n(\mathbf{r_i}) = \sum_{i}^{occ} f_i |\phi_i(\mathbf{r_i})|^2 \tag{2.2}$$

where $\{f_i\}$ are integer occupation numbers. In the Eq. (2.2), the obtained charge density is a completely antisymmetrised product of one-electron wave functions $\phi_i(\mathbf{r_i})$, the Slater determinant, commonly named as the "Kohn-Sham determinant", that satisfying the Schrödinger equation:

$$H^{KS}\phi_i(\mathbf{r}) = \epsilon_i \phi_i(\mathbf{r}) \tag{2.3}$$

The eigenvalue ϵ_i refers to the lowest energy of the system at ground state. The Kohn-Sham Hamiltonian H^{KS}, deriving from the equation 2.1, consisting of the kinetic energy term, the local potential term and the exchange correlation term that describes the *many-body* effects, will be discussed in detail in the next paragraph.

The first term in the energy functional Eq. (2.1) is the kinetic energy of a non-interacting reference system:

$$E_k[\{\phi_i\}] = \sum_{i}^{occ} f_i \left\langle \phi_i \left| -\frac{1}{2}\nabla^2 \right| \phi_i \right\rangle \tag{2.4}$$

including the same number of electrons exposed to the same external potential as in the fully interacting system. The second term, the external potential, comprises the Coulomb interactions between electron-nuclei interactions and inter-nuclei interactions.

$$V_{ext}(\mathbf{r_i}) = -\sum_i \frac{\mathrm{Z}_i}{|\mathbf{R}_i - \boldsymbol{r}|} + \sum_{i<j} \frac{\mathrm{Z}_i \mathrm{Z}_j}{|\mathbf{R}_i - \mathbf{R}_j|} \tag{2.5}$$

The third term is the Hartree energy, indicating the classical electrostatic energy of two charge clouds which stem from the electronic density. It is obtained by integrating electrostatic energy spatially:

$$V_H(\mathbf{r_i}) = \int \frac{\mathrm{n}(\boldsymbol{r}')}{|\boldsymbol{r}_i - \boldsymbol{r}'|}\, d\boldsymbol{r}' \tag{2.6}$$

2.1.2. The exchange-correlation energy and its approximation

The last contribution in the Kohn-Sham energy is the exchange-correlation energy $\mathrm{E}_{xc}[n]$, which is defined as the remainder between the exact energy and its Kohn-Sham decomposition in terms of the previous contributions. The approximation of this term is crucial to the implementation of the density functional theory and many works have been done to improve its accuracy and applicability for different systems. A discussion focusing on the utilization of the exchange-correlation functional in the framework of first-principles simulation is for example given in ref. 5. In the simplest case this term can be approximated into an interacting but homogeneous electron gas at the density given by the local density $n(\mathbf{r})$ at space-point **r**. This simple but surprisingly successful approximation is the famous "local density approximation (LDA)" that has been applied to a wide range of ionic systems[6].

$$E_{xc}^{LDA}[n] = \int n(\mathbf{r})\ \epsilon_{i\,xc}^{LDA}\big(n(\mathbf{r})\big) d\boldsymbol{r} \tag{2.7}$$

Despite its remarkable success, LDA tends to perform inaccurately for strongly correlated systems, for example it incorrectly predicts the Mott insulator nature of

transition metal oxides XO (X=Fe, Mn, Ni)[7]. A significant improvement of the accuracy has been achieved by introducing the so call "generalized gradient approximation" (GGA), where this exchange-correlation energy is approximated by an integral over a function that depends on the charge density as well as its spatial gradient[8]:

$$E_{xc}^{GGA}[n] = \int n(\mathbf{r})\ \epsilon_{i_{xc}}^{GGA}\big(n(\mathbf{r}), \nabla n(\mathbf{r})\big) d\boldsymbol{r} \tag{2.8}$$

It extends the applicability of density functional calculations to the realm of complex quantum physics and chemistry and has been extensively tested on molecules, crystals, surfaces and many other ionic systems[9-15]. For consistency purposes, only the GGA functionals were used throughout this thesis.

2.1.3. Born-Oppenheimer approximation and self-consistent field method

The approach to solve the static electronic structure is based on the Born-Oppenheimer approximation[16], where the electronic motion is considered much faster than the nuclear motion. We assume the nuclei are frozen among the motion of electrons. By constructing the Hamiltonian for the many-particle system, the Schrödinger equation can be solved in a self-consistent manner, named as the self-consistent field theory (SCF)[17-19]. The computational flowchart of SCF is showed in Fig. 2.1, as the calculation is initialized by guessing a set of properly antisymmetrised wavefunctions (the slater determinant). The numerical solutions of the Schrödinger's equation can be found by diagonalizing the Hamiltonian and solving a matrix problem. The charge density will be updated according to the newly computed eigenvalues. The potential energy, interatomic forces and the charge density of the current step are compared with the prior step. If the

difference falls below the preset threshold, the system is considered as converging into a self-consistent ground state. If not, the charge density ρ is mixed with the previous step's in some mixing algorithm (*e.g.* linear mixing as in equation 2.9).

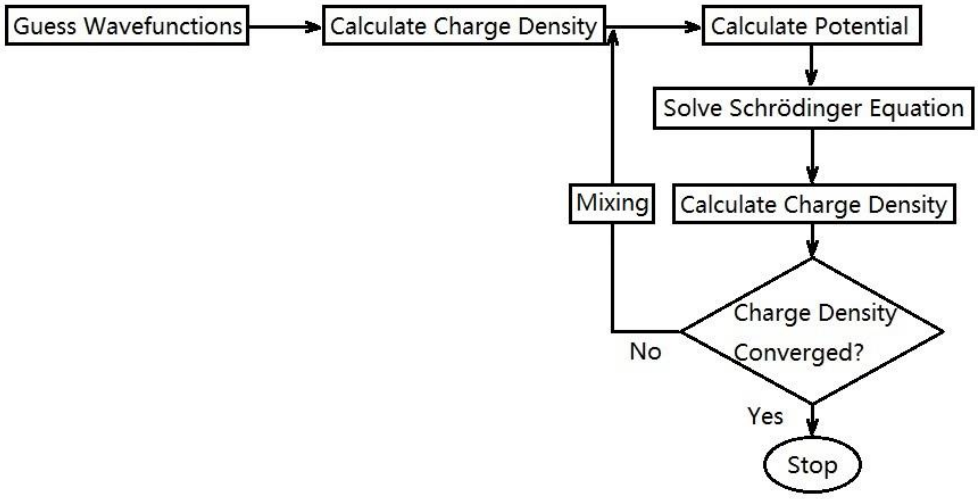

Figure 2.1. Simplified flow chart of self-consistent field theory calculation.

$$\rho_{in}^{n+1} = \alpha\rho_{out}^{n} + (1-\alpha)\rho_{in}^{n} \tag{2.9}$$

where the ρ_{in} and ρ_{out} are the input and output charge density, and α is the proportion in the linear mixing. The mixed charge density is sent into the loop and starts a new iteration. Such iteration continues until the converge criterion is satisfied. For each system, the self-consistent solution gives a converged charge density distribution under a controlled accuracy and the state obtained is considered as the ground state in the preset computational constrains.

2.2 Pseudopotentials methods

The Schrödinger equation (2.3) is solved by expanding the wavefunction:

$$\phi(\boldsymbol{r}) = \sum_i a_i \, \varphi_i(r) \tag{2.10}$$

The equation converts the Schrödinger equation to an eigenvalue problem. The form of ϕ_i distinguishes different electronic structure methods from each other. For example in the augmented plane wave (APW) method, ϕ_i has a spherical harmonics from inside a sphere surrounding the atomic sites and a plane wave from outside these spheres (called the muffin-tin spheres). Inside the muffin-tin radius the wave functions are expressed in terms of Bessel functions while expressed as Neumann functions outside[20-24]. These methods, termed as all-electrons methods, solve for all electrons in the system and therefore demand a considerable amount of computational power to calculate even a small ionic system (1 or 2 unit cells). Another class of methods freezes the core electrons, separating them from the valence electrons. These methods, known as the pseudopotential methods, replace electronic degrees of freedom in the Hamiltonian by an effective potential, leading to a reduction of number of electrons in the system and thereby allow for faster calculation or the treatment of larger systems.

2.2.1 Norm-conserving pseudopotentials

The pseudopotentials used for most *ab initio* simulation in this thesis are generated from all-electron atomic calculations. Most of those pseudopotentials are built on the basis of four general conditions:

1. The generated valence pseudo-wavefunction should be nodeless.
2. The normalization of pseudo wave function inside the core region is conserved so

that the wave function outside the core resembles that of the all-electron atom as closely as possible. This is known as the norm-conserving condition.

3. Within the core region, the charge density from the all-electron wave function should be equal to the one from normalized pseudo-wavefunction:

$$\int_0^{r_c} r^2 \left|\psi_l^{ps}(r)\right|^2 dr = \int_0^{r_c} r^2 |\psi_l^t(r)|^2 dr \qquad (2.11)$$

This constrain suffers problematic results if the wave function is expanded with a plan-wave basis outside the core-region, where the rugged pseudopotentials at the core boundaries can occur when the kinetic energy cut-off is not large enough. In some cases the typical kinetic energy cut off has to be set very large to ensure the smoothness of pseudopotentials.

4. The eigenvalues calculated from both all-electron wavefunction and normalized radial pseudo-wavefucntion should be equal.

We employed the combination of the Becke exchange functional and the Lee-Yang-Parr correlation functional (BLYP) to account for the exchange-correlation energy, parameterized by Goedecker *et al.*[25]. A typical kinetic cut-off is 150-200 *Ry* in the majority of our simulations, producing well-converged potential energy and its derivatives (*e.g.* inter-atomic force, cell stress tensor) for the silicate systems.

2.2.2 Projected augmented-wave pseudopotentials

For the norm-conserving pseudopotentials introduced in the previous section, the all-electron wave function gets replaced inside some core radius by a soft, nodeless, pseudo wave function. Since the pseudo and all-electron wave functions are identical outside the core radius, pseudo wave function must have the same norm as the all-

electron wave function within the chosen core radius. As shown previously, the core radius needs to be as large as the outermost maximum to well reproduce the charge distribution and moments of the all-electron wave function. Therefore in strongly localized systems (like hydrogen, oxygen, transition metal and rare earth elements), it requires a large kinetic plane wave cutoff (up to 200 Ry in some of my simulations). To compromise at the stake of sacrificing accuracy and reliability, Blöchl proposed a linear transformation to connect the pseudo and all-electron wave functions, named as the projector augmented-wave method (PAW)[26-27].

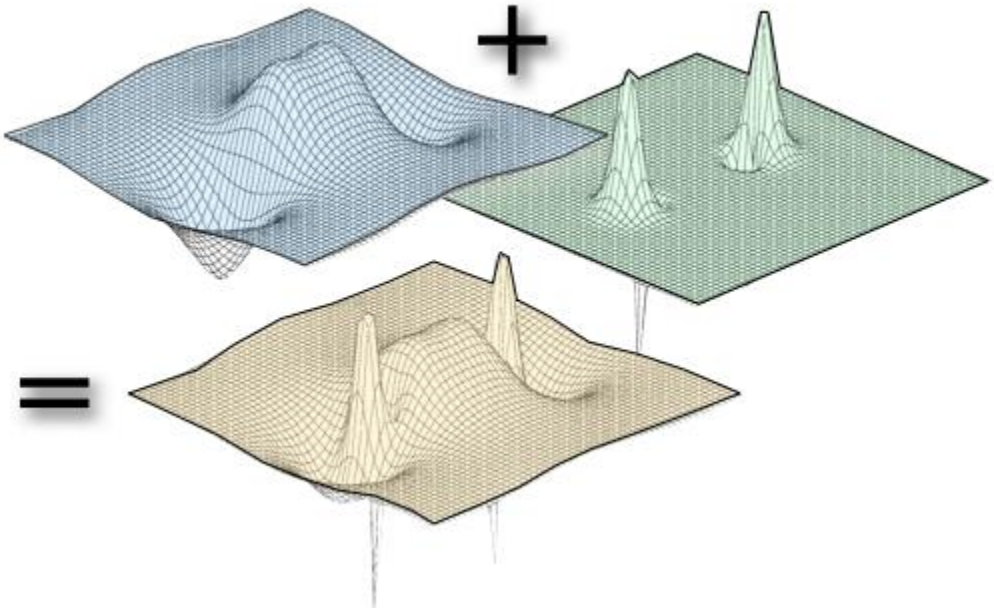

Figure 2.2. Schematic representation of the PAW transformation. The pseudized wavefunction is constructed by the oscillatory part close to atoms (two atoms in the figure, represented by two hills) and a smooth interstitial function.

The derivation of the PAW method is complicated[28]. In general, the PAW method is based on a formal division of the whole space into two distinct regions: a collection of non-overlapping spherical regions around each atom and the remainder (see Fig. 2.2). It introduces a set of localized projector functions to reproduce the all-electron wave functions. Since the projector functions are parameterized, it only requires a portion of wave function cutoff as in the all electron methods, thus significantly boosts computation speed. The PAW method is widely used in simulation packages like CASTEP, VASP, ABINIT, *etc.* Although the PAW method is not extensively used in this thesis, we still applied it to our work whenever necessary, mainly to validate our computational results achieved from using different types of pseudopotentials.

2.3 Ionic geometric relaxation

In determining the optimal configuration of an ionic system, geometric relaxation is a popular method to calculate the static structural properties at the minimum energy (also known as the 0 K configurations). Generally speaking, geometric optimization starts from a given point on the free energy landscape and attempts to find the configuration of minimum energy.

The geometric optimization problem is more of a mathematic optimization problem. We employed first-principles potentials and the quasi-Newton optimization method[29] to find the minimum energy in the degree of freedom of $3N$-6 (N is the number of atoms). The quasi-Newton method is a first order optimization method since the second order Hessian matrix does not need to be explicitly computed. It is a generalization of the secant method to find the root of the first derivative for multidimensional problems. A

simplified 1D problem is showed below:

$$E(\boldsymbol{x_k} + \Delta\boldsymbol{x}) = E(\boldsymbol{x_k}) + \nabla E(\boldsymbol{x_k})\Delta\boldsymbol{x} + \frac{1}{2}\Delta\boldsymbol{x^T} B \Delta\boldsymbol{x} \tag{2.12}$$

where $\nabla E(\boldsymbol{x_k})$ is the gradient of potential which is set to zero, and B is an approximation of Hessian matrix. The gradient of the approximation is:

$$\nabla E(\boldsymbol{x_k} + \Delta\boldsymbol{x}) = \nabla E(\boldsymbol{x_k}) + B\Delta\boldsymbol{x} \tag{2.13}$$

which is the secant function. The determination of B matrix is the core issue in quasi-Newton method and many algorithms are available. The Broyden-Fletcher-Goldfarb-Shanno algorithm[30] is used in this thesis by default, which usually yields reasonable results. The matrix B at the kth Newton step is shown below:

$$B_{k+1} = B_k + \frac{E_k E_k^T}{E_{k\Delta\boldsymbol{x}}^T} - \frac{B_k \Delta\boldsymbol{x} (B_k \Delta\boldsymbol{x})^{\boldsymbol{T}}}{\Delta\boldsymbol{x^T} B_k \Delta\boldsymbol{x}} \tag{2.14}$$

where B can be initialized as the identity matrix. The optimizer is applied every time a SCF solution is reached, known as one ionic step. The criterion of convergence is measured by the change of interatomic force and total energies. We set the force criterion as 1×10^{-2} eV/Å on each atom in most cases. However, the actual convergence criteria will be specified in each individual section under different computational environments.

2.4 Molecular dynamics

Unraveling the mechanism of phase transitions is the major goal in this thesis. The phase transition can be considered as a kinetic process, as the atomic positions and cell variables are dynamically changing under various pressure and temperature conditions. In this section we deal with those dynamical properties with molecular dynamics (MD) simulation.

2.4.1 Molecular dynamics in Verlet's scheme

The goal of this section is to derive molecular dynamics of classical particles from the fundamental Verlet's method[31], without the input of any potential models. Starting from the Hamiltonian of an arbitrary N-body system:

$$H = \sum_{i=1}^{N} \frac{1}{2} m_i v_i^2 + \sum_{i<j}^{N} \sum_{j}^{N} U(\boldsymbol{r_i}, \boldsymbol{R_I}) \tag{2.15}$$

where m_i is the mass of ith particle and v_i is its mechanical velocity. The $\boldsymbol{r}_\mathrm{i}$ and $\boldsymbol{R}_\mathrm{I}$ are electronic and nuclear degrees of freedom respectively. In the Verlet's method, the initial position and velocities conditions are known as:

$$\{\boldsymbol{r_1}(0), \boldsymbol{r}_2(0), \dots, \boldsymbol{r}_N(0)\}$$

$$\{\dot{\boldsymbol{r}}_1(0), \dot{\boldsymbol{r}}_2(0), \dots, \dot{\boldsymbol{r}}_N(0)\}$$

The movement at time step Δt is derived from the Taylor expansion of motions (cut off at the third term of the Taylor expansion):

$$\boldsymbol{r}_i(\Delta t) \equiv \boldsymbol{r}_i(0) + \dot{\boldsymbol{r}}_\iota(0)\Delta t + \frac{F_{\boldsymbol{ri}(0)}}{2m_i}\Delta t^2 \tag{2.16}$$

$$\dot{\boldsymbol{r}}_\iota(\Delta t) \equiv \dot{\boldsymbol{r}}_\iota(0) + \frac{F_{\boldsymbol{ri}(0)} + F_{\boldsymbol{ri}(\Delta t)}}{2m_i}\Delta t \tag{2.17}$$

Based on this trajectory in the phase space, the numerical average values $\langle A \rangle$ of the motion can be calculated:

$$\langle A \rangle_{n\Delta t} \cong \frac{1}{n\Delta t} \sum_{s=0}^{n} A[\boldsymbol{r}(s\Delta t), \dot{\boldsymbol{r}}(s\Delta t)]\Delta t \tag{2.30}$$

Those averaged values are useful in defining the equilibrium of the simulated systems. In statistical mechanics equivalence, we can define an idealization consisting of a large number of virtual copies for the N-body system, known as the thermodynamics

ensemble. For example, MD simulations run in an isolated system, the total energy *E*, volume *V* and the number of particles *N* are conversed. In such systems the values of *NVE* are constants, known as the microcanonical ensembles:

$$\langle A \rangle \equiv \bar{A}_{NVE} \tag{2.31}$$

We principally use two types of ensembles to achieve targeting temperature and pressure: the canonical ensemble (NVT) and the isothermal-isobaric ensemble (NPT). Introductions for both ensembles are given in the following sessions.

2.4.2 Canonical ensemble

A system with the canonical ensemble is in thermal equilibrium with a heat bath. While the constant temperature is achieved by exchanging heat with the heat bath, the simulation box is fixed so that the number of particles and volume are kept constant. In this thesis NVT ensembles were mainly used to equilibrate the structures to a stable state and examine their thermal stability.

There are many thermostats available for constant temperature molecular dynamics simulations. In this thesis, we employed the Nosé-Hoover thermostat to achieve the realistic constant temperature condition[32]. The Nosé-Hoover method has been commonly used as one of the most accurate and efficient methods for many simulation systems.

The spirit of the Nosé-Hoover algorithm is the extended Lagrangian that contains additional, artificial coordinates and velocities to describe particle fluctuations at a certain temperature. In a system of *N* particles, with coordinates $\boldsymbol{q}_i$, masses $\boldsymbol{m}_i$, momenta $\boldsymbol{p}_i$ and potential energy $\phi(\boldsymbol{q})$ and time *t*, Nosé[32] introduced an additional degree of freedom *s* acting as an external system on the simulated system. The external system has virtual

variables (coordinates $\boldsymbol{q}_i'$, momenta $\boldsymbol{p}_i'$ and time t') that relates to the real simulated system:

$$\boldsymbol{q_i} = \boldsymbol{q_i'}, \qquad \boldsymbol{p_i} = \frac{\boldsymbol{p_i'}}{s}, \qquad t = \int_0^{t'} \frac{dt'}{s} \tag{2.32}$$

The extended Lagrangian is constructed as:

$$L = \sum_{i=1}^{N} \frac{m_i}{2} s^2 \, \dot{\boldsymbol{q}}_i'^2 - \phi(\boldsymbol{q}') + \frac{Q}{2}\dot{s}^2 - gkT\ln s \tag{2.33}$$

where Q is an effective mass associated to s and g=3N+1 is the degree of freedom of the system. The value of Q, also known as the thermal inertia parameter, determines the rate of the heat transfer. The chosen of Q has to be appropriate to ensure the efficiency and validity of the simulated canonical ensemble. Equation 2.33 relates the coordinate and momenta of the virtual system. Thus the Hamiltonian of the extended system can be represented by:

$$H = \sum_{i=1}^{N} \frac{\boldsymbol{p}_i'^{\boldsymbol{2}}}{2m_i s^2} + \phi(\boldsymbol{q}') + \frac{p_s^2}{2Q}\dot{s}^2 - gkT\ln s \tag{2.34}$$

where $p_s = \frac{\partial L}{\partial \dot{s}} = Q\dot{s}$ is the partial derivative of Lagrangian with s. Based on the Hamiltonian and the relationship between virtual variables and real variables, the real space equation of motion are[33]:

$$\frac{d\boldsymbol{q_i}}{dt} = \frac{\boldsymbol{p_i}}{m_i} \tag{2.35}$$

$$\frac{d\boldsymbol{p_i}}{dt'} = -\frac{\partial \phi}{\partial \boldsymbol{q_i}} - s^2 \frac{p_s}{Q} \boldsymbol{p_i} \tag{2.36}$$

$$\frac{\partial \ln(s)}{\partial t} s^2 \frac{p_s}{Q} \tag{2.37}$$

$$s \frac{d^2 \boldsymbol{s}}{dt^2} = \frac{1}{Q} \left(\sum_{i=1}^{N} \frac{\boldsymbol{p_i^2}}{2 m_i s^2} - gkT \right) \tag{2.38}$$

These equations describe the Nosé-Hoover thermostat. Values like coordinate and momenta can be calculated by propagating equations of motion over time. By choosing the right value of *Q*, we can impose time average value of temperature to be equal to the prescribed value.

2.4.3 Isothermal-isobaric ensemble: the Parrinello-Rahman method

The implementation of an isothermal-isobaric ensemble is more complicated. We allow the full flexibility of the simulation cell to generate a constant pressure condition, as described in the paper by Glenn[34]. This method, hinged on the Parrinello-Rahman method[35-36], is a robust hybrid method that removed some inconsistencies in the prior schemes[37-38]. The partition function, yielding the probability distribution in space, is determined by the following equation under hydrostatic pressures:

$$Z = \int d\boldsymbol{h} \exp[-\beta P_{ext} \det(\boldsymbol{h})] Q(\boldsymbol{h}) \det[\boldsymbol{h}]^{1-d} \tag{2.39}$$

where $\boldsymbol{h}$ is the normal matrix of cell parameters, P_{ext} is the external pressure, and $Q(\boldsymbol{h})$ is a canonical partition function. This is a fully nonlinear treatment of the case that isotropic tension is applied along the instantaneous lattice vectors. The incorporation of the

variation of lattice matrix enables the changes of cell variables upon the applied external pressure. The equilibrium of the system is achieved by comparing the averaged internal pressure calculated from the above equation and the set external pressure. The shape of the cell is adjusted accordingly.

More details of the Parrinello-Rahman method can be found in the original methodology papers[34-36]. Successful implementations of this method in MD studies of silica are discussed in a review article by Rajappa[39].

2.4.4 Car-Parrinello type molecular dynamics

Incorporating the spirit of molecular dynamics and the DFT representation of energy, we are able to simulate the motion of condense matter in the scheme of first-principles calculation. As we have discussed in section 2.1, first-principles MD under the Born-Oppenheimer approximation[16] resolves the static electronic structure problem in each MD step. A self-consistent potential energy has to be reached at each MD step; hence the number of self-consistent cycles equals to the number of MD steps. The Car-Parrinello (CP) type MD was proposed by R. Car and M. Parrinello in 1985, in an effort to permit the application of density-functional theory to much larger systems than previously feasible[40]. In CPMD, the following objectives are achieved: (i) integrating the equations of motion on the time scale set by the nuclear motion. (ii) intrinsically take advantage of the smooth time evolution of the dynamically evolving electronic subsystem as much as possible. The second thrust allows us to avoid explicit SCF calculation on each MD step.

Algorithmically, the CP type MD transforms the separation of fast electronic and

slow nuclear motion into a classical-mechanical adiabatic energy-scale separation in the framework of dynamical system theory. The energy of the electronic subsystem $\langle\Psi_0|H|\Psi_0\rangle$ is a function of the nuclear positions $\{\mathbf{R}_\mathrm{I}\}$. But at the same time it can be considered to be a functional of the wave function and thus of a set of orbitals $\{\phi_\mathrm{i}\}$. Its force on the nuclei is obtained from the derivative of a suitable Lagrangian with respect to the nuclear positions. In addition, possible constrains within the set of orbitals have to be imposed, such as the orbital orthonormality. These constrains might not only be a functional of set of orbitals $\{\phi_\mathrm{i}\}$, but also a function of the nuclear positions $\{\mathbf{R}_\mathrm{I}\}$. Both these dependences have to be taken into account properly in deriving the CP type equations of motion, since it is crucial to generate a proper energy-conserving dynamical evolution. In light of this, Car and Parrinello introduced the following class of Lagrangians[41].

$$\mathcal{L} = \sum_I \frac{1}{2} M_I \dot{\boldsymbol{R}}_I^2 + \sum_i \mu\langle\dot{\phi}_\iota|\dot{\phi}_\iota\rangle - \langle\Psi_0|H|\Psi_0\rangle + constraints \tag{2.45}$$

where M_I is the mass of nuclear and μ is the fictitious mass of the electron. The equations of motion for both nuclear positions and orbitals are obtained from the associated Euler-Lagrange equations:

$$\frac{d}{dt}\frac{\partial\mathcal{L}}{\partial\dot{\boldsymbol{R}}_I} = \frac{\partial\mathcal{L}}{\partial\boldsymbol{R}_I} \tag{2.46}$$

$$\frac{d}{dt}\frac{\partial\mathcal{L}}{\partial\dot{\phi}_\iota} = \frac{\partial\mathcal{L}}{\partial\phi_i} \tag{2.47}$$

Now plug in the functional derivatives respect to orbitals. The generic Car-Parrinello equations of motion are calculated to be of the form:

$$M_I \ddot{\boldsymbol{R}}_{\boldsymbol{I}}(t) = -\frac{\partial}{\partial \boldsymbol{R}_I}\langle \Psi_0 | H | \Psi_0 \rangle + \frac{\partial}{\partial \boldsymbol{R}_I}\{constraints\} \tag{2.48}$$

$$\mu \ddot{\boldsymbol{\phi}}_{\iota}(t) = -\frac{\delta}{\delta \boldsymbol{\phi}_i}\langle \Psi_0 | H | \Psi_0 \rangle + \frac{\delta}{\delta \boldsymbol{\phi}_i}\{constraints\} \tag{2.49}$$

The above equations can be further simplified by using the Kohn-Sham theory in conjunction with position-independent constrains as discussed earlier in chapter 2.1. The constraints are explicitly represented by:

$$\{constraints\} = \sum_{i,j} \Lambda_{ij} \left(\langle \phi_i | \phi_j \rangle - \delta_{ij} \right) \tag{2.50}$$

where the proper orbital orthonormality $\langle \phi_i | \phi_j \rangle = \delta_{ij}$, must be imposed by Lagrange multipliers Λ_{ij}. Hence it generates the well-established Car-Parrinello equations of motion:

$$M_I \ddot{\boldsymbol{R}}_{\boldsymbol{I}}(t) = -\nabla_I \langle \Psi_0 | H^{KS} | \Psi_0 \rangle \tag{2.51}$$

$$\mu \ddot{\boldsymbol{\phi}}_{\iota}(t) = -H^{KS}\phi_i + \sum_j \Lambda_{ij}\, \phi_j \tag{2.52}$$

The nuclei evolve in time at a certain physical temperature $\propto \Sigma_I M_I \dot{\mathrm{R}}_I^2$, while the electron fictitious temperature $\propto \Sigma_i \mu \langle \dot{\phi}_{\iota} | \dot{\phi}_j \rangle$ can be associated accordingly with the electronic degrees of freedom. The fictitious temperature is lower when the electronic subsystem is close to its instantaneous minimum energy, where it is close to the Born-Oppenheimer surface. Thus the wave functions optimized for the initial configuration of the nuclei will stay close to its ground state also during time evolution of it is kept at a sufficiently low fictitious temperature.

The CP type MD is targeting on separating the nuclear and electronic motions such that the fast electronic subsystem stays cold also for long times but still follows the slow nuclear motion adiabatically. How and to what extent to achieve this target requires

complex technical investigation, such as decoupling of nuclear and electron subsystems as well as adiabatic time evolution. Therefore the lengthy details on implementing CPMD simulations will not be discussed in this thesis. However, the practice was analyzed in details in the pioneering paper based on well-controlled model systems[42]. The adiabaticity issue was also addressed in mathematics by Bornemann and Schütte[43] and in terms of a generalization to a second level of adiabatic decoupling[44].

2.5 Barrier crossing algorithms

While *ab initio* MD empowers us to investigate the transition pathway, very often the large kinetic energy barrier separating different phases makes conventional MD simulations highly inefficient. We introduce two methods in this session: metadynamics and nudge elastic band method (NEB) to deal with barrier-involved problems. Metadynamics is specialized in escaping energy barriers by artificially filling the free energy landscape. It is a powerful method to search for metastable structures. On the other hand, the NEB method can accurately calculate the transition pathway connecting two phases close in the phase space.

2.5.1 Metadynamics

The Metadynamics algorithm was first introduced by A. Laio and M. Parrinello in 2002[45,46]. It provides a new computational method to sample rare events. The metadynamics algorithm describes the system as a function of collective variables (CVs) $\boldsymbol{S_\alpha}$. The collective variable can be one or combinations of order parameters that characterize the system in a timescale of *t*. Its potential V_{mtd} is described as:

$$V_{mtd} = V_{mtd}(\boldsymbol{S_\alpha}, t) \tag{2.53}$$

The choice of collective variables largely depends on the nature of the system. In general, the changes of CVs reflect the evolution of the structure during phase transformation. However the number of CVs needs to be as small as possible, to minimize the efforts to synchronize the energy depositing progress, where many unexpected issues can occur (*e.g.* the hill surfing problems[47]). In this thesis we initially performed test-runs on many order parameters and extract the most efficient CVs. The initialization has to be done before the actual execution of any metadynamics simulation and ensured the efficiency of the further simulation. During a molecular dynamics run with the metadynamics algorithm, the free energy is reconstructed at each time interval by adding a history-dependent potential, which is usually the sum of repulsive Gaussian potentials hills centered along the trajectory of CVs. Therefore the reconstructed Hamiltonian is the sum of first-principles energy and the free energy from metadynamics.

$$H(\boldsymbol{r}, \rho(\boldsymbol{r}), \boldsymbol{S_\alpha}, \boldsymbol{t}) = H_E(\boldsymbol{r}, \rho(\boldsymbol{r})) + V_{mtd}(\boldsymbol{S_\alpha}, t) \tag{2.54}$$

$$V_{mtd}(\boldsymbol{S_\alpha}, t) = \sum_{t_i<t} h(t_i) \exp\left[-\frac{(\boldsymbol{S_\alpha^i} - \boldsymbol{S_\alpha})^2}{2\delta_s{}^2}\right] \tag{2.55}$$

In order to determine the shape of the Gaussian functions (height $h(t_i)$ and width δ_s), it is helpful to run CPMD without depositing any bias energy for each CV combination to give an indication of the width of the well. The potential hills are added to the history-dependent potential $V_{\mathrm{mtd}}(\boldsymbol{S}_\alpha,t)$ with a meta-time step that is one or two orders larger than the MD time step. The potential encourages the system to build up in the reactant state, until it escapes via the local minima transition state to the next minima. Processing with a small hills results in better resolution so that the multidimensional free energy landscape

is obtained to arbitrary accuracy as the negative sum of $V_{mtd}(\boldsymbol{S}_\alpha,t)$ (see Fig. 2.3).

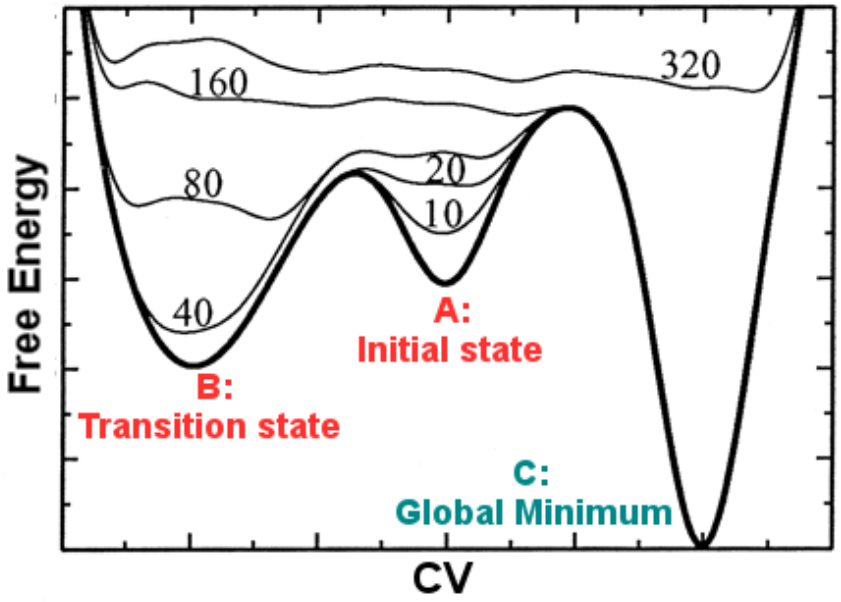

Figure 2.3. Schematic representation of the free energy surface for a one-dimensional problem. The simulation starts at local minima A and transits through the intermediate state B before reaching the global minimum. Numbers indicates the number of Gaussian hills deposited onto the free energy surface during the simulation progress.

Since the appearance of the energy surface depends on the complex properties of transition states, the exact details in implementing metadynamics follows a case-by-case manner, where their details can be found in each individual section.

2.5.2 Nudged elastic band method

The transition pathway directly connecting two stable phases is studied with the widely used nudged-elastic band method[48]. When the initial and final states of a reaction

are known, the NEB relaxes an initial path to a minimum-energy path (MEP). The structures on the transition pathway are called "replicas", where multiple replicas can be initialized as the geometric intermediates. The energy and force of the system were calculated at each ionic step until it satisfied the preset convergence criterion. Here we used the so-called solid-state NEB (ssNEB)[49], which is specialized in dealing with phase transitions involving cell shape changes. In this method, a *Jacobian* is used to combine atomic and cell degrees of freedom so that the MEP is insensitive to the choice of unit cell size and geometry:

$$J = \Omega^{1/3} N^{1/6} \tag{2.56}$$

where Ω is the volume of the unit cell and N is the number of atoms in the cell. It connects the strain from the cell into the same unit of atomic position, so that the changes in the configurations $\mathbf{\Delta R_{ss}}$ is formed by concatenating the strain ε and changes in atomic coordinates $\Delta\mathbf{R}$:

$$\Delta\mathbf{R}_{ss} = \{J\epsilon, \Delta\mathbf{R}\} \tag{2.57}$$

The ssNEB was implemented in VASP[50], together with the Transition States Tools VASP (VTST)[49]. Full geometry optimizations were made on both the α-quartz and quartz III structures. The projected augmented-waves (PAW) pseudopotentials with the Perdew-Wang GGA parameterization[51] for Si and O with a 550 eV plane basis cutoff were used in these calculations. Since α-quartz is metastable at high pressures, we employed a Hessian-based geometric optimization method such that it is possible to optimize the structure onto local maxima (first order saddle point) without transforming into the quartz III phase. Then the initial phase (α-quartz) and the final phase (quartz III) are sampled

with 16 replicas with equal image distances connecting the two reactant phases. We adopted a forced-based quick-min optimizer[52] to find the MEP in the phase transition pathway and the forces typically converged within 200 ionic steps.

2.6 Lattice dynamics: phonon calculations

The purpose for phonon calculations in this work is three-fold. (i) To examine the mechanical stability of the derived metastable phases. Both the necessary and sufficient condition for the mechanical stability of a crystal is the phonon stability[53,54], *i.e.*, $\boldsymbol{\omega}(\mathbf{q}, \boldsymbol{s})^{\mathbf{2}} > \mathbf{0}$ holds for any wave vector $\mathbf{q}$ and vibration mode *s***.** A phonon mode that has imaginary frequency, *i.e.*, $\boldsymbol{\omega}(\mathbf{q}, \mathbf{s})^{\mathbf{2}} < \mathbf{0}$, will lower the energy of the system, and indicate the crystal is mechanically unstable. (ii) The phonon vibration modes are used to estimate the Gibbs free energy of the crystals based on the quasi-harmonic approximation. (iii) To monitor the phonon-softening behavior of the Brillouin zone boundary of α-quartz and to see at what pressure the phonon instability (an indicator of mechanical instability) kicks in.

The first-principles phonon calculation was based on the same BLYP type GGA pseudopotential[25] with the Quantum Espresso phonon code. After completely relaxing the atomic structure, we computed the dynamical matrix on a grid of wave vectors in the Brillouin zone by the Density Functional Perturbation Theory (DFPT). The long range dipole-dipole interaction is taken into account using the dielectric tensor. It is possible to calculate the phonon frequencies at any wave vector $\mathbf{q}$ by reconstructing the dynamical matrix, known as the Fourier interpolation method.

The grid size and accuracy control is much dependent on the simulation size and systems. The technical details of phonon calculations will be discussed separately for each system.

2.7 Experimental approaches

The experiments we have conducted in this thesis are targeted on identifying the atomic structure of silica samples at high pressures. Accurately identifying the atomic structure of a compressed sample is an outstanding problem ever since the establishment of high pressure science. In this session, we introduce two major technical advancements employed in our high pressure research: i) the use of Diamond Anvil Cell (DAC) as a pressurization instrument. ii) the application of energy dispersive X-ray diffraction technique as a structure characterization tool.

2.7.1 Single crystal samples

Before discussing the experimental techniques, we introduce the use of single crystal samples that differentiate ours from other experiments. Powders and single crystal are two major sample categories in high pressure research. While powder samples can be recognized as the assembling of extremely tiny single crystals with arbitrary crystal orientations, single crystal samples have a well-defined crystalline orientation (Fig. 2.4 shows a comparison under electronic microscope).

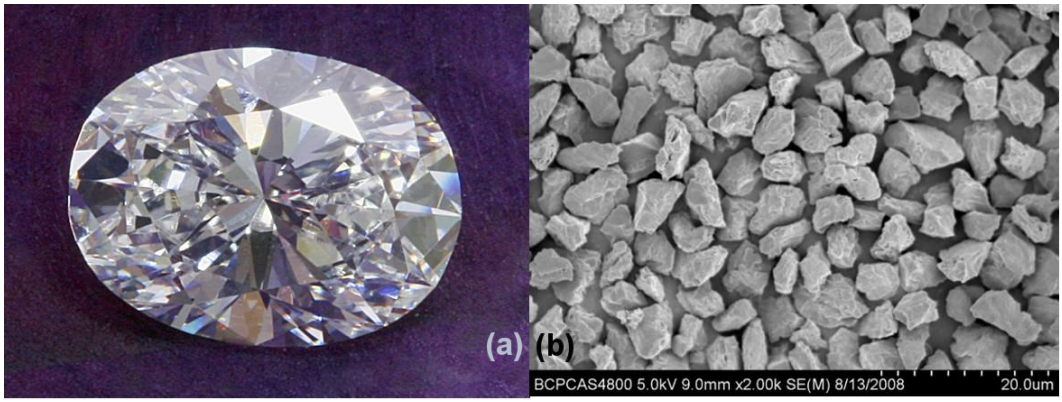

Figure 2.4. Diamonds in the form of (a) single crystal and (b) powder under scanning electronic microscopy (SEM). The SEM photo of polycrystalline diamonds, showing arbitrary crystalline orientations, are grained in size of around 20×20 μm, manufactured by Beijing Grish Hitech Co., Ltd.[55]

The advantages of using single crystal samples are: i) Single crystals are much more sensitive to minor structural changes (*e.g.* lattice distortion and metastable transition) than powders. ii) Eliminating the size and orientation effects encountered in polycrystalline samples and iii) Enable direct comparisons between experiment and *ab initio* simulation.

Therefore the single-crystal experiment is ideal to observe the metastable structures and the transition sequence, which serves as the primary sample type in this thesis.

2.7.2 Diamond anvil cell

Pressure, in its physical definition, can be increased by two methods: raising the force *F* applying perpendicular to the surface of an object, or shrinking the contact area *S*.

$$p = \frac{F}{S} \tag{2.58}$$

Efforts on achieving extreme pressure never stop. The state-of-the-art static pressurization experiments reported a 440 GPa pressure in a specially designed diamond anvil cell[56,57], where no other material than the diamond could survive under such circumstance without being crushed or losing crystalline shapes. Diamond, the ambient metastable allotrope of carbon, is known as the toughest mineral on earth and also most transparent to X-rays. Because of its extraordinary thermodynamical and optical properties, diamond is the ideal solid pressure medium for high pressure science.

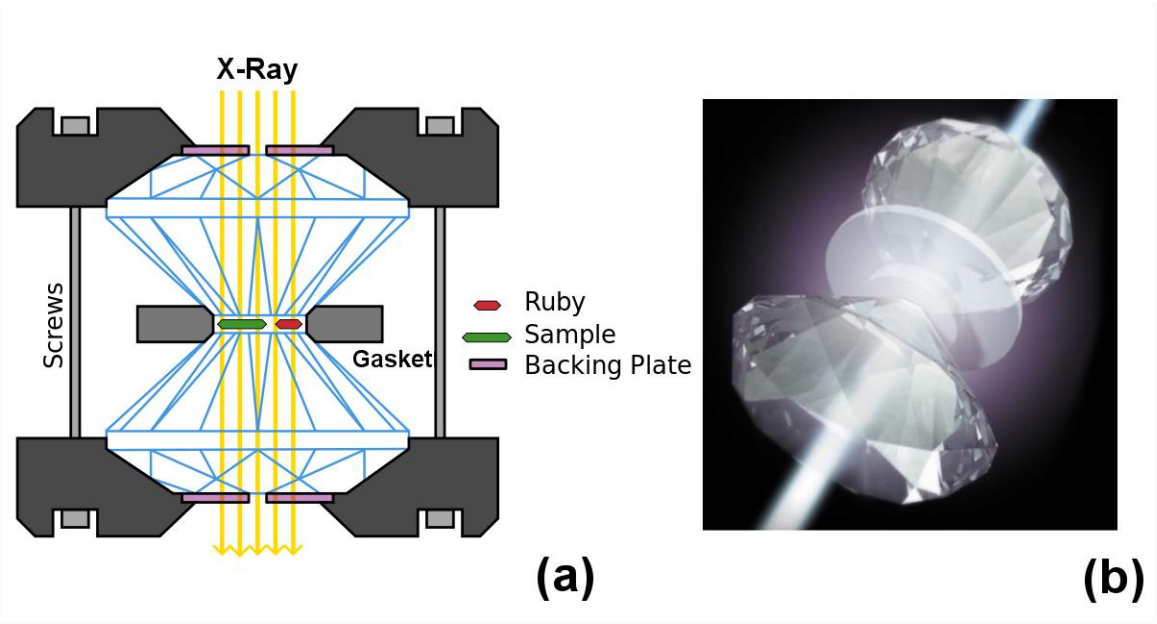

Figure 2.5. The diamond anvil cell. (a) Schematics cross section of the core of a diamond anvil cell. A sample and a piece of ruby (the pressure indicator) were sealed together by a gasket. Tightening of the screws moves the casings and the diamond closer together and builds pressure. The backing plate holds the diamond in place. (b) Visualization of electromagnetic radiation penetrating through DAC's axial direction, allowing scientific measurements.

The design of DAC, shown in Fig. 2.5, has been well established in this area and it is also the pressurizing instrument used in my thesis. The core component of DAC is a pair of well-aligned diamond anvils, where the contact area is minimized to amplify the compression effect at the same stress. The opening on the backing plates allows radiation rays scattered on a small piece of sample (Fig. 2.5b).

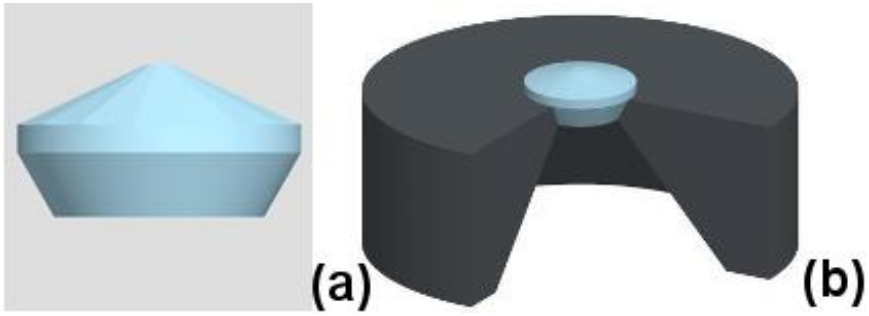

Figure 2.6. Designs of diamond anvil seats: (a) Representation of diamond anvil on the emergent beam side. It has shorter height than standard designed diamond anvils. (b) Diamond anvil put onto the cBN seat. X-rays are able to pass through the seat with lowered intensity, allowing open angles even wider than the seat hole size.

Specifically, DAC in the Mao-Bell design[58] was used as the major apparatus for compressing single crystal samples. The diamond anvil (300 μm in culet diameter, manufactured by Almax-easyLab, Co. Belgium[59]) is eight-sided and in oblate shape (Fig. 2.6), particularly designed for wide open-angle synchrotron experiments. The seat on the incident beam facet is made of the tungsten carbide, which has great hardness but absorbs most X-rays. On the emergent beam side, the seat is made of cubic boron nitride (cBN)

that is semi-transparent to X-rays. Whereas cBN is not as hard as tungsten carbide, we are granted wider diffraction angles even beyond the seat hole size on the emergent side by using this seat. It ensures a solid platform for applying pressure up to 60~70 GPa (the maximum pressure is also determined by the culet size, crystallization quality and many other factors). Diffracted beam permeating though the cBN seat can still reach the image plate in half intensity. The comprehensive experimental setup for different samples studied in this thesis will be demonstrated in separate sections, as their specifications vary.

2.7.3 Energy dispersive X-ray diffraction from synchrotron radiation source

Back to the 1940s, synchrotron radiation was named after its discovery in a general electric synchrotron accelerator built in 1946 and announced in May 1947 by Frank Elder and his research group[60,61]. They observed electromagnetic radiation emitted when charged particles were accelerated radially ($\mathbf{a} \perp \mathbf{v}$). By using bending magnets, undulators and/or wigglers, accelerated electrons (close to lightspeed) perform a snakelike motion in a giant storage ring circuit (Fig. 2.7). The synchrotron radiation beams are generated by the acceleration of ultrarelativistic charged particles through magnetic fields. Generally speaking, the radiation produced in this way is extremely strong in intensity (*e.g.* 1×10^{6}~1×10^{8} times greater than a regular X-ray diffractometer) and the frequencies generated can range over the entire electromagnetic spectrums. Those characteristics are ideal for high pressure research since the sample in DAC is very tiny. While a traditional diffractometer can take months to render a good quality DAC diffraction pattern, X-rays emitted in synchrotron radiation circuit are capable doing the same amount of job in seconds.

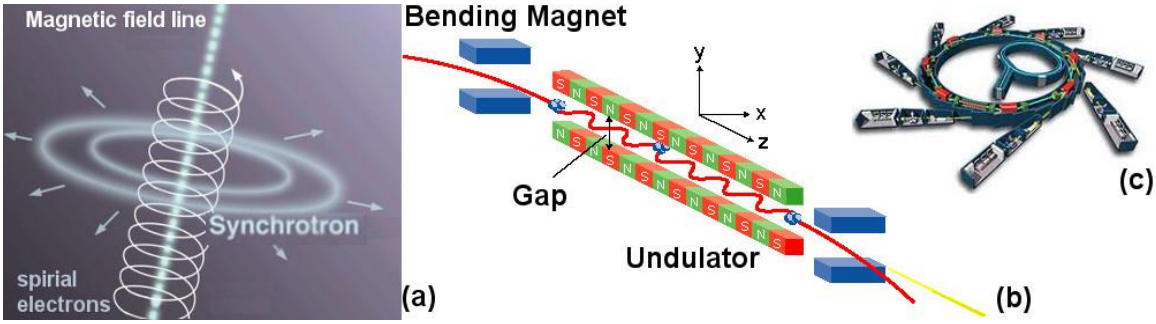

Figure 2.7. Generation of synchrotron beam from (a) bending magnets and (b) undulator. The inset figure (c) is a schematic build-up to the giant electrons storage ring. Line stations are constructed along the running direction of accelerated electrons.

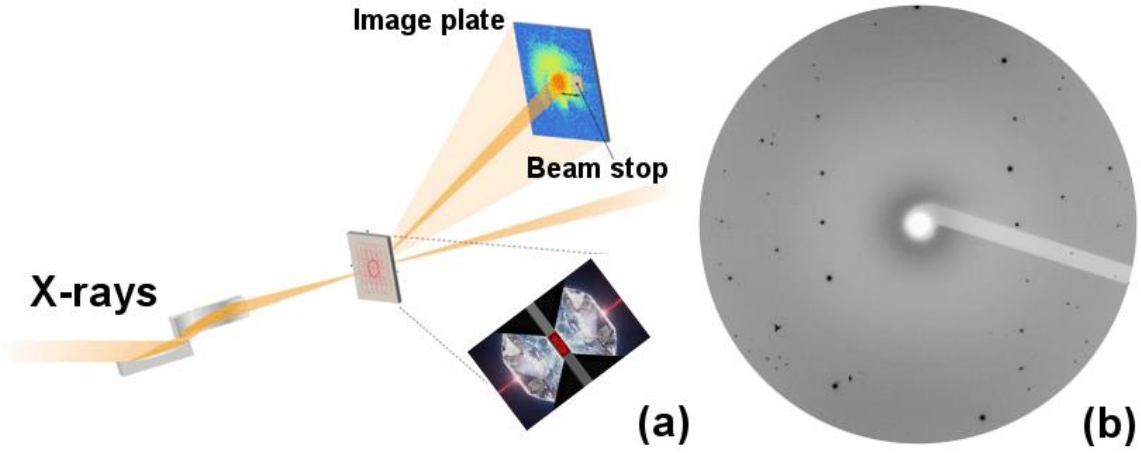

Figure 2.8. Workflow for solving the structure of a high pressure sample. (a) A schematic procedure for solving the structure of compressed sample. (b) Two dimensional X-ray diffraction pattern of a single crystal coesite sample. Deriving from the Bragg's law, the incoming beam is deflected by an angle according to the reciprocal lattice vectors of sample, producing reflection spots on the image plate.

Since the wavelength of hard X-rays are close to the magnitude of atomic spacing in molecules and condense matters, it can be used as a tool to identify the structure of a crystal, in which the crystalline atoms cause a beam of incident X-rays to diffract into many specific directions. In light of the Bragg's law, the incident beam is deflected in the angle θ based on the spacing d between the diffraction planes:

$$2d \sin\theta = n\lambda \tag{2.59}$$

where λ is the wavelength of the beam and n is any integer. High energy incident beam diffracts on the sample in DAC, received by the image plate behind it (Fig. 2.8a). The diffraction pattern is spotty like from our single crystal samples and each spot represents a specific plane in its reciprocal space (Fig. 2.8b).

Experiment is initialized by focusing the beam to the rotational center of the sample. A pre-scan is necessary to avoid those angle positions that the diffraction signals were mostly absorbed by diamonds. Diffraction patterns are collected onto a plate detector at each X-ray incident angle (1^o per image) typically from -15^o to 15^o. An additional image scanning over the same range of scattering angle is taken to show the integrated 2D diffraction pattern. The single crystal structure and its orientation matrix are calculated by the difference vector approach implemented in the package GSE_ADA[62]. The mathematical details including predicting and refining crystalline structure from reciprocal vectors can be found in a book reference[63].

REFERENCE

1. Hohenberg, P. & Kohn, W. Inhomogeneous electron gas. *Phys. Rev*. **136**, B864-B871 (1964).

2. Kohn, W. & Sham, L. J. Self-consistent equations including exchange and correlation effects. *Phys. Rev.* **140**, A1133-A1138 (1965).

3. Parr, R. G. Density functional theory. *Ann. Rev. Phys. Chem.* **34**, 631-656 (1983).

4. von Barth, U. Basic density-functional theory-an overview. *Phys. Scripta*. **T109**, 9-39 (2004).

5. Sprik, M. *Classical and Quantum Dynamics in Condensed Phase Simulations,* Ch. 13, Pg. 285-309, (World Scientific, Singapore, 1985).

6. Jones, R. O. & Gunnarsson, O. The density functional formalism, its applications and prospects. *Rev. Mod. Phys.* **61**, 689-746 (1989).

7. Jones, R. O. & Gunnarsson, O. Density functional formalism: sources of error in local-density approximations. *Phys. Rev. Lett.* **55**, 107 (1985).

8. Perdew, J. P. & Wang, Y. Accurate and simple analytic representation of the electron-gas correlation energy. *Phys. Rev. B* **45**, 13244-13249. (1992).

9. Sim, F., St-Amant, A., Papai, I. & Salahub, D. R. Gaussian density functional calculations on hydrogen-bonded systems. *J. Am. Chem. Soc.* **114**, 4391-4400 (1992).

10. Juan, Y-M. & Kaxiras, E. Application of gradient corrections to desity-functional theory for atoms and solids. *Phys. Rev. B* **48**, 14944-14952 (1993).

11. Johnson, B. G., Gill, P. M. W. & Pople, J. A. The performance of a family of density functional methods. *J. Chem. Phys.* **98**, 5612-5626 (1993).

12. Ernzerhof, M & Scuseria, G. E. Assessment of the Perdew-Burke-Ernzerhof exchange-correlation functional. *J. Chem. Phys.* **110**, 5029-5036 (1999)

13. Cohen. A. J. & Handy, N. C. Assessment of exchange correlation functionals. *Chem. Phys. Lett.* **316**, 160-166 (2000).

14. Staroverov, V. N., Scuseria, G. E., Tao, J. & Perdew, J. P. Erratum: “Comparative assessment of a new nonempirical density functional: molecules and hydrogen-bonded complexes”. *J. Chem. Phys.* **121** 11507 (2004).

15. Staroverov, V. N., Scuseria, G. E., Tao, J. & Perdew, J. P. Erratum: Tests of a ladder of density functional for bulk solids and surfaces. *Phys. Rev. B* **69**, 075102 (2004).

16. Born, M. & Oppenheimer, J. R. Zur Quantentheorie der Molekeln, *Annalen der Physik*, **389**, 457–484 (1927).

17. Hartree, D. R. The wave mechanics of an atom with a non-coulomb central field. *Proc. Camb. Phil. Soc,* **24**, 89-132 (1928).

18. Fock, V. A. Näherungsmethode zur Lösung des quantemechischen Mehrkörperproblems. *Z. Phys.* **61**, 126-148 (1930).

19. Slater, J. C., A Simplification of the Hartree-Fock Method , *Phys. Rev.* **81**, 385-390 (1951).

20. Zunger, A. & Cohen, M. L. Density-functional pseudopotential approach to crystal phase stability electronic structure. *Phys. Rev. Lett.* **41**, 53 (1978).

21. Hamann, D. R., Schluter, M. & Chiang, C. Norm-conserving pseudopotentials. *Phys. Rev. Lett.* **43**, 1494 (1979).

22. Kerker, G. P. Non-singular atomic pseudopotentials for solid state applications. *J. Phys. C* **13**, L189 (1980).

23. Bachelet, G. D., Hamann, D. R. & Schluter, M. Pseudopotentials that work: from H to Pu. *Phys. Rev. B* **26**, 4199 (1982).

24. Vanderbilt, D. Optimally smooth norm-conserving pseudopotentials. *Phys. Rev. B* 32, 8412 (1985).

25. Goedecker, S., Teter, M. & Hutter, J. Separable dual-space Gaussian pseudopotentials. *Phys. Rev. B* **54**, 1703-1710 (1996).

26. Blöchl, P. E. Projectpr augmented-wave method. *Phys. Rev. B* **50**, 17953-17979. (1994)

27. Blöchl, P. E., Först, C. J. & Schimpl, J. Projector augmented wave method: ab initio molecular dynamics with full wave functions. *B. Mater. Sci.* **26**, 33-41 (2003).

28. Valiev, M. & Weare, J. M., The projector-augmented plane wave method applied to molecular bonding. *J. Phys. Chem. A* **103**, 10588-10601 (1999).

29. Davidon, W. C. Variable metric method for minimization. *SIAM J. Appl. Math.* **1**, 1-17 (1991).

30. Avriel, M. *Nonlinear Programming: Analysis and Methods*, Ch. 11 (Dover publishing, 2003).

31. Verlet. L. Computer experiments on classical fluids. *Phys. Rev.* **159**, 98 (1967).

32. Nosé, S. A unified formulation of the constant temperature molecular dynamics methods, *J. Chem. Phys.* **81**. 511 (1984).

33. Hoover, W. G., Canonical dynamics: equilibrium phase-space distributions. *Phys. Rev. A* **31**, 1695 (1985)

34. Martyna, G. J., Tobias, D. J. & Klein, M. L. Constant pressure molecular dynamics algorithms. *J. Chem. Phys.* **101**, 4177 (1994).

35. Parrinello, M. & Rahman, A. Crystal structure and pair potentials: a molecular dynamics study. *Phys. Rev. Lett.* **45**, 1196-1199 (1980).

36. Parrinello, M. & Rahman, A. Strain fluctuations and elastic constants. *J. Chem. Phys.* **76**, 2662 (1982).

37. Wentzcovitch, R. M. Invariant molecular-dynamics approach to structural phase transitions. *Phys. Rev. B* **44**, 2358 (1991).

38. Lill, J. V. & Broughton, J. Q. Nonlinear molecular dynamics and Monte Carlo algorithms *Phys. Rev. B* **46**, 12068 (1992).

39. Rajappa, C., Sringeri, S. B., Subramanian, Y. & Gopalakrishnan, J. A molecular dynamics study of ambient and high pressure phases of silica: Structure and enthalpy variation with molar volume. *J. Chem. Phys.* **140**, 244512 (2014).

40. Car, R. & Parrinello, M. Unified approach for molecular dynamics and density-functional theory. *Phys. Rev. Lett.* **55**, 2471-2474 (1985)

41. Mermin, N. D. What's wrong with this Lagrangian. *Phys. Today*, **41**, 4, 9 (1988).

42. Remler, D. K. & Madden, P. A. Molecular-dynamics without effective potentials via the Car-Parrinello approach. *Mol. Phys.* **70**, 921-966 (1990).

43. Bornemann, F. A. & Schütte, C. Adaptive accuracy control for Car-Parrinello simulations. *Number. Math.* **78**, 359-376 (1998).

44. Marx, D., Tuckerman, M. E. & Martyna, G. J. Quantum dynamics via adiabatic *ab initio* centroid molecular dynamics. *Comput. Phys. Comm.* **118**, 166-184 (1999).

45. Laio, A. & Parrinello, M. Escaping free energy minima. *Proc. Natl. Acad. Sci.*, **99**, 12562 (2002).

46. Laio, A. & Gervasio, F. L. Metadynamics: a method to simulate rare events and reconstruct the free energy in biophysics, chemistry and material science. *Rep. Prog. Phys.*, **71**, 126601 (2008).

47. Ensing, B., Laio, A., Parrinello, M. & Klein, M. L. A recipe for the computation of the free energy barrier and the lowest free energy path of concerted reactions. *J. Phys. Chem. B.* **109**, 6676-6687 (2005).

48. Jónsson, H., Mills, G. & Jacobsen K. W. *Classical and Quantum Dynamics in Condensed Phase Simulations*, Pg. 385-404, (World Scientific, Singapore, 1998).

49. Sheppard, D., Xiao, P., Chemelewski, W. & Johnson, D. D. A generalized solid-state nudged elastic band method. *J. Chem. Phys.* **136**, 074103 (2012).

50. Sheppard, D., Terrell, R. & Henkelman, G. Optimization methods for finding minimum energy paths. *J. Chem. Phys.* **128**, 134106 (2008).

51. G. Kresse & J. Furthmüller. Efficiency of *ab*-initio total energy calculations for metals and semiconductors using a plane-wave basis set. *Comput. Mat. Sci.* **6**, 15 (1996).

52. G. Kresse & D. Joubert. From ultrasoft pseudopotentials to the projector augmented-wave method. *Phys. Rev. B* **59**, 1758 (1999).

53. W. E & P. B. Ming, Cauchy-Born rule and the stability of crystalline solids: static problems, *Arch. Ration. Mech. Anal.* **183**, 241-297 (2007).

54. Grimvall, G., Köpe, B. M., Ozolins, V. & Persson, K. A., Lattice instabilities in metallic elements, Rev. Mod. Phys. **84**, 945 (2012).

55. Beijing Grish Co., Ltd. http://bjgrish2009.en.made-in-china.com

56. Eremets, M. I. & Troyan. I. A. Conductive dense hydrogen. *Nat. Mater.* **10**, 927-931 (2011).

57. Zha, C-S., Cohen, R. E., Mao, H-K. & Hemley, R. J. Raman measurements of phase transitions in dense solid hydrogen and deuterium to 325 GPa. *Proc. Nat. Acad. Sci.* **111**, 4792-4797 (2014).

58. Jephcoat, A. P., Mao, H-K. & Bell, P. M., *Hydrothermal Experiment Techniques* Ch. 11, (Wiley-interscience, New York, 1987).

59. Almax easyLab official website. http://www.almax-easylab.com

60. Iwanenko D. & Pomeranchuk I. On the maximal energy attainable in betatron, *Phys. Rev.* **65**, 343 (1944).

61. Elder, F. R., Gurewitsch, A. M., Langmuir, R. V. & Pollock, H. C. Radiation from Electrons in a Synchrotron, *Phys. Rev.* **71**, 829-830 (1947).

62. Dera, P., *et al.* High pressure single-crystal micro X-ray diffraction analysis with GSE_ADA/RSV software. *High Pressure Res*. **33**, 466-484 (2013)

63. Carpenter, G. B. *Principles of Crystal Structure Determination*. Ch. 11-12, (W. A. Benjamin, INC. New York, 1964).

III. A NEW PHASE TRANSITION MECHANISM IN COMPRESSED COESITE

3.1 X-ray diffraction experiment

3.1.1 Experimental setup

In order to determine the crystalline structure of coesite under pressure, multiple XRD experiments were performed on coesite single crystals. The typical sample size is (W)40 μm×(L)40 μm×(T) 10μm, synthesized using a multi-anvil apparatus[1]. The crystal orientation was determined *in situ*. The advantages of using single crystal samples have been discussed in chapter 2.6.3. Experiments were mainly conducted at the 16 IDB station of High Pressure Collaborative Access Team (HPCAT) of the Advanced Phonon Source (APS), Argonne National Laboratory (ANL). At the time of experiment, the X-ray beam has a wavelength of 0.4066 Å, equivalent to 30.5 keV in beam energy.

The single crystal coesite sample was loaded into in a tungsten gasket with hole diameter 170 μm, seated on a 300 μm culet. To ensure the best hydrostatic condition, helium gas was employed as the pressure medium. Since helium gas is extremely compressible, the hole size shrank by more than half (measured in diameter) after gas loading (Fig. 3.1).

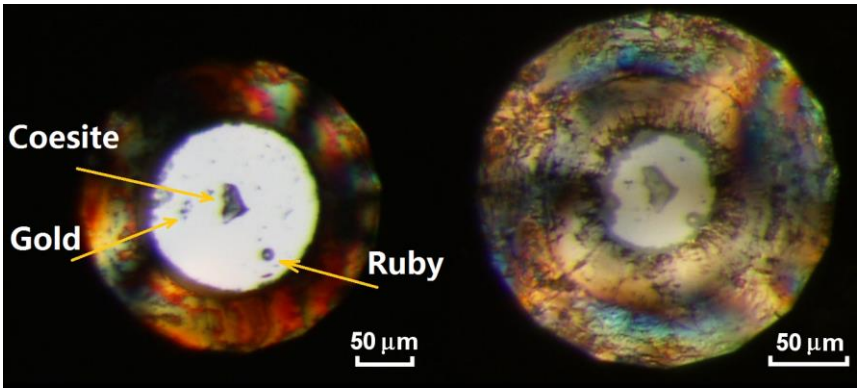

Figure 3.1. Microscopic images of coesite sample loaded in a DAC: before (left) and after (right) aerating pressure medium. One ruby ball and gold powders (indicated by golden arrows) were loaded along with the coesite sample for pressure calibration. The gasket hole size, decreased from 170 μm to around 80 μm after filling helium gas. The equilibrated pressure was around 1.7 GPa.

Pressure was calibrated *in situ* based on the equation of state of gold powders and ruby fluorescence line shift in an off-line hutch. The uncertainty in the pressure measurement is ±0.80 to 1.98 GPa, derived from the pressure change within each experiment interval.

3.1.2 Coesite single crystal

Fig. 3.2 shows an indexed 2D diffraction pattern from one coesite sample at 6 GPa. The diffraction images were processed in such a way that the strongest diffraction peaks from coesite sample were included but most saturated diamond peaks were masked out. Since strong diamond diffraction signals traveling through the seat can cause secondary powder diffraction (*i.e.*, Debye-Scherrer rings which are centered on the given diamond peaks[2]), the way the image is processed is for clarity purposes.

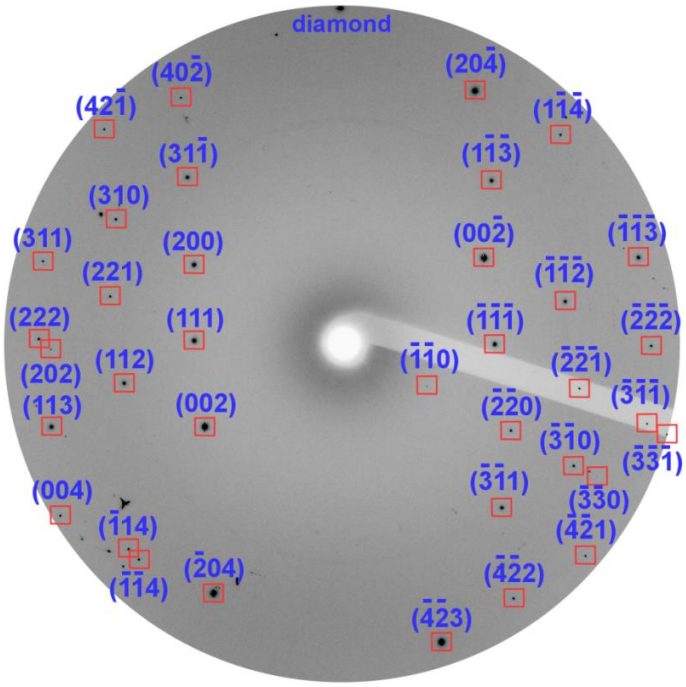

Figure 3.2. An indexed 2D diffraction pattern of coesite at 6 GPa. All major peaks were refined to a monoclinic coesite structure with space group C2/c, as labeled in red boxes. The index (hkl) denotes a plane orthogonal to a direction (h, k, l) in the basis of the reciprocal lattice vectors.

In short, the d-spacing values of the spots in the graph are larger than 1.30 Å. Diffraction peaks less than 1.30 Å in d-spacing are still tractable, which are indexed in the original raw images. At 6 GPa all diffraction peaks are readily indexed to a monoclinic coesite structure, where sharp single crystal patterns are clearly shown. The dark ring at the image center and some other minor spots are due to either defects on the image plate or the beam pinhole.

3.1.3 Ostensible amorphization of coesite

The sharp coesite diffraction pattern persists up to 26 GPa, when all original coesite

diffraction spots split into multiple sharp spots (Fig. 3.3). The zoomed-out section of peak (111) is also displayed in the left panel of Fig 3.4, where at 26 GPa three extra spots emerge with different d-spacing values and such a split phenomenon remains visible until around 40 GPa.

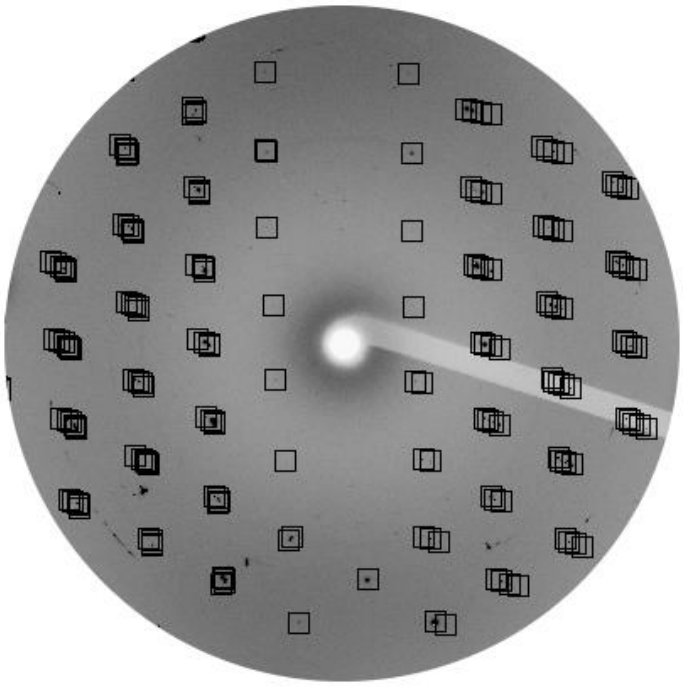

Figure 3.3. A split 2D diffraction pattern of single-crystal coesite sample compressed at 26 GPa. The black boxes were indexed to four intermediated silica phases that have a topotaxial relationship with its parent coesite structure.

The diffractions spots do not split along the same diffraction ring, suggesting the creation of multiple crystalline structures rather than a crashed crystal with different orientations. The diffraction pattern after splitting can be uniquely fit into four distinct but nearly isochoric structures (Fig. 3.5). Their orientations, as summarized in Table 3.1,

although close to each other, are unique in their own rights. The lattice parameters of each metastable phase at 26 GPa are solved one by one. The lattice parameters at a lower pressure are taken as the seed to search for the closest structure from the split pattern. The indexed peaks from the search are removed from the pattern and the search continues for the next structure until the diffraction peaks are fully indexed. The diffraction peaks are eventually completely covered by the assembly of four triclinic structures. It is found that those isovolumetric metastable phases have a topotaxial relationship with the parent coesite crystal, as the *a* and *c* axis were distorted, resulting in triclinic structures (Table 3.2).

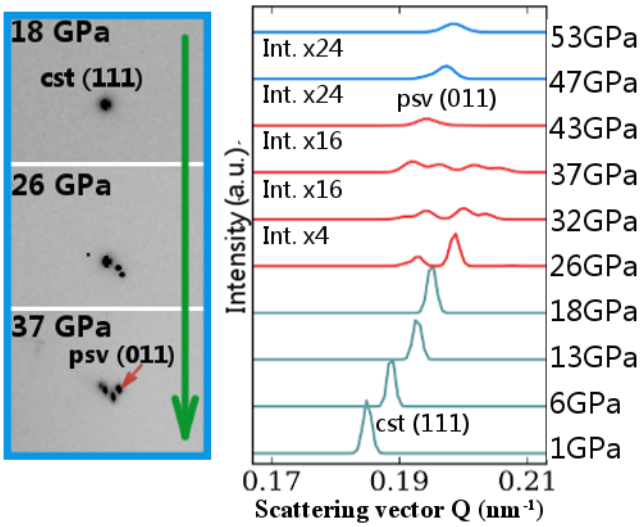

Figure 3.4. The evolution of the selected (111) diffraction peak from coesite during compression. Left figure: changes of coesite (111) peak at 18 GPa, 26 GPa and 37 GPa, respectively, as it splits into 4 spots. Right figure: the evolution of integrated 1-D diffraction spectrum of the (111) peak up to 53 GPa. The peaks are widened by one magnititude and their intensities are significantly lowered.

Table 3.1. Orientation parameters for the metastable phases at 26 GPa, in comparison with coesite single crystal at 18 GPa. The orientation variation of the metastable phases is finite in comparison with the parent coesite single crystal. The meanings of the rotation angles (Ω, Φ and X) characterizing the orientation of the crystals are illustrated in the picture on the right.

	Ω	Φ	X
M1	20.48(4)	0.93(4)	102.14(2)
M2	17.09(3)	0.55(2)	106.88(1)
M3	22.34(5)	-1.73(2)	106.78(0)
M4	6.64(4)	-3.58(1)	101.59(0)
18 GPa	9.39(1)	-4.71(2)	109.94(0)

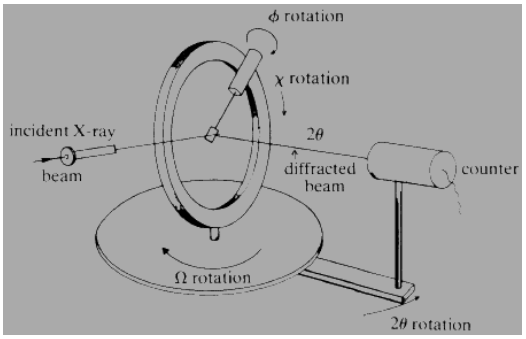

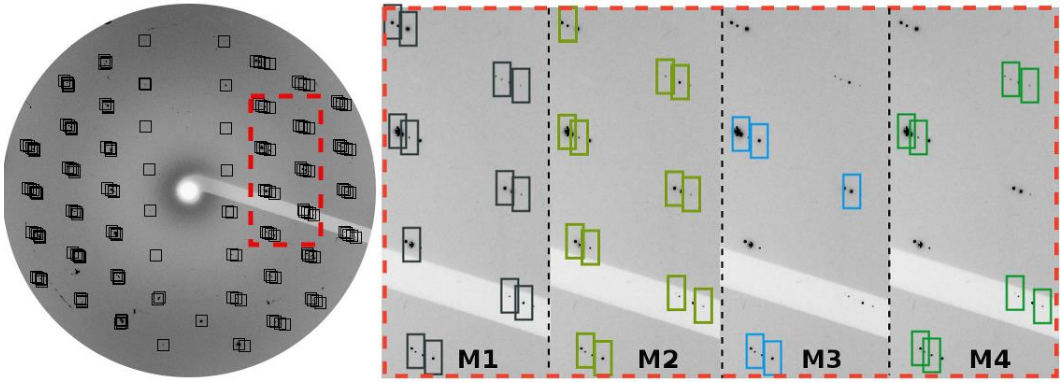

Figure 3.5. Four copies of the highlighted diffraction pattern at 26 GPa, taken from the red dashed box on the left 2D pattern. The contributions from the four individual metastable structures (M1-M4) are highlighted in different colors (right figure).

Table 3.2. Lattice parameters of the four distinct metastable structures at 26 GPa determined from the experiment. The triclinic metastable structures have a reduced symmetry compared to coesite.

	a (Å)	b (Å)	c (Å)	α	β	γ	V (Å^3/SiO_2 unit)
M1	6.572(8)	12.085(2)	6.585(1)	98.20(0)	117.64(3)	98.43(2)	27.81(4)
M2	6.572(7)	11.715(3)	6.585(2)	94.08(1)	117.63(5)	94.38(2)	27.79(5)
M3	6.572(9)	11.715(3)	6.813(2)	94.03(0)	121.09(4)	94.03(2)	27.79(5)
M4	6.573(8)	11.599(2)	6.812(2)	90.16(0)	121.10(3)	90.06(1)	27.80(4)

It is notable that this phenomenon is in contrast to the reported formation of an intermediate amorphous phase[3], where diffraction peaks might be just too weak to be detected from the image plate. The peak widening, accompanying with the split of diffraction spots, results in much lowered diffraction intensities (Fig. 3.4). At 40 GPa, the peak intensities have decreased by almost one order of magnitude, resembling the pressured-induced amorphization phenomenon reported earlier[3,4]. We conjecture that the ostensible amorphization behavior reported in earlier works might be due to either low X-ray diffraction intensities or low detector sensitivity.

3.1.4 Coexistence of metastable phases and post-stishovite

A new set of diffraction pattern from a denser silica phase appeared at 32 GPa and coexisted with the existing metastable phases. At those pressures the spatial resolution of the single crystal diffraction pattern is insufficient to resolve any new distorted crystal structures, which however can be mitigated by integrating the spotty patterns into 1D diffraction spectrums. At 37 GPa, whereas peaks from the metastable phases are still

strong, new peaks appear and are highlighted in Fig. 3.6 (red arrows in the 2D diffraction pattern and red stars in the integrated spectrum plot).

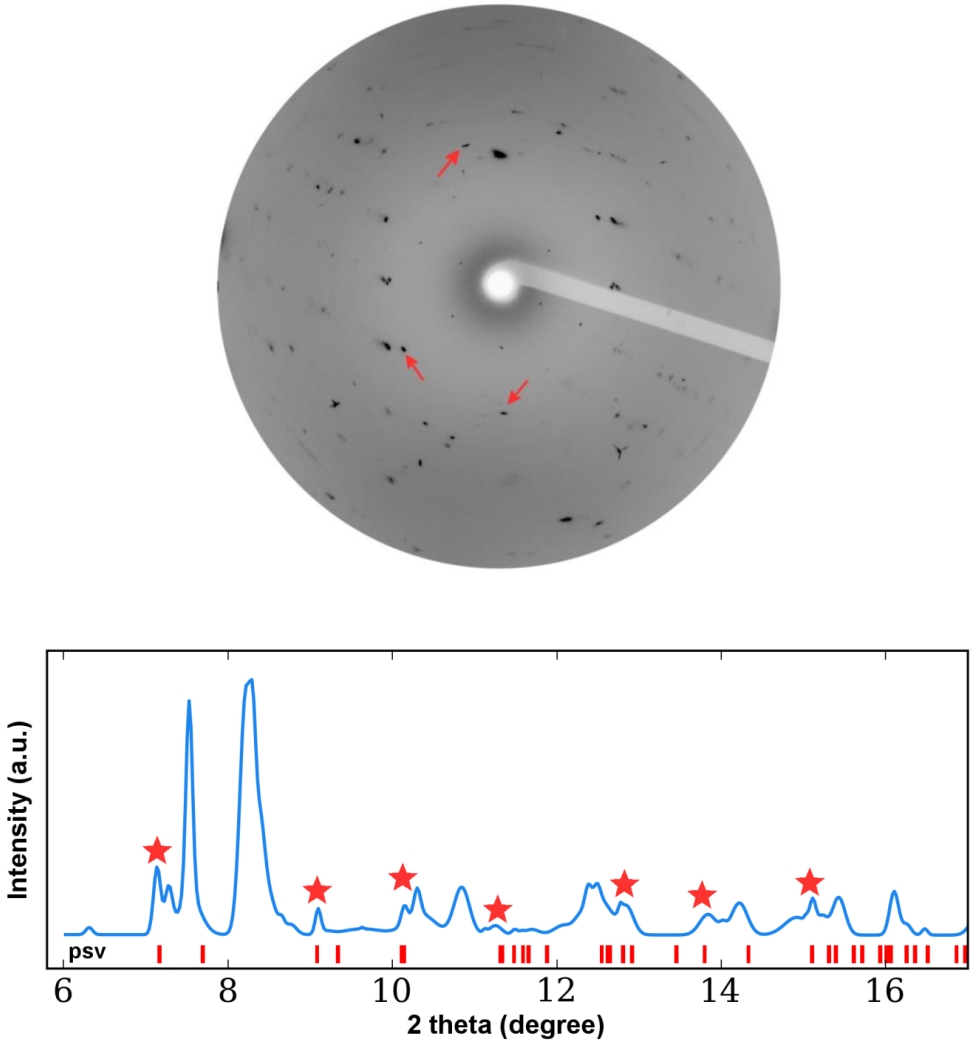

Figure 3.6. X-ray diffraction pattern for compressed coesite at 37 GPa. The 2D single crystal pattern (top graph) contains a phase mixture of the metastable silica phases and a new phase (indicated by red arrows). The integrated diffraction spectrum (bottom graph) is indexed to the later resolved post-stishovite phase (red stars and bars).

The majority of the diffraction peaks at 40 GPa are contributed from the metastable phases, but the new peaks are later confirmed to be a monoclinic type post-stishovite structure (space group P2/c, *e.g.*, crystallographic data at 40 GPa is summarized in Table 4.3), corresponding to a new phase with a higher density. The post-stishovite phase is stable up to 53 GPa (the highest pressure achieved in this work) at room temperature and is clearly different from either the monoclinic coesite structure or the triclinic metastable structures discovered in Figure 3.4.

Table 3.3. Lattice parameters of monoclinic post-stishovite at 40 GPa. The experiment data was obtained at 300 K. The simulation data was extracted from *ab initio* metadynamics simulation followed by complete geometric relaxation (including cell parameters and atom positions) at 0 K. The differences of the lattice parameters between experiment and simulation are less than ~3%, which falls within the accuracy of first-principles calculations.

	Simulation	Experiment
Space group	P2/c	P2/c
Z	4	4
a (Å)	3.869(5)	4.002(2)
b (Å)	4.342(3)	4.589(2)
c (Å)	4.949(3)	4.651(4)
β	91.58(2)	92.50(5)
ρ (g/cm^{-3})	4.80(1)	4.68(0)

First-principles calculations at similar conditions were carred out and the resutls were compared with my experiments. The silicon six-coordinated post-stishovite is confirmed by *ab initio* molecular dynamics simulation with the metadynamics algorithm

and the results will be discussed in section 3.3. The lattice parameters and the density of the new structure emerging from metadynamics are provided in Table 3.3. The structures are geometrically optimizated by the quasi-Newton algorithm to reach the local energy minimum. The calcualted results exhibit a reasonably good match with the experiments, where the difference in lattice parameters falls within the error of first-principles calculations (~2% in terms of lattice parameters).

3.1.5 The monoclinic type post-stishovite

The diffraction signals from the metastable phases completely disappear above 45 GPa. The remaining diffraction spots corresponding to the post-stishovite phase persist up to the highest experimental pressure at 53 GPa (Fig 3.7). To resolve the lattice parameters, the crystal structure from *ab initio* MD is taken as the initial seed for structural refinement. Again, those visible peaks can be indexed into the above-mentioned monoclinic post-stishovite phase, whose structure is distinctly different from the α-PbO_2[5] and ZrO_2[6] types of post-stishovite structure reported in the literature.

The diffraction pattern calculated from *ab initio* simulations is corrected for Lorentz, polarization and multiplicity factors to compare with the observed pattern. The extra experimental peaks highlighted by the green crosses are possibly contributed from α-PbO_2-type silica residuals, shown by the small ticks at the bottom. The peak positions of the α-PbO_2-type silica are obtained based on its equation of state provided by the *X-ray helper* program at Advanced Photon Source, Argonne National Laboratory. The *ab initio* simulation results match the observations from the single-crystal XRD experiment, suggesting that the new silica phase can be stable in the medium-lower mantle of the

Earth.

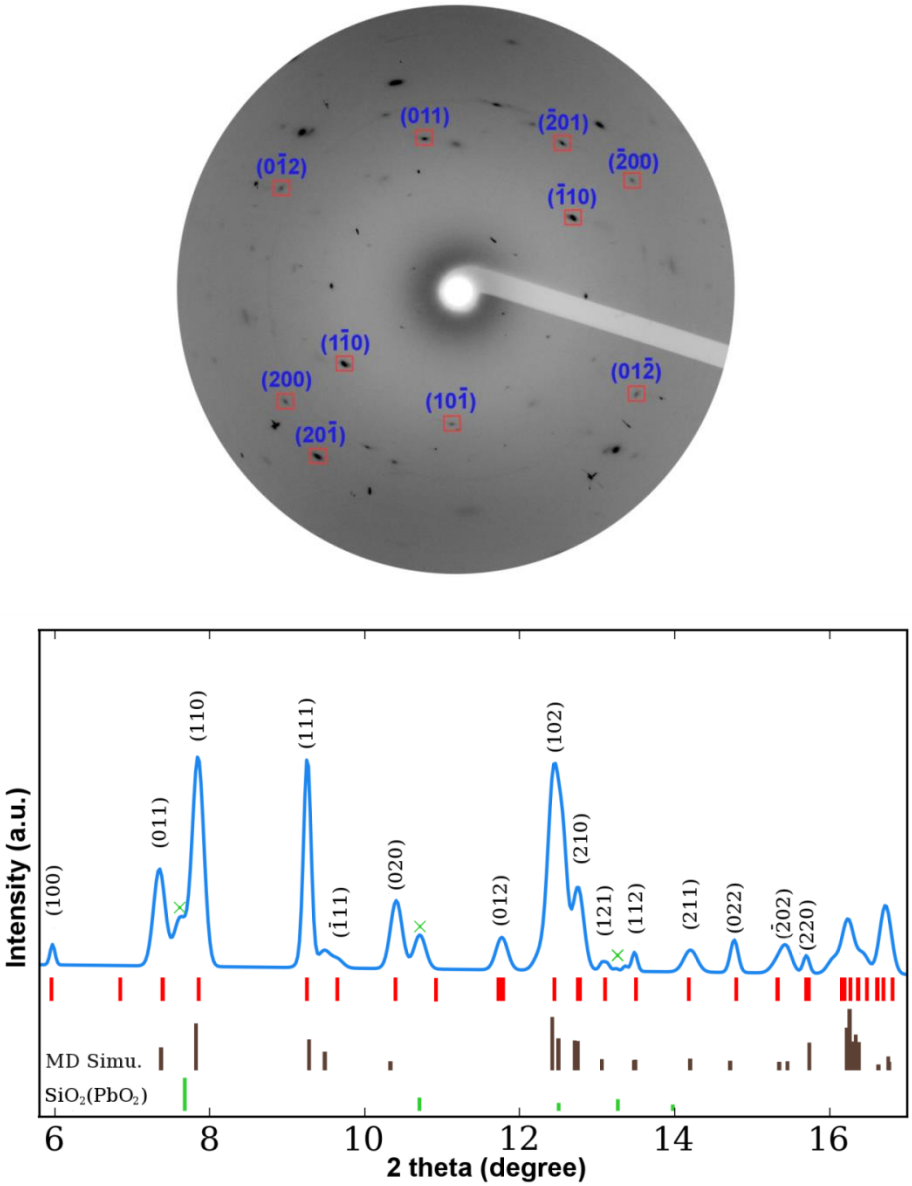

Figure 3.7. Energy-dispersive X-ray diffraction patterns of coesite at 53 GPa. The 2D pattern of the monoclinic post-stishovite (indexed for one grain) is shown in the upper figure. Its integrated spectrum fits to the post-stishovite phase (red bars with indexed hkl). The diffraction patterns of MD-simulated post-stishovite and the residual α-PbO_2-type silica phase are indicated by the brown and green bars, respectively.

3.1.6 The evolution of coesite X-ray diffraction patterns

In summary, from the energy dispersive X-ray diffraction experiment on single crystal coesite, we find the transformation from the coesite phase to four intermediate metastable phases, *en route* to the monoclinic type post-stishovite phase (Fig 3.8).

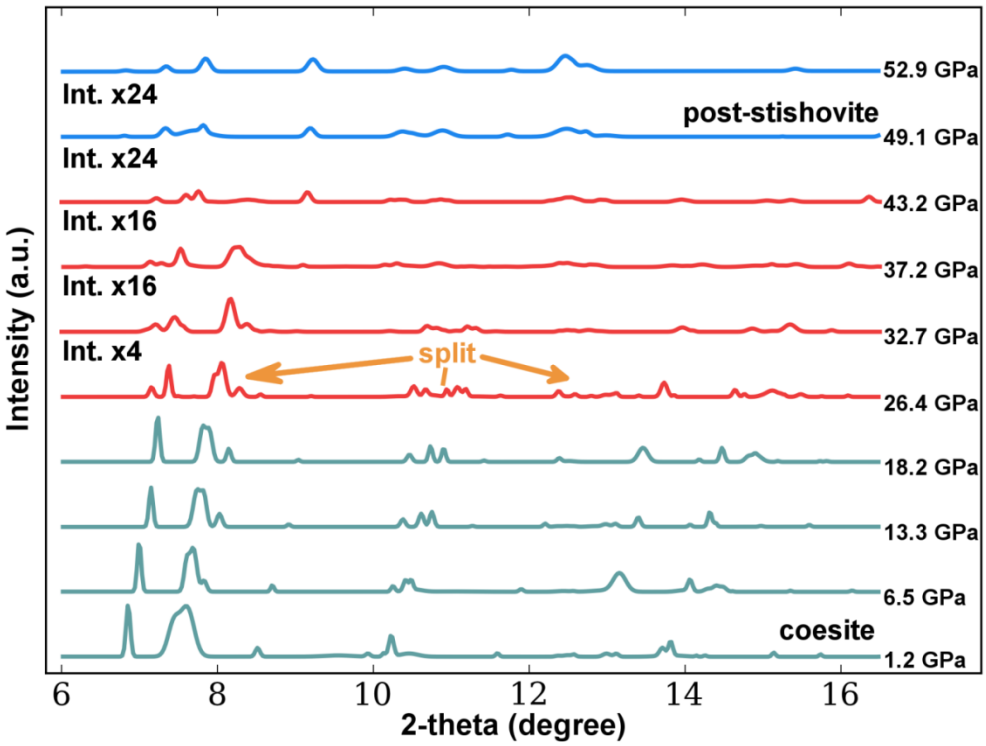

Figure 3.8. Evolution of coesite X-ray diffraction spectrum up to 53 GPa. Starting from the coesite phase (1.2~18 GPa, space group C2/c), coesite transform into the coexistence of four triclinic metastable structures (26~43 GPa) and the monoclinic type post-stishovite phase (32~53 GPa space group P2/c). The split of the original coesite peaks is observed at 26 GPa, resembling an ostensible amorphization process. The spectrums in the red color indicate the region where silica metastable structures are discernible in the experiment. The blue colored spectrums correspond to the new post-stishovite phase. The intensities of all spectrums are all scaled to fit the figure size as indicated by the scaling factors in the figure.

The isovolume intermediate phases, coexisting in the pressure range of 26-43 GPa at room temperature, are manifested by the split of the peaks with different d-spacing values. Peak intensities are significantly reduced at high pressures (Fig 3.8). With the help of first-principles modeling, a new monoclinic post-stishovite phase has been identified. The experiment indicates that the four-coordinated coesite phase eventually transforms to six-coordinated post-stishovite, consistent with previous studies[7,8]. Such a coordination transition is believed to be common to the silica family and silicates upon compression[9-11].

From the single-crystal experiments, a new phase transition pathway of coesite is identified, featuring the formation of multiple intermediate phases. By compressing coesite single crystals at room temperature, four metastable phases are captured in the pressure range of 26~43 GPa. Such a phenomenon may have been mistakenly interpreted as an amorphization behavior in the past due to poor signal resolution in the experiment. It is the first time to demonstrate how coesite transits into the six-coordinated post-stishovite phase at room temperature.

3.2 Equations of state

3.2.1 Quantum ESPRESSO setup

The equations of state for coesite and post-stishovite have been evaluated by optimizing the structure at different pressures based on first-principles methods. The geometric optimization was conducted in the framework of DFT with the simulation package Quantum ESPRESSO ver. 5.0.1[12]. The generalized gradient approximation

under the Becke-Lee-Yang-Parr parametrization was implemented to describe the exchange corelation functional[13,14]. For silica, 4 valence electrons were considered for Si atoms ($2s^2 2p^2$) and 6 for O atoms ($2s^2 2p^4$). A plane-wave basis set with kinetic energy cut off of 150 Ry (~2041 eV) was found sufficient to converge the total energy less than 2.7×10^{-7} eV, and the forces acting on each atom less than 0.05 eV/Å. The Monkhorst mesh of *k*-points sampling the Brillouin zone were summarized in the following table:

Table 3.4. Structural properties and *k*-points meshes for coesite and post-stishovite.

	Z	Space group	*k-points* mesh	# irreducible *k-points*
coesite	16	C2/c	3×3×3	14
post-stishovite	4	P2/c	3×3×3	14

Hydrostatic pressure was applied by adding the pulay stress to the diagonal elements of the stress tensor. At each pressure, the system was optimized for atomic position, cell shape and cell volume. The resultant external pressure is within 0.1 GPa difference of the targeting pressure, confirming the optimization is in good accuracy.

3.2.2 Experimental and computational equations of state

The experimental equations of state for compressed coesite are compared with my first-principles geometric optimization results in Fig. 3.9:

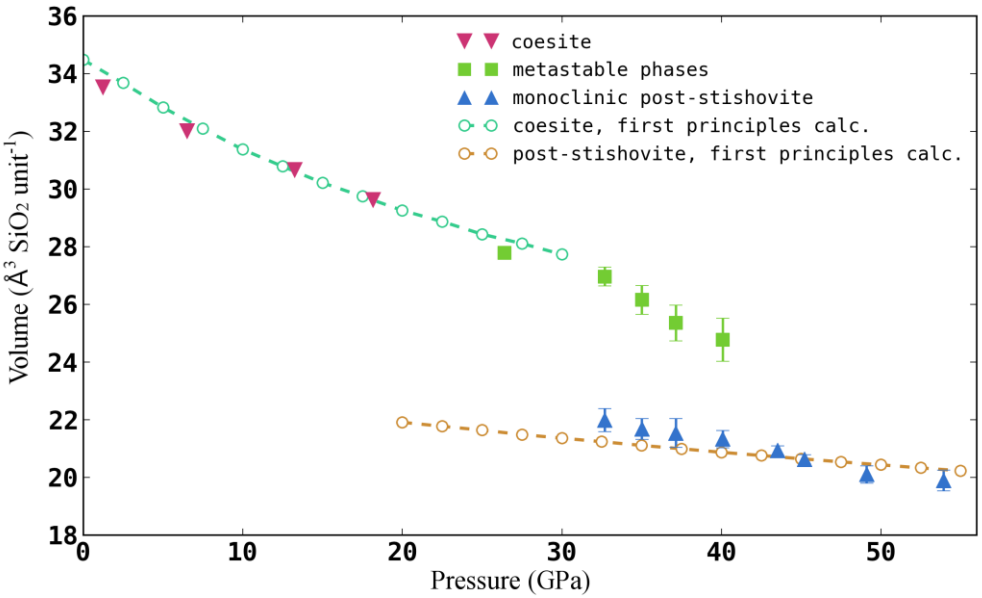

Figure 3.9. The specific volume of coesite as a function of pressure during the compression experiment. The color markers are: coesite (magenta down triangles), metastable transition intermediates (green squares) and monoclinic post-stishovite (blue triangles). The experimental data are compared with first-principles calculations of the equations of state (EOS) of coesite (consistent with the experimental EOS[14,15]) and monoclinic post-stishovite.

The simulated equations of state are found to match the experimental data very well, with an accuracy of 3% in terms of volume. The intermediate phases appearing at the 26 GPa deviate from the EOS of coestie, with an additional 2% volume collapse. Such a volume collapse becomes more pronounced at higher pressures (*e.g.*, 35 GPa). Due to poor diffraction signals from the metastable structures at those pressures, however, their volumes cannot be accurately determined. The volume of the monoclinic

post-stishovite phase is comparable with the static calculations in general. The experimentally solved volumes in the range of 32-40 GPa are slightly higher than the predicted values, which presumably, as mentioned in the literature[4], is due to defects generated during the phase transition.

3.2.3 Structural evolution in compressed coesite

The structural representations are extracted from the MD simulations followed by geometric optimization at 0 K. The following graphs demonstrate the structural evolution from coesite (Fig. 3.10) to the metastable silica phases (Fig. 3.11), eventually to the monoclinic post-stishovite phase (Fig. 3.12).

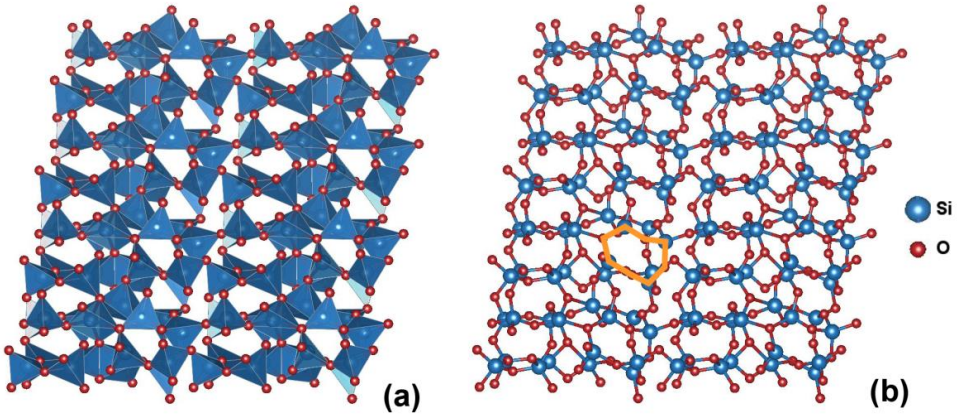

Figure 3.10. Structural representation with polyhedra of coesite at 20 GPa. The 4×2×4 supercell is projected along the c-axis. The polyhedra representation is shown in the left figure and the wired framework representation is shown in the right figure. Corner-sharing tetrahedra are colored in blue. One signature four-member ring of coesite is sketched out by the orange solid line in the wired structure.

Coesite is a high-pressure polymorph of silica and was first synthesized from dry

sodium metasilicate and diammonium at 3.5 GPa and 750 K[16]. The silica units are arranged in corner linked tetrahedra, the same Si-O unit as α-quartz. One monoclinic coesite unit cell contains a total number of 48 atoms, signified by its 4-silica-member rings (Fig. 3.10b). From the simulation, the four-member rings are distorted to compensate the volume change during compression, which has been explained by Angel *et al.* as the anomalous compression in coesite[17,18]. From the experiment, splitting peaks appear at 26 GPa as a result of symmetry-breaking, indicating that the atomic structure of coesite has changed.

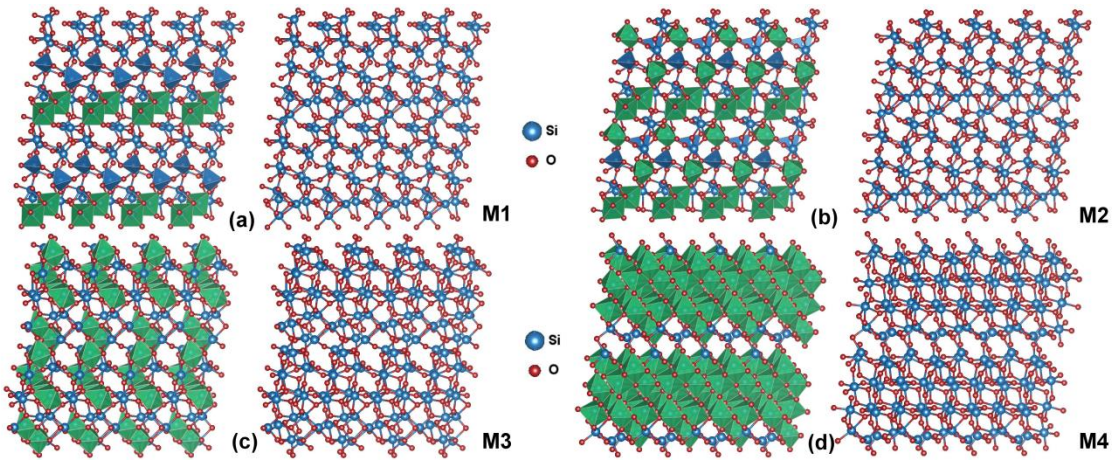

Figure. 3.11. Structural evolution of the four silica metastable phases at 40 GPa. The 4×2×4 supercell is projected along the c-axis. Structure representations with polyhedra are shown on the left while the ball-and-stick model structures are shown on the right. Silica tetrahedra are colored in blue and six-coordinated octahedra are colored in green. Four intermediate phases are numbered in the order in which the transition sequence was observed in the metadynamics simulation.

3.2.4 Four metastable structures

Four metastable phases (M1-M4, see Fig. 3.11) have been observed in both experiment and simulation. Starting from the four-coordinated coesite phase, the number of six-coordinated silica unit gradually increases. Five-coordinated polyhedra are also captured as the intermediate network to help stabilize the system. Their lattice parameters are summarized in Table 3.5. The structures are optimized at 40 GPa. Whereas the exact one-to-one correspondence of the metastable structures from the experiment and the computation is difficult to come by, the softening of the *c*-axis and the overall changes of the lattice parameters have been well reproduced by simulation.

Table 3.5. Lattice parameters of the four distinct metastable structures at 40 GPa determined from the simulation. The triclinic metastable structures were optimized at 0 K and their errors were estimated from the fluctuation of molecular dynamics.

	a(Å)	b(Å)	c(Å)	α	β	γ	V ($Å^3/SiO_2$ unit)
M1	6.20(7)	11.14(14)	6.01(8)	96.81(10)	117.57(11)	92.78(9)	22.69(28)
M2	6.21(5)	11.04(9)	6.05(5)	97.11(3)	117.32(7)	92.97(5)	22.67(19)
M3	6.26(8)	10.59(12)	6.45(8)	95.95(8)	124.51(12)	91.58(8)	21.76(27)
M4	6.29(7)	10.45(11)	6.54(6)	94.91(6)	124.37(8)	95.78(4)	21.72(22)

3.2.5 The monoclinic post-stishovite structure

The monoclinic post-stishovite phase (*Z*=4, space group P2/c) is the most compressed phase among all silica polymorphs studied in this work. Its silicon polyhedra are arranged in edge-sharing six-coordinated octahedra, as shown in Fig. 3.12. The

reconstructed six-folded octahedra blocks result in a much smaller inter-atomic distance in comparison to other tetrahedra based silica systems. The transition from coesite to post-stishovite involves large atomic displacements. It is interesting to note that the post-stishovite phase can be pressure-quenched to ambient conditions. Both experiment and simulations support that such a phase transition is not reversible, suggesting a reconstructive type from the observation of structural changes[19].

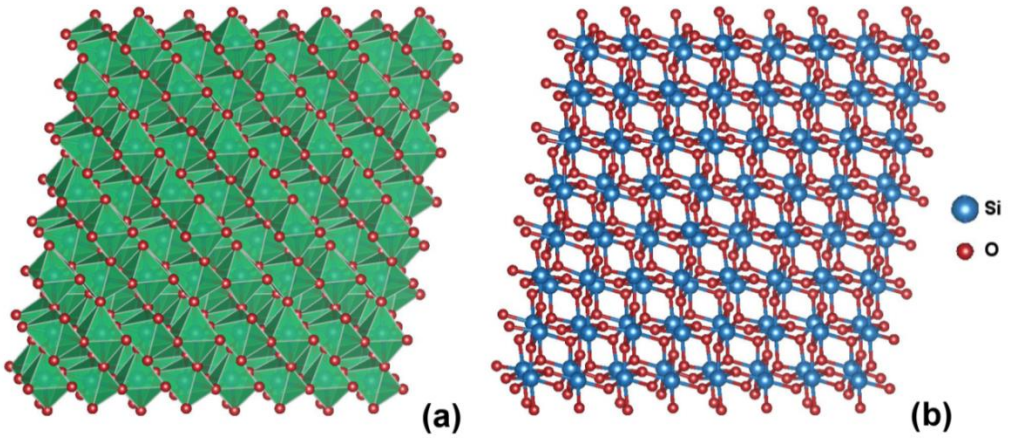

Figure 3.12. Structural representation with polyhedra of post-stishovite at 40 GPa. The silica supercell is projected along the *c*-axis of the simulation box. Structure with polyhedral is shown in the left figure and the ball-stick framework is shown on the right of the figure. Edge-sharing octahedra are colored in blue.

While the static properties of compressed coesite are illustrated by the EOS curves, the details of the phase transition at room temperature are directly monitored by the *ab-initio* molecular dynamics simulation, which will be discussed in the next section.

3.3 *Ab initio* molecular dynamics

3.3.1 First-principles MD in CPMD

In order to elucidate the role of high pressure on the structural changes of coesite, first-principles MD has been conducted. First-principles MD simulation was performed with the Car-Parrinello MD (CPMD) package[20]. One coesite unitcell (48 atoms, space group C2/c) was slowly compressed to 40 GPa, and equilibrated for 2 picoseconds at 300 K with *ab initio* MD in an NPT ensemble. During *ab initio* MD simulation, the fluctuations of fictitious electron kinetic energy were restricted by the velocities scaling method in a range of ±300 K and the nuclear degree of freedom was controlled by the Nosé-Hoover chain thermostats[21].

Although the cell edges and cohesive energies were directly monitored in the simulation, the pressure and enthalpy were not. The stress tensor matrix of the system was recorded every 100 MD steps and the Cauchy stress tensor σ can be defined as:

$$\sigma = \begin{bmatrix} \sigma_{11} & \sigma_{12} & \sigma_{13} \\ \sigma_{21} & \sigma_{22} & \sigma_{23} \\ \sigma_{31} & \sigma_{32} & \sigma_{33} \end{bmatrix} \tag{3.1}$$

The instantaneous pressure was then calculated from the determinate of the stress tensor matrix.

$$p = \sqrt[3]{det(\sigma)} \tag{3.2}$$

The stress tensor is very sensitive to the change of lattice parameters. Small thermodynamical fluctuations lead to tremendous jumps in instantaneous pressures and such values cannot represent the observable pressure of the system. Therefore the calculated pressure should be an averaged value over the simulation period. In this spirit, the pressure is averaged over the simulation time and we checked the convergence by

comparing with the designated pressure value. Based on the convergence of force, a plane wave energy cutoff of 150 Ry has been used in all of the MD simulations, sufficient to converge pressure (see, *e.g.* Fig. 3.13, where pressure converges at 40 GPa after 50,000 timesteps.).

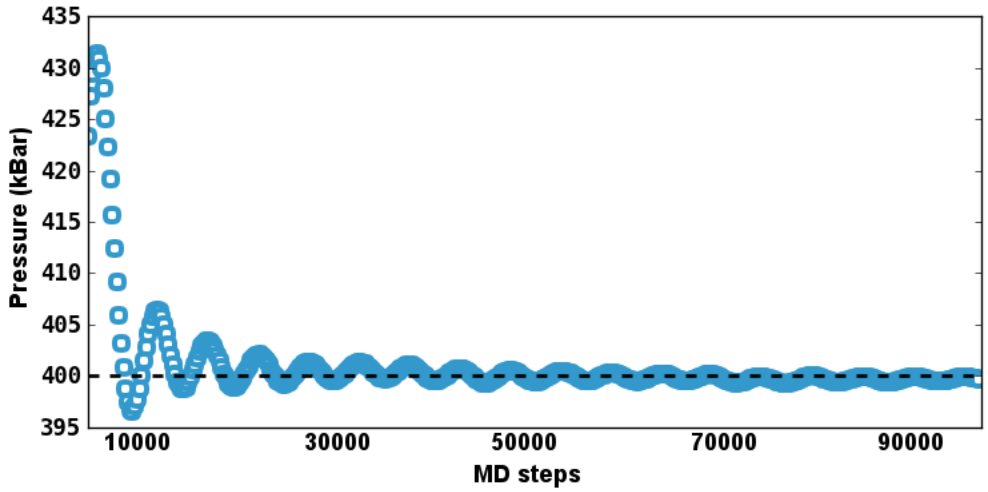

Figure 3.13. Pressure convergence of *ab initio* simulation pressure at 40 GPa. The pressure was calculated from the determinant of the Cauchy stress matrix and averaged over simulation time. It converged to 40 GPa within a few tens of thousands of MD steps.

The enthalpy of the system, consisting of the cohesive energy U and the pressure-volume term PV, was then calculated from its definition:

$$H(P,V) = U + PV \tag{3.3}$$

3.3.2 Configuring metadynamics in CPMD

In order to handle barrier-crossing processes, the metadynamics algorithm[22] is employed. The basis of this method has been discussed in chapter 2.5.1. For

metadynamics simulation, various combinations of collective variables (CVs) have been carefully tested. For the coesite system, the most efficient CVs were found to be the cell-edges (lengths) of *b* and *c* axis combined with the average coordination number of silicon atoms, which is defined by the following equation:

$$CN = \frac{1}{N_{Si}} \sum_i \sum_j \frac{1 - (d_{ij}/d_0)^6}{1 - \left(\frac{d_{ij}}{d_0}\right)^{12}} \tag{3.4}$$

where d_{ij} refers to Si-O bond distance; d_0 is a reference bond length (2.1 Å); *i* and *j* loop over silicon and oxygen atoms respectively. Consequently, the bias energy $V(\boldsymbol{s}, t)$ along the metadynamics simulation is given by:

$$V(\boldsymbol{s}, t) = \sum_{t_i<t} h \exp\left[-\frac{(\boldsymbol{s}_i - \boldsymbol{s})^2}{2\delta_{\boldsymbol{s}}{}^2}\right] \tag{3.5}$$

where *t* denotes simulation time, and s_i is the value of the *i*th CV. The height *h* and width $\delta_{\boldsymbol{s}}$ of the Gaussian hill shape were carefully selected to facilitate the metadynamics simulation. The fluctuations of all the CVs were first monitored without modifying the free-energy landscape. These trail runs enabled us to determine the energy scaling factors to synchronize all CVs, satisfying the relationship:

$$\alpha_1\omega_1 = \alpha_2\omega_2 = \alpha_3\omega_3 \tag{3.6}$$

where ω_i is the fluctuation range for the *i*th CV. The Gaussian width δ_s was set to be ¼ of the fluctuation of a CV type and applied to all CVs by multiplying their scaling factors. The height of the Gaussian type bias energy was chosen within 0.5~2.0 k_bT, depending on the phase regions of the simulation samples (A shallower height, *e.g.*, 0.5 k_bT, was

applied near the saddle point of the phase transition). Such potential heights were proved efficient in filling most energy wells as shown in similar works[23,24].

After a bias energy was deposited at each metastep, the system was equilibrated with lengthy *ab initio* MD simulations. The number of MD steps was determined in such a way that the CV displacement is comparable with the width of the bias energy, avoiding the so-called "hill surfing problems"[25]. Therefore the metadynamics timestep was chosen adaptively such that a Gaussian was placed at t_i once the following condition was fulfilled:

$$|s(t) - s(t_i)| = \frac{3}{2}\delta_s \tag{3.7}$$

As soon as a phase transition was identified, the energy deposition parameters were updated. The table below briefly summarizes the parameters used in sampling SiO_2 polymorphs at 40 GPa and 300 K.

Table 3.6. Scaling factors and gaussian shape parameters for different silica phases used in metadynamics simulation of coesite.

	α_1(b)	α_2(c)	α_3(coordination)	δ_s(a.u.)	h(k_bT)
Coesite	2.5	2.5	1.0	0.08	2.0
M1 & M2	1.0	1.5	1.0	0.06	0.5
M3 & M4	2.0	2.0	1.0	0.08	1.0

3.3.3 First-principles MD up to 40 GPa: distorted coesite

During the compression of coesite to 40 GPa, the monoclinic structure is found to be slightly distorted but all Si atoms remain to be tetrahedral coordinated by oxygen, corroborating the previously reported compression mechanism of coesite at low pressures[17,18] (see Fig. 3.14)

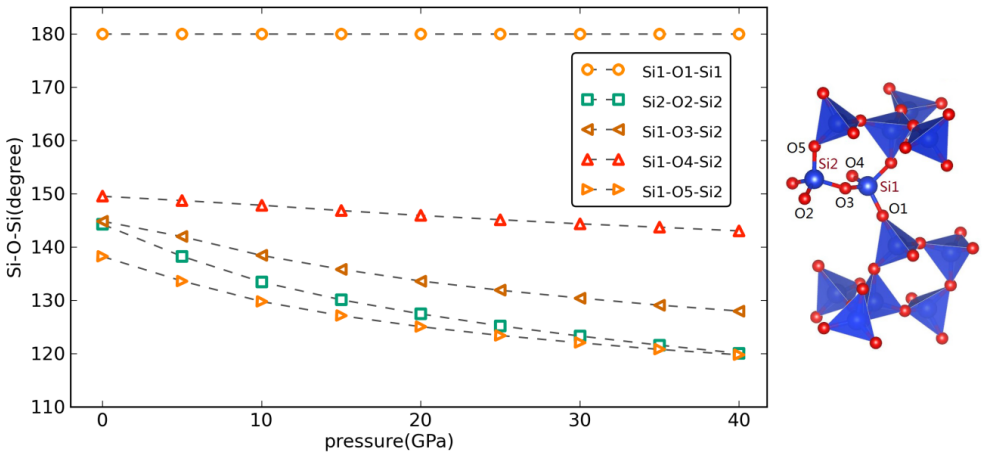

Figure 3.14. The evolution of Si-O bond angle in a compressed coesite unit cell. The bond angle relationship is shown on the right panel. Si and O atoms are represented by blue and red balls respectively. The Si-O tetrahedra are colored in blue.

Geometric relaxation up to 40 GPa has been carried out and closely monitored the change of five typical bond angles in coesite. The Si1-O1-Si1 bond-angles keep as 180 °, preserving the central symmetry in the C2/c space group. The decrease of all other bond angles represents the rotation of Si-O polyhedra as an effort to compensate the volume reduction during compression. Such observations match prior literature results on single

crystal coesite[17,18].

At 40 GPa, the distorted triclinic coesite structure survive long time *ab initio* MD simulation (up to 4.8 picoseconds), indicating that an energy barrier prevents further structural changes and also suggesting the *ab initio* MD method is ineffective to overcome the energy barrier.

3.3.4 Free energy landscape

To circumvent this issue, the metadynamics method[22] was introduced to accelerate sampling of the potential energy surface and explore possible transition pathways of coesite.

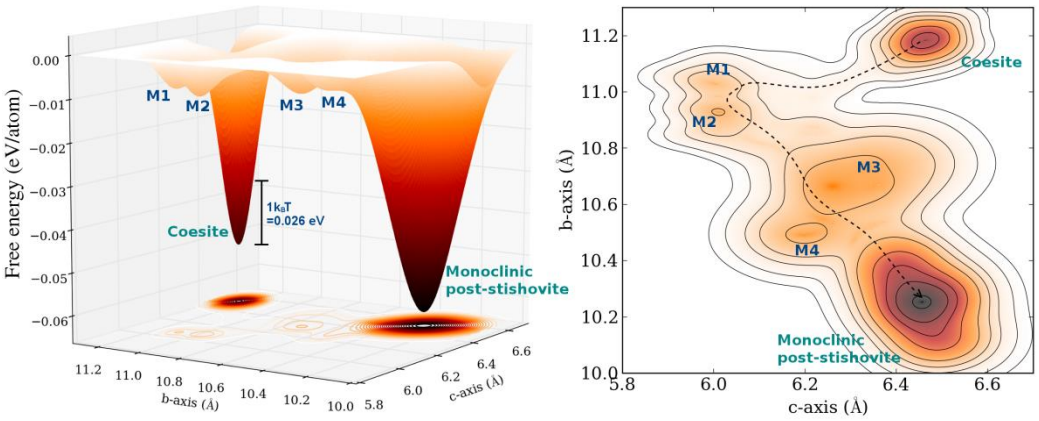

Figure 3.15. Free energy landscape showing the transition pathways from coesite to post-stishovite obtained by *ab initio* metadynamics simulation at 40 GPa and 300 K. A hypothetical transition pathway is shown in the left panel (dotted line). Several local energy minima (M1-M4) are present between the stable coesite and post-stishovite phases. The stability of the various structural intermediates has been confirmed with phonon calculations, where no imaginary vibration modes are identified.

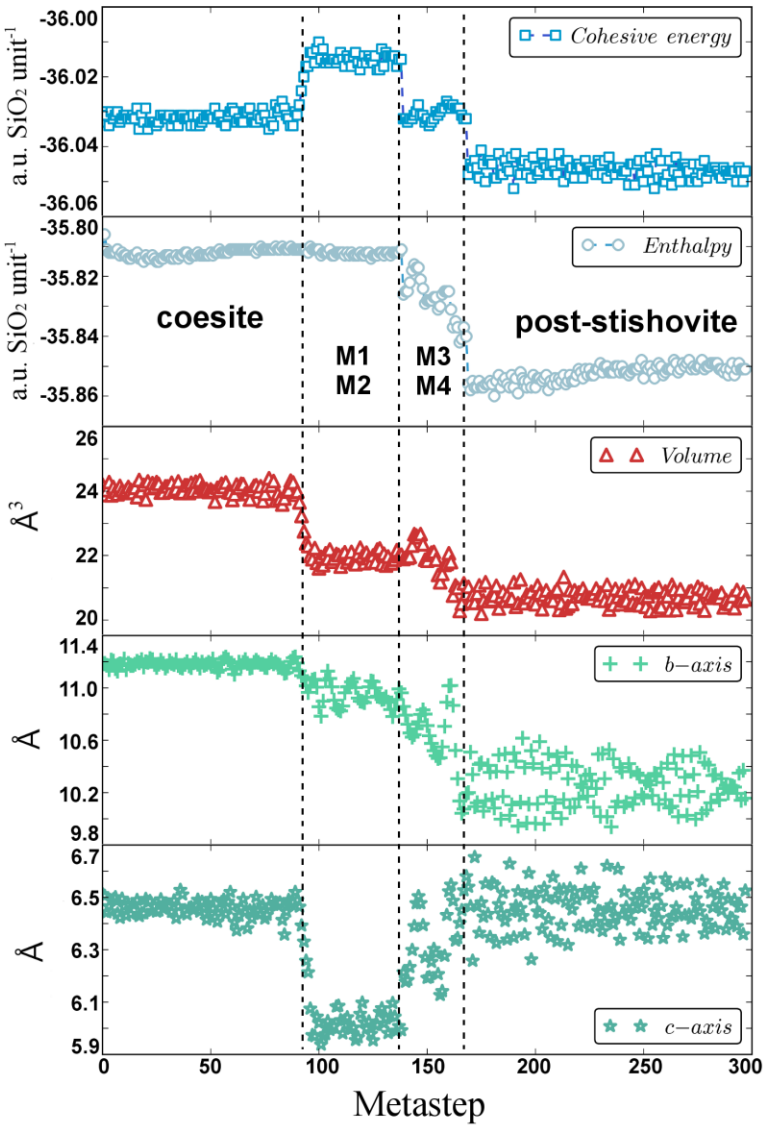

Figure 3.16. Summary of *ab initio* metadynamics simulation. The evolution of enthalpy, potential energy, volume and lattice parameters of SiO_2 (starting from coesite) along the *ab initio* metadynamics simulation sampling the potential energy surface. The simulation was carried out at 300 K and 40 GPa, using Si coordination number (see the text) as the collective variable. The metastable phases emerging from metadynamics (M1-M4) are found to have similar volumes but different short-range order structures.

Following the prescribed simulation protocol, within a few hundreds of metasteps, the system undergoes a direct transition from coesite to a monoclinic post-stishovite structure, and four distinct metastable structures are captured along the transition path, exactly matching the experimental observations. The free-energy landscape is shown in Fig. 3.15, where the derived free energy landscape is projected along cell edge b (s_1) and c (s_2). At each metastep, a two-dimensional Gaussian type energy is added to the energy landscape. The energy intensity z as a function of s_1 and s_2 is calculated by:

$$z(s_1, s_2) = \sum_{t_i<t} h \exp\left(-\frac{(s_{1i} - s_1)^2}{2(\alpha_1 \delta_s)^2} - \frac{(s_{2i} - s_2)^2}{2(\alpha_2 \delta_s)^2}\right) \tag{3.8}$$

The free energy landscape is reproduced by summating all gaussian type energies throughout the simulation time. Four metastable phases (labeled as M1 to M4) labeled at the energy dips are observed, as they are frequently visited structures in the metadynamics simulation. Those structures can survive after running a short MD simulation (2 nanoseconds). By tracking the evolution of the cell edges, a hypothetical transition pathway can be sketched out, connecting the four metastable phases between the coesite and post-stishovite silica phases (Fig 3.15, right figure). Details about the energetics, lattice parameters and coordination changes during the metadynamics simulation will be illustrated in Fig. 3.16 and 3.17 respectively.

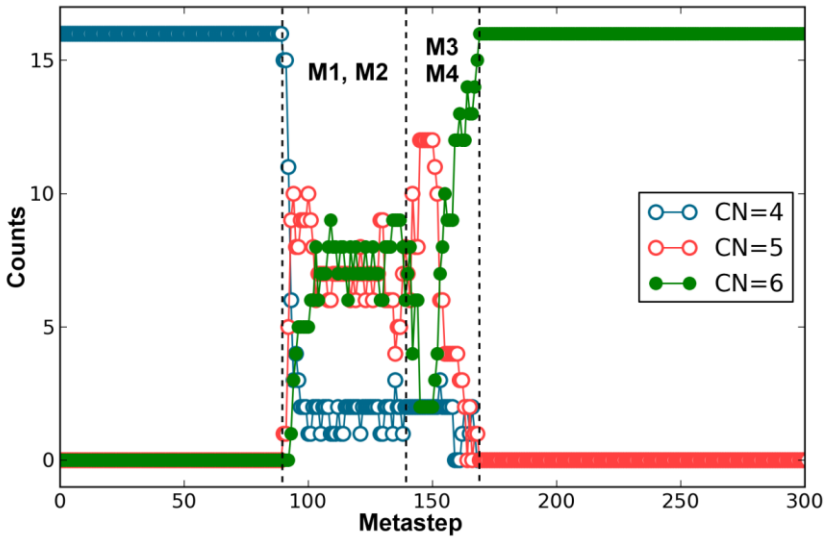

Figures 3.17. The evolution of the coordination number of Si atoms along the *ab initio* metadynamics simulation (see Fig. 3.16). The bonding length threshold between Si and O was set to be 2.1 Å for coordination number calculations. With increasing metadynamics steps, the coordination number of Si changes from four to six, indicating that the compressed metastable phases have mixed structural motifs with different coordination numbers along the transition pathways.

3.3.5 The transition sequence

The initial silicon tetrahedral structure distorts and the connections between neighboring silicon atoms are broken after the first 81 metasteps. The system then become trapped between two competing metastable structures (*e.g.*, see Fig. 3.14), signified by the development of two six-coordinated silicon polyhedra connected perpendicularly to the (110) plane, as shown in Fig. 3.18 b&c.

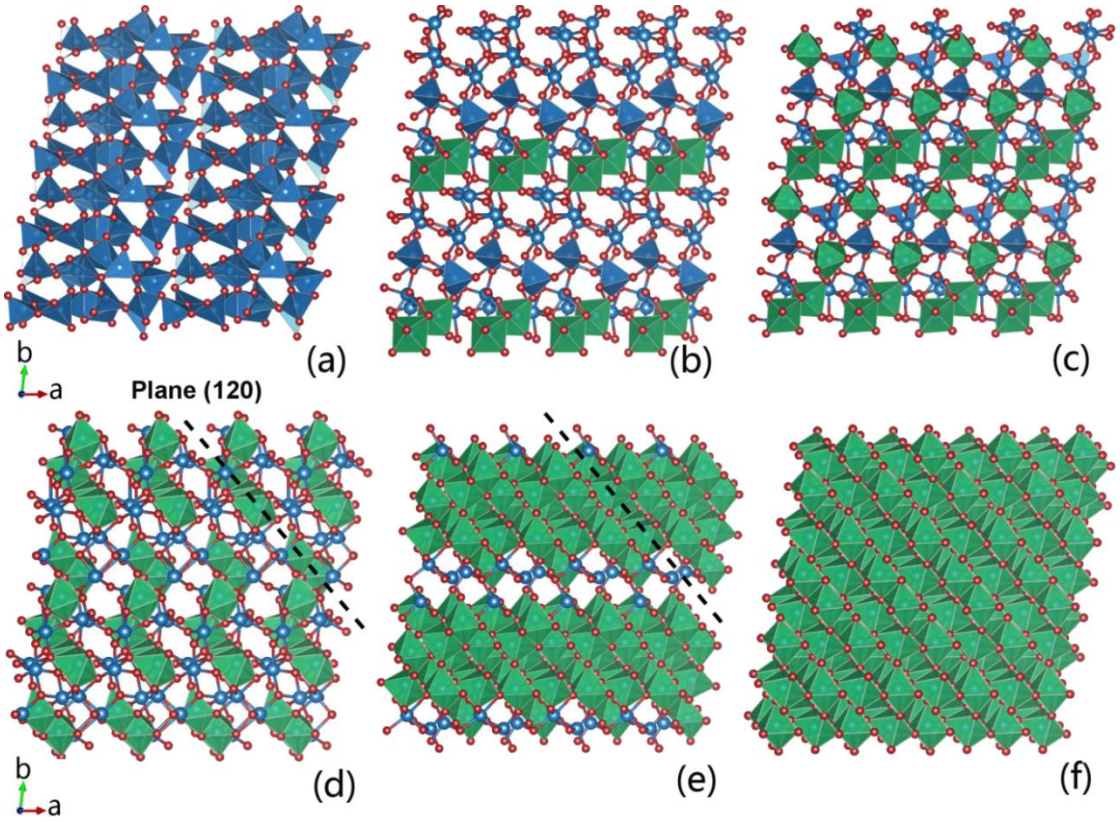

Figure 3.18. Illustration of the structural transition from coesite (C2/c) to monoclinic post-stishovite (P2/c) derived from *ab initio* metadynamics simulation. Structural evolution from (a) coesite to (f) monoclinic post-stishovite phase. (b)(c)(d)(e) correspond to the metastable phases (M1-M4) identified from metadynamics simulation, manifesting the SiO_6 octahedra units (colored in green) formed along the (120) plane (The SiO_4 tetrahedra units are colored in blue).

The appearance of the two metastable structures is associated with the unit cell to shorten by 7.7% along the *c*-axis. The new structural motifs with five and six-coordinated polyhedra stabilized the lattice and the free energy barrier between M1 and M2 is relatively small. Therefore local crossings between the two phases are possible at the simulation temperature. With prolonged metadynamics simulation, more six-coordinated

silicon atoms form along the (120) plane, resulting in an expansion of the *c*-axis and a compression of the *b*-axis (Fig 3.18 d&e). Correspondingly two more metastable structures with similar enthalpies are identified from the small dips M3 and M4 in Fig. 3.14, where silicon octahedra are observed to align alternately along the (120) plane. It finally transforms into the monoclinic post-stishovite phase after around 170 metasteps, accompanying a large drop in enthalpy. At this point, a total of 14.6% volume collapse is achieved by the phase transition from coesite to post-stishovite, resulting from the reconstruction of the edge-sharing six-coordinated octahedra structure (Fig. 3.18 f). An amount of kinetic energy, equivalent to 2.6 k_BT at 40 GPa and 300 K, is required to activate the transition from coesite to its first two metastable phases (M1 & M2).

The activation barrier to M3 & M4 is much smaller, estimated to be 0.7 k_BT from the height of the M2 phase. No further phase transitions are identified after a total of 300 metasteps, in agreement with the static calculation where the post-stishovite phase appears to be a stable phase above 40 GPa. The changes of Si coordination along the metadynamics simulation are shown in Fig. 3.17, illustrating the reconstructive nature of the phase transition. The newly discovered transition mechanism of compressed coesite is different from what has been reported by Martoňák *et al.*[26,27]

3.3.6 Phonon calculations

It is interesting to note that all the four metastable phases emerging from *ab initio* metadynamics (M1-M4) contain five-coordinated Si atoms, which have not been reported previously.

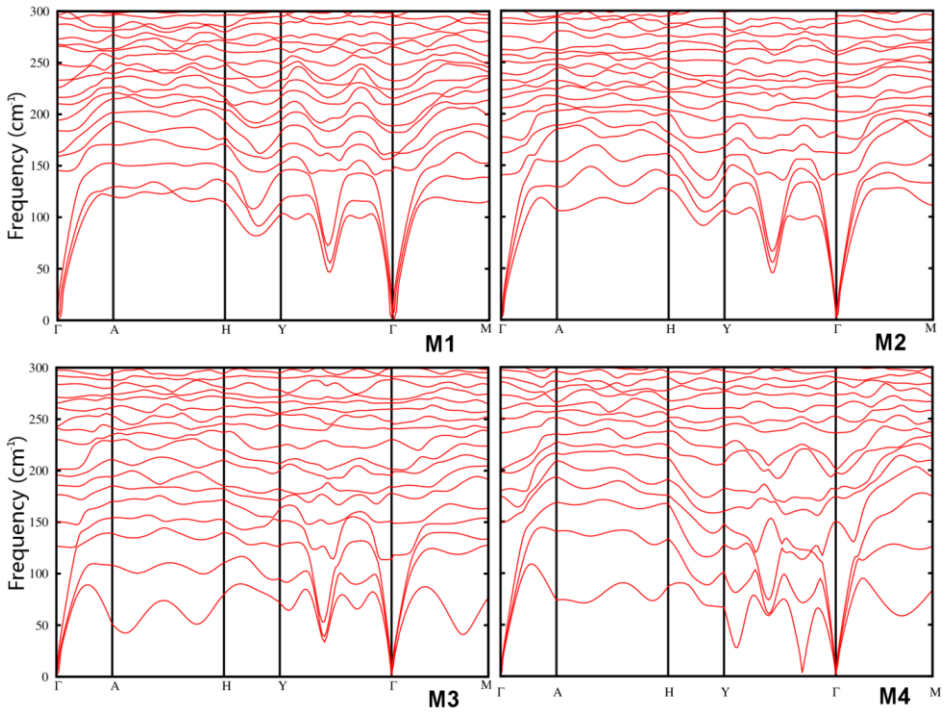

Figure 3.19. Phonon dispersion curves for four distinct metastable structures. The four metastable structures were identified from the metadynamics simulation. No negative modes are found at 26 GPa to show they are mechanical stable.

The mechanical stability of the metastable structures was investigated through *ab initio* MD simulation and it is found they are able to keep their coordinations up to 40 GPa at room temperature. The metastable structures were further quenched to 26 GPa and 0 K for phonon dispersion calculations (see Fig. 3.19). All structures were fully relaxed at 26 GPa and 0 K. Phonon calculation was implemented by the Quantum Espresso code with the same potential and kinetic cutoff used in CPMD. A 2×2×2 Monkhorst-Pack mesh was adopted to ensure the geometric optimized unit cell has an energy convergence of 1.0×10^{-7} eV, and the forces acting on each atom less than 0.01 eV/Å. The vibrational

frequencies were collected by finding the eigenvalues of the dynamical matrices on a grid of *q*-vectors same as the k-point mesh. Fourier interpolation was used to calculate the modes along the high symmetry points in the Brillouin zone.

No imagery vibration modes are found for those transition intermediates in the Brillouin zone; therefore they are confirmed to be metastable in the pressure range of interest. These metastable phases match the experiment results in the same pressure range (26 GPa~40 GPa), in which the four sets of diffraction patterns can be explained by the formation of the metastable structures in an on-going phase transition. The metastable structures from the experiment also show that the lattice parameter in the *b*-axis continues to decrease and the c-axis is greatly softened, which is exactly reproduced by the simulation. In the *ab initio* metadynamics simulation, the lattice parameters of the resulting monoclinic post-stishovite are comparable with the experimental data (Table 3.3).

3.4 Conclusion and discussion

In summary, using the integration of hydrostatic single-crystal x-ray diffraction, multiple crystal-solving techniques, and *ab initio* computer simulation, not only the long standing enigma of PIA of coesite is resolved, also we make several surprisingly important discoveries. Four new structures of SiO_2 that have not been reported or calculated previously were observed in this work. These intermediate phases can co-exist at the same time and have distinct coordination numbers. The long-sought for five-coordinated Si are also predicted to exist in all four new phases. Those five-coordinated silicon polyhedra exist to stabilize the compressed coesite phase between 26 to 45 GPa.

We conclude that the ostensible PIA might actually result from a mixture of low symmetry crystalline phases *en route* from Si tetrahedra to octahedra. Such a phase mixture, evidenced by diffraction-peak splitting, is only observable in single crystal experiments because single crystal diffraction patterns are extremely sensitive to minor lattice distortions. Moreover, our results demonstrate the power of this low-temperature (300 K) approach to freeze the intermediate phases and garner true understanding of the transition mechanism of refractory materials.

REFERENCE

1. Koch-Muller, M., Fei, Y., Hauri, E. & Liu, Z. Location and quantitative analysis of OH in coesite. *Phys. Chem. Minerals* **28**, 693-705 (2001).

2. Dera, P., *et al*. High pressure single-crystal micro X-ray diffraction analysis with GSE_ADA/RSV software. High Pressure Res. 33, 466-484 (2013)

3. Hemley, R. J., Jephcaot, A. P., Mao, H-K., Ming, L. C. & Manghnani, M. H. Pressure-induced amorphization of crystalline silica. *Nature* **334**, 52-54 (1988).

4. Kingma, K. J., Meade, C., Hemley, R. J., Mao, H-K. & Veblen, D. R. Microstructural observations of alpha-quartz amorphization. *Science* **259**, 666-669 (1993).

5. Miyahara, M., *et al*. Discovery of seifertite in a shocked lunar meteorite. *Nat. Commun.* **4**, 1737 (2013).

6. Goresy, A. E., Dubrovinsky, L., Sharp, T. G., Saxena, S. K. & Chen, M. A monoclinic post-stishovite polymorph of silica in the shergotty meteorite. *Science* **288**, 1632-1634 (2000).

7. Huang, L., Durandurdu., M & Keiffer. J. Transformation pathways of silica under high pressure. *Nat. Mater*. **5**, 977-981 (2006).

8. Tsuchida, Y. & Yagi, T. New pressure-induced transformations of silica at room temperature. *Nature* **347,** 267-269 (1990).

9. Teter, D. M. & Hemley, R. J. High pressure polymorphism in silica. *Phys. Rev. Lett.* **80**, 2145-2148 (1998).

10. Dmitriev, V. P., Toledano, P., Torgashev, V. I. & Salje E. K. H. Theory of reconstructive phase transitions between SiO_2 polymorphs. *Phys. Rev. B* **58**, 11911 (1998).

11. Stixrude, L. & Karki, B. Structure and freezing of $MgSiO_3$ liquid in earth's lower mantle. *Science* **310**, 297-299 (2005).

12. Giannozzi P., *et. al*. QUANTUM ESPRESSO: a modular and open-source software project for quantum simulations of materials. *J. Phys. Condens. Matter.* **21**, 395502 (2009).

13. Lee, C., Yang, W., & Parr, R. G. Development of the Colle-Salvetti correlation-energy formula into a functional of the electron density. *Phys. Rev. B,* **37**, 785. (1988).

14. Becke, A. D. Density-functional thermochemistry. III. The role of exact exchange. *J. Chem. Phys.* **98**, 5648 (1993).

15. Levien, L. & Prewitt, C. T. High-pressure crystal structure and compressibility of coesite. *Am. Miner.* **66**, 324-333 (1981).

16. Coes, L. A new dense crystalline silica. *Science* **118**, 131-132 (1953).

17. Angel, R. J., Mosenfelder, J. L. & Shaw, C. S. J. Anomalous compression and equation of state of coesite. *Phys. Earth Planet. In*. **124**, 71-79 (2001).

18. Angel, R. J., Shaw, C. S. J., Gibbs, G. V. Compression mechanisms of coesite. *Phys. Chem. Minerals.* **30**, 167-176 (2003).

19. Shekar N. V. C. & Rajan, K. G. Kinetic of pressure induced structural phase transitions – A reivew. *Bull. Mater. Sci.*, **24**, 1-21 (2001).

20. Andreoni, W. & Curioni, A. New advances in chemistry and materials science with CPMD and parallel computing. *Parallel Comput*. **26**, 819-842 (2000).

21. Martyna, G. K., Klein, M. L. & Tuckerman, M. Nosé-Hoover chains: the canonical ensemble via continuous dynamics. *J. Chem. Phys.* **97**, 2635-2643. (1992).

22. Laio, A & Gervasio, F. L. Metadynamics: a method to simulate rare events and reconstruct the free energy in biophysics, chemistry and material science. *Rep. Prog. Phys.* **71**, 126601 (2008).

23. Nair, N. N., Schreiner, E. & Marx, D. Glycine at the pyrite-water interface: the role of surface defects. *J. Am. Chem. Soc.* **128**, 13815-13826 (2006).

24. Schreiner, E., Nair, N. N. & Marx, D. Influence of extreme thermodynamics conditions and pyrite surfaces on peptide synthesis in aqueous media. *J. Am. Chem. Soc.* **130**, 2768-2770 (2008).

25. Ensing, B., Laio, A., Parrinello, M. & Klein, M. L. A recipe for the computation of the free energy barrier and the lowest free energy path of concerted reactions. *J. Phys. Chem. B.* **109**, 6676-6687 (2005).

26. Martoňák, R., Donadio, D., Oganov, A. R. & Parrinello, M. Crystal structure transformations in SiO_2 from classical & *ab initio* metadynamics. *Nat. Mater.* **5**, 623-626 (2006).

27. Martoňák, R., Donadio, D., Oganov, A. R. & Parrinello, M. From four- to six-coordinated silica: Transformation pathways Transformation pathways from metadynamics. *Phys. Rev. B* **76**, 014120 (2007)

IV. HIERARCHICAL SOLID-STATE TRANFORMATIONS OF α-QUARTZ UNDER HIGH PRESSURE

4.1 X-ray diffraction experiment

4.1.1 Experimental preparations

We performed compression experiments with single crystal α-quartz samples and used the XRD technique to identify the crystalline structures. The experiments were conducted at the 16 BMD station of High Pressure Collaborative Access Team (HPCAT) of the Advanced Phonon Source (APS), Argonne National Laboratory (ANL), Chicago. At the time of experiment, the X-ray beam had a wavelength of 0.4246 Å, equivalent to 29.2 keV in beam energy.

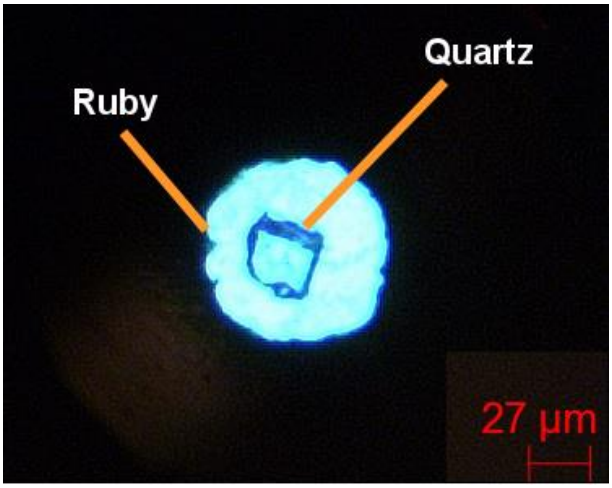

Figure 4.1. An optical microscopic image of α-quartz sample at 62 GPa.

The single crystal α-quartz sample was loaded into in a tungsten gasket with hole diameter 160 μm, seated on a 300 μm culet. One ruby ball was found at the edge of the hole (Fig. 4.1). The gasket hole was estimated to be around 80 μm at 62 GPa.

To ensure the best hydrostatic condition, helium gas was employed as the pressure medium. Up to the highest pressure we have achieved in the experiment, the single crystal quartz was still securely sealed in the DAC without any physical damages (see Fig. 4.1 for the microscopic image at 62 GPa). The pressure was calibrated by ruby fluorescence line shift in an off-line hutch. The uncertainty in the pressure was ±0.81 to 1.94 GPa, derived from the pressure change within each experiment interval.

4.1.2 α-quartz single crystal

The upper graph in Fig. 4.2 shows an indexed 2D diffraction pattern from the sample at 12 GPa. The diffraction image was processed in such a way that the strongest diffraction peaks from the single-crystal quartz sample were included but most saturated diamond peaks were masked out. Since strong diamond diffraction signals traveling through the seat can cause secondary powder diffraction (*i.e.*, Debye-Scherrer rings which are centered on the given diamond peaks[1]), the way the image is processed is for clarity purposes.

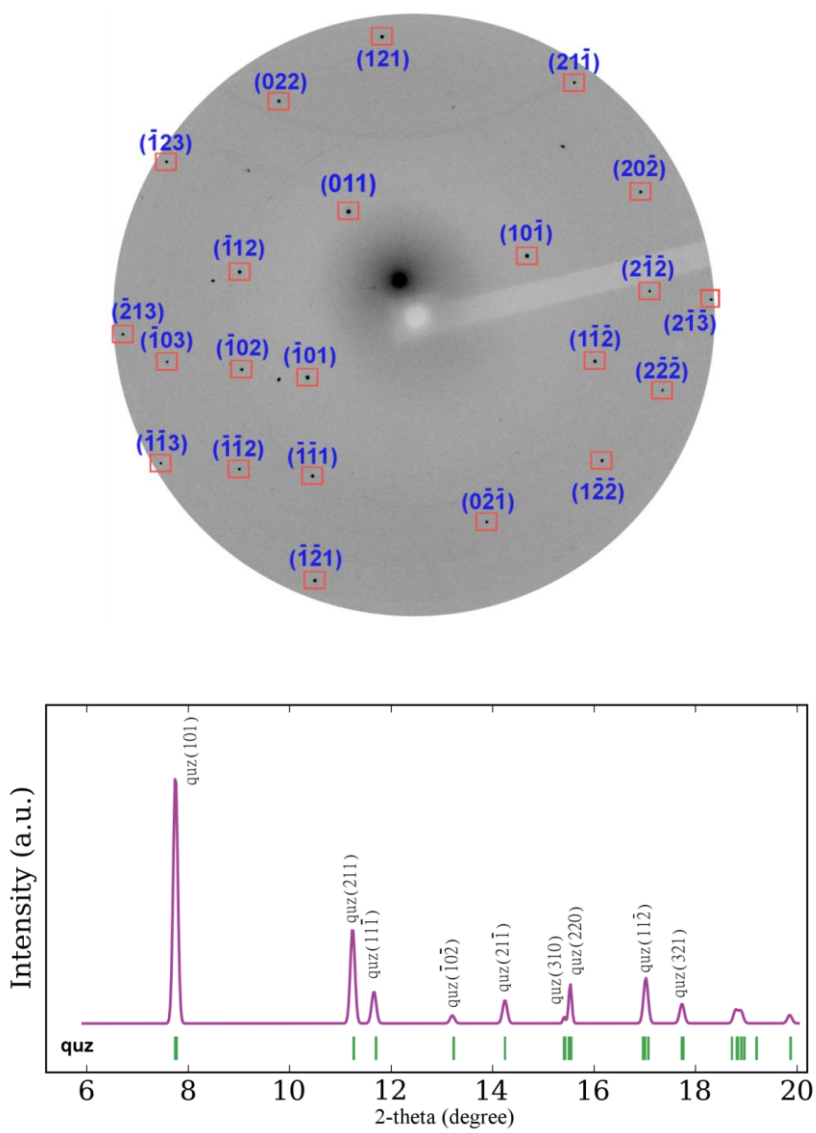

Figure 4.2. X-ray diffraction patterns of α-quartz at 12 GPa. The original 2D single crystal pattern is shown in the top panel. In the bottom integrated spectrum, all major peaks were refined to a trigonal α-quartz structure with space group $P3_121$, as indicated by the green bars.

4.1.3 Emergence of a quartz II phase

At 25 GPa (Fig. 4.3), although α-quartz peaks are still strong in intensity, a new set

of diffraction spots emerge, with a distinct crystalline orientation.

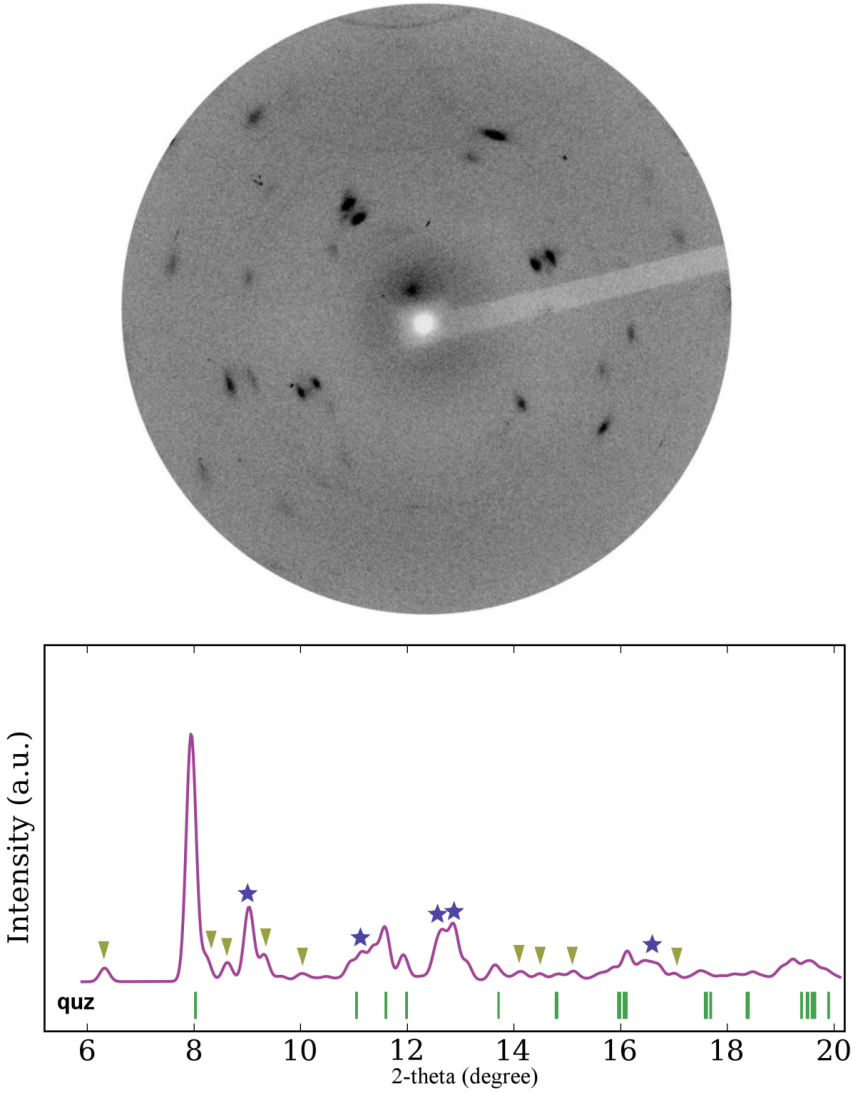

Figure 4.3. Single-crystal XRD images of compressed α-quartz at 25 GPa. The integrated diffraction spectrum, shown in the bottom graph, indicates a phase mixture. According to the high-pressure results, the sample contains compressed α-quartz (green bars), quartz II (space group P1, down golden triangles) and the monoclinic post-stishovite phase (space group P2/c, blue stars).

In order to solve the structure, the 2D pattern is integrated to a 1D diffraction spectrum. The appearance of the sharp (101) peak from α-quartz indicates the compressed sample still contains a considerable amount of low-quartz phase. However, with regard to the new diffraction peaks, we fail to associate them with any distorted α-quartz crystals. As we shall see later, the new peaks are possibly contributed from two new phases, the metastable quartz II phase (marked by golden down triangles) and the monoclinic post-stishovite phase (marked by blue stars). The rationale for the formation of the new phases is based on the simulation results at 36 GPa, which will be discussed the in the following section.

4.1.4 Coexistence of α-quartz, quartz II and post-stishovite phases

The diffraction pattern, drawn in the magenta curve (Fig. 4.4), reflects a three-phase mixture: the compressed α-quartz, the monoclinic type post-stishovite (P2/c space group) and the quartz II phase (P1 space group). The quartz II structure was originally discovered when compressing α-quartz to 22 GPa[2] and its diffraction peak positions are indicated by the green bars in Fig 4.4. The exact structure of quartz II is still under debate[3,4], which cannot be solved from the current experiment neither mainly because too few peaks are available for solving the crystalline structures. However, the calculated diffraction peaks from first-principles MD partially match the quartz II structure at the same pressure, which lends us support to analyze the structure of quartz II as shall be seen in the next section. The quartz II structure in the simulation is predicted to be a metastable phase intervening the transition pathway from α-quartz to post-stishovite.

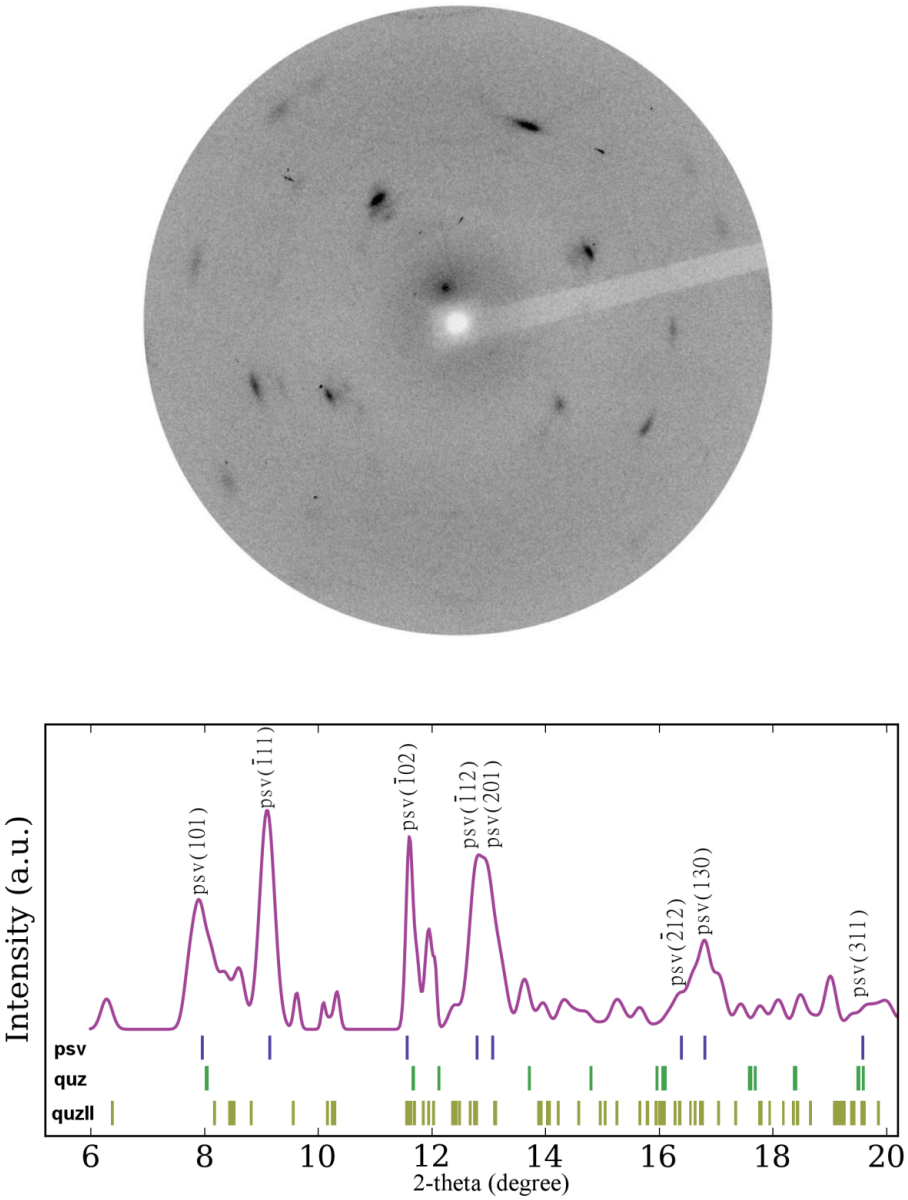

Figure 4.4. Single-crystal XRD image of compressed α-quartz at 36 GPa. The diffraction signal from α-quartz is rather poor at 36 GPa. The 2D pattern is integrated into a diffraction spectrum to resolve the high pressure phase of silica, as shown in the bottom figure.

Table 4.1. Crystallographic data for monoclinic post-stishovite. The experiment data was obtained at 300 K and 36.3 GPa. The simulation data was obtained from *ab initio* metadynamics followed by geometric relaxation (including cell parameters and atom positions) at 35 GPa and 0 K. The differences of the lattice parameters between experiment and simulation are less than ~4% in cell parameters. The atomic positions solved from simulation are shown on the right.

	Experiment	Simulation	Wyckoff positions from simulation			
Z	4	4	Space group		P2/c	
a (Å)	4.059(4)	3.956(5)		x	y	z
b (Å)	4.607(4)	4.883(3)	Si1	0.000	0.152	0.250
c (Å)	4.651(8)	4.397(3)	Si2	0.500	0.652	0.250
β	92.62(10)	90.95(2)	O1	0.265	0.383	0.419
ρ (g/cm^{-3})	4.59(3)	4.69(1)	O2	0.765	0.117	0.581

The eight blue bars (Fig. 4.4), used for indexing the monoclinic post-stishovite structure, were extracted from the single crystal X-ray diffraction pattern. Those peaks were used for refining the post-stishovite silica phase. The d-spacing values of the eight peaks from the 2D diffraction pattern ware found to match the simulation data, confirming that the pattern indeed corresponds to the monoclinic phase. Hence, the post-stishovite structure from simulation is used as the initial structural seed and employed a non-linear least-square fitting method (using the package *Unitcell*[5]) to refine the structure. The structure is managed to fit to a monoclinic post-stishovite silica structure (space group P2/c) that is slightly distorted from an orthorhombic structure with a larger beta angle. This newly found post-stishovite phase has the same structure as the high pressure monoclinic phase resulting from compressed coesite. The fit lattice parameters, compared to the simulation, are showed in Table 4.1.

4.1.5 The high pressure post-stishovite phase

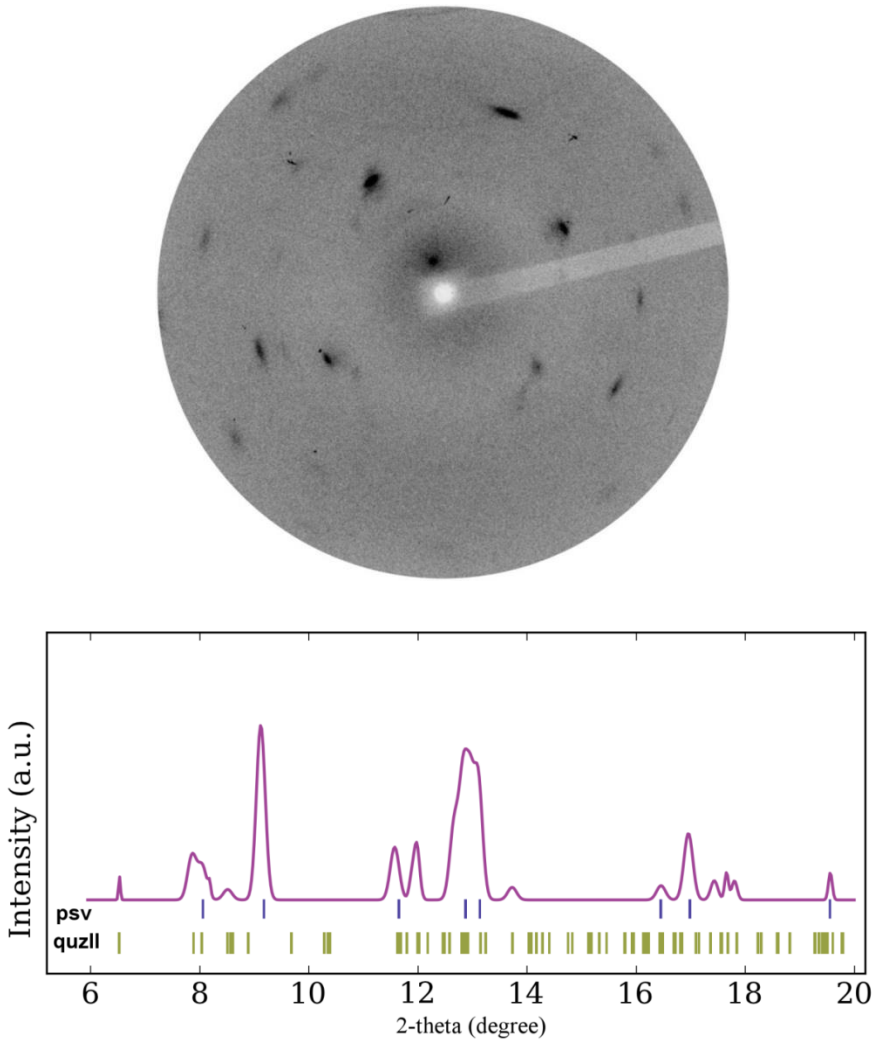

Figure 4.5. A single-crystal 2D XRD image (upper panel) and its integrated X-ray spectrum (bottom panel) of compressed sample at 45 GPa. Blue bars were the single crystal peaks used for fitting the monoclinic post-stishovite structure. Other peaks that are not indexed for post-stishovite are from quartz II residuals. Owning to the poor intensity of diffraction signals at 45 GPa, those peaks that are hardly distinguishable from the detector background were excluded from the spectrum. The peaks labeled in the spectrum have relatively higher intensities.

Upon the completion of phase transition (Fig. 4.5), some low intensity peaks from post-stishovite are strengthened.

We provide the diffraction pattern at 45 GPa, where some peaks can still be identified from the residual quartz II phase. The remaining eight strong peaks are used to obtain the lattice parameter at 45 and 55 GPa. The refined crystal structure generates a list of diffraction peaks belonging to the post-stishovite phase and is used to locate more post-stishovite peaks at those pressures. Using such a double-index approach, more diffraction peaks from the post-stishovite phase are confirmed. The diffraction peaks in Fig. 4.6 are purely from the monoclinic type post-stishovite.

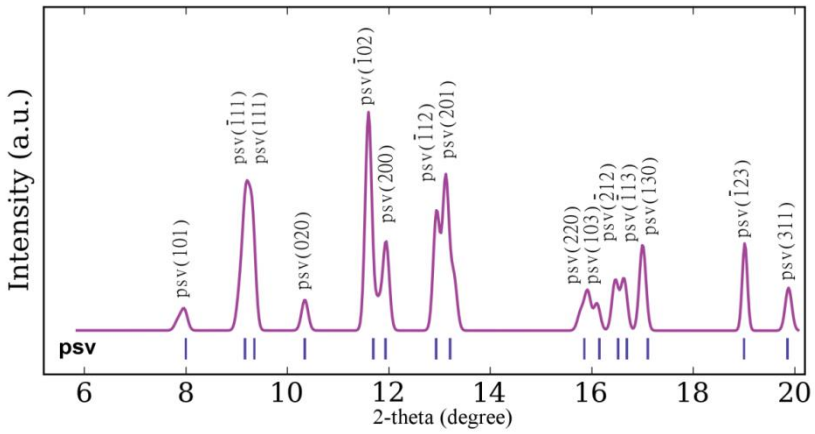

Figure 4.6. X-ray diffraction spectrum of the compressed quartz sample at 55 GPa. The pattern is indexed to a monoclinic post-stishovite silica structure. Some low intensity peaks that cannot be recognized in the wide scan diffraction image are confirmed in the step scan images.

The crystallinity of the new high pressure phase in compressed α-quartz is not

perfect at room temperature. In Fig 4.7 the evolution of one diffraction spot (the (011) peak in α-quartz) is shown, where its intensity is greatly lowered during compression.

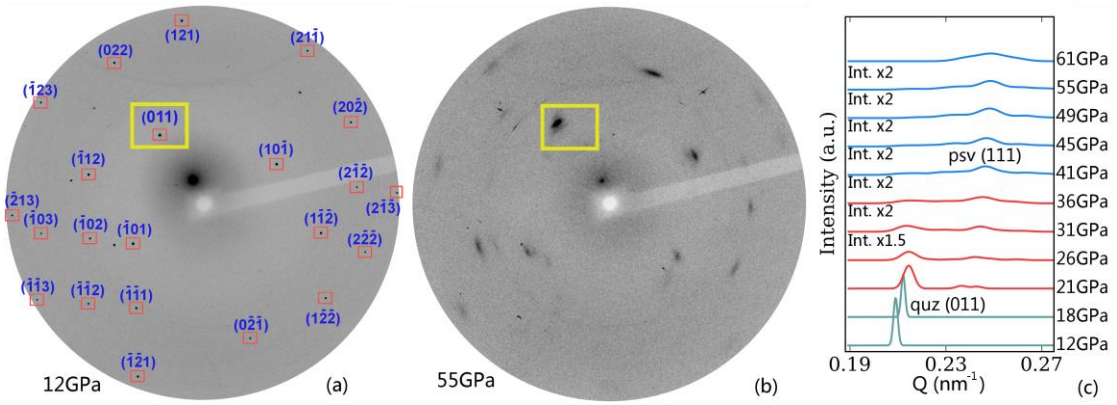

Figure 4.7. XRD patterns for pressurizing an α-quartz single crystal at (a) 12GPa, α-quartz single crystal. (b) 55GPa, crystallized monoclinic type post-stishovite. (c) The evolution of the integrated diffraction spectrum within the solid box shown in Fig. (a) and (b). The (111) peak is almost 10 times lowered in intensity at 41 GPa. The spread along the d-spacing is very obvious at higher pressures, resembling the amorphization phenomenon if powder samples were used.

The full width at the half maximum at 45 GPa is around 10 times greater than at 12 GPa. Such peak weakening resembles what is observed in compressing powder α-quartz, where the diffraction peaks from the sample gradually disappeared above 25 GPa. The weak diffraction peaks from the high pressure phase, however are able to be detected using the single crystal technique thanks to a better intensity contrast between sample diffraction and the background.

4.1.6 A summary on the evolution of the diffraction spectrum of quartz

In summary, from the energy dispersive X-ray diffraction experiment on single crystal samples, the α-quartz phase transforms to an intermediate quartz II phase, *en route* to the monoclinic type post-stishovite phase. The evolution of the XRD spectrum is shown in Fig. 4.7.

The intermediate phase, coexisting with the high-pressure post-stishovite phase at 25-45 GPa, gradually loses all its diffraction signals during compression above 25 GPa. At the same time, the diffraction peaks from the post-stishovite phase sustain and are strengthened. The coordination of silicon in low pressure phase (four-coordinated silicon) increases to six, requiring re-bonding and lots of atomic displacements to accomplish. Thermodynamically, the recoordination needs a huge amount of kinetic energy to ensure a transformation into a less defected crystal, similar to the work done with the laser heating technique or the multi-anvil[6] approach. However, by compressing the sample at room temperature, the intermediate phase can be clearly identified. The mechanism of this phase transition will be discussed in the energetic analysis in the next section.

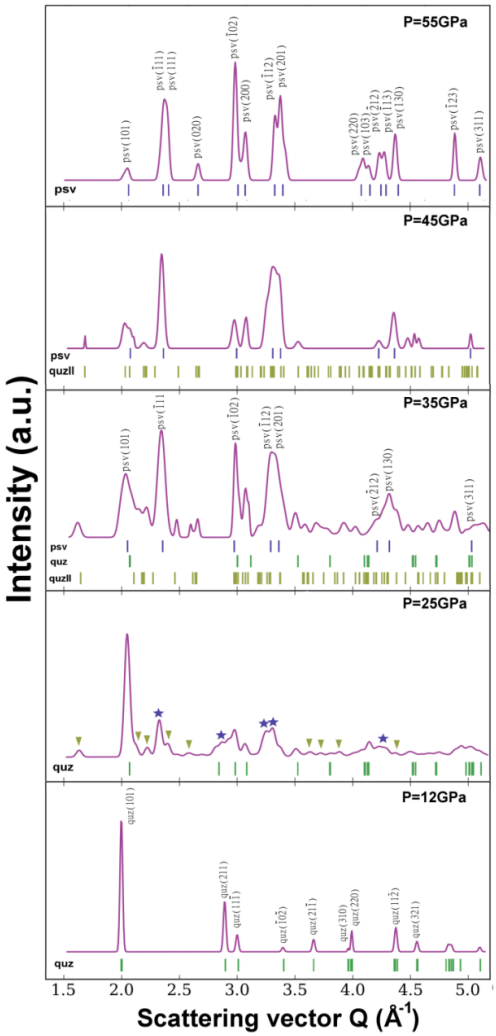

Figure 4.8. Evolution of the X-ray diffraction pattern of compressed single-crystal α-quartz. Starting from the α-quartz phase (12 GPa, green bars, space group $P3_121$), it slowly transformed into the quartz II phase (25 GPa, space group C2) and the monoclinic type post-stishovite phase (space group P2/c). Symbols indicate the new emerging peaks are either attributed from quartz II (yellow down triangles) or post-stishovite (blue stars). Quartz II appears to be the intermediate phase (yellow bars) and it coexists with the post-stishovite phase (blue bars) from 25 to 45 GPa. It completely crystalized into the more compressed post-stishovite phase at 55 GPa, where quartz II peaks are too weak to be observed. The intensities of all spectrums were scaled to fit the box size. The abbreviations in the figure are: quz, quartz; quzII, quartz II; psv, post-stishovite.

4.2 Structural optimization and lattice dynamics

4.2.1 First-principles structural optimization

The first-principles structure optimizations were performed in the framework of density functional theory (DFT) through package Quantum ESPRESSO ver. 5.0.1[7]. The generalized gradient approximation under the Becke-Lee-Yang-Parr parametrization was implemented to describe the exchange corelation functional[8,9]. The norm-conserving pseudopotentials were used with 4 valence electrons for Si ($2s^2 2p^2$) and 6 for O atoms ($2s^2 2p^4$). A plane-wave basis set with kinetic energy cut off of 200 Ry (2721 eV) was found sufficient to converge the total energy less than 2.7×10^{-7} eV. All structures were fully relaxed (relax cell variable and atomic postions) so that the forces acting on each atom are less than 0.01 eV/Å. The unit cells of four silica polymorphs were used for the equations of state calculation, in which their Brillouin zones were sampled by a Monkhorst mesh of *k* points. The simulation variables for each silica polymorph are summarized in the Table 4.2:

Table 4.2. Lattice types and *k-points* meshes for different silica polymorphs.

	Z	Space group	*k-points* mesh	# irreducible *k-points*
α-quartz	3	$P3_121$	$3 \times 3 \times 3$	7
quartz II	12	P1	$3 \times 3 \times 3$	14
quartz III	3	C222	$3 \times 3 \times 3$	14
stishovite	2	$P4_2/mnm$	$5 \times 5 \times 5$	18
$CaCl_2$ silica	2	Pnnm	$4 \times 4 \times 4$	30
α-PbO_2 silica	4	Pbcn	$3 \times 3 \times 3$	10
post-stishovite	4	P2/c	$3 \times 3 \times 3$	14

Hydrostatic pressure was applied by adding the pulay stress to the diagonal elements of the stress tensor. At each pressure, the system was optimized for atomic position, cell shape and cell volume.

4.2.2 A comparison of simulation models

Besides the BLYP type GGA potential in Quantum ESPRESSO, LDA and GGA[10,11] based simulations were also carried with the package of Vienna *Ab Initio* Simulation Package (VASP)[12] to compare with the simulation models used in this thesis. Our results were also compared with the high-accuracy (but computationally demanding) hybrid HSE functional calcuations[13]. The calculated equations of state are compared with many experimental and computational data available in the literature[3,14,15] on low quartz, shown in Fig. 4.8.

According to the simulation results, all the three types of exchange-correlation funcitonals used in this work (GGA and LDA with VASP, and BLYP type GGA potential with Quantum ESPRESSO) reproduce the same geometrically relaxed crystal structures. However, below 10 GPa, the volume obtained from the GGA/VASP method is overestimated by ~10%. The systematic deviation in GGA/VASP does not reflect a different description of atomic arrangements, but merely a superposed isotropic pressure arising from the gradient corrections. It motivates us to adopt a better GGA functional for the system. For the LDA treatment, although it produces more accurate compression curves, it fails to give a reasonably accurate prediction of the quartz to stishovite transition pressure[16-18]. According to the literature[18], the energy difference of the α-quartz and stishovite per SiO_2 unit is correctly predicted to be 0.57 eV (compared to an

experimental value of 0.54 eV[16,17]) with the gradient correction, while in LDA the energy difference is significantly underestimated.

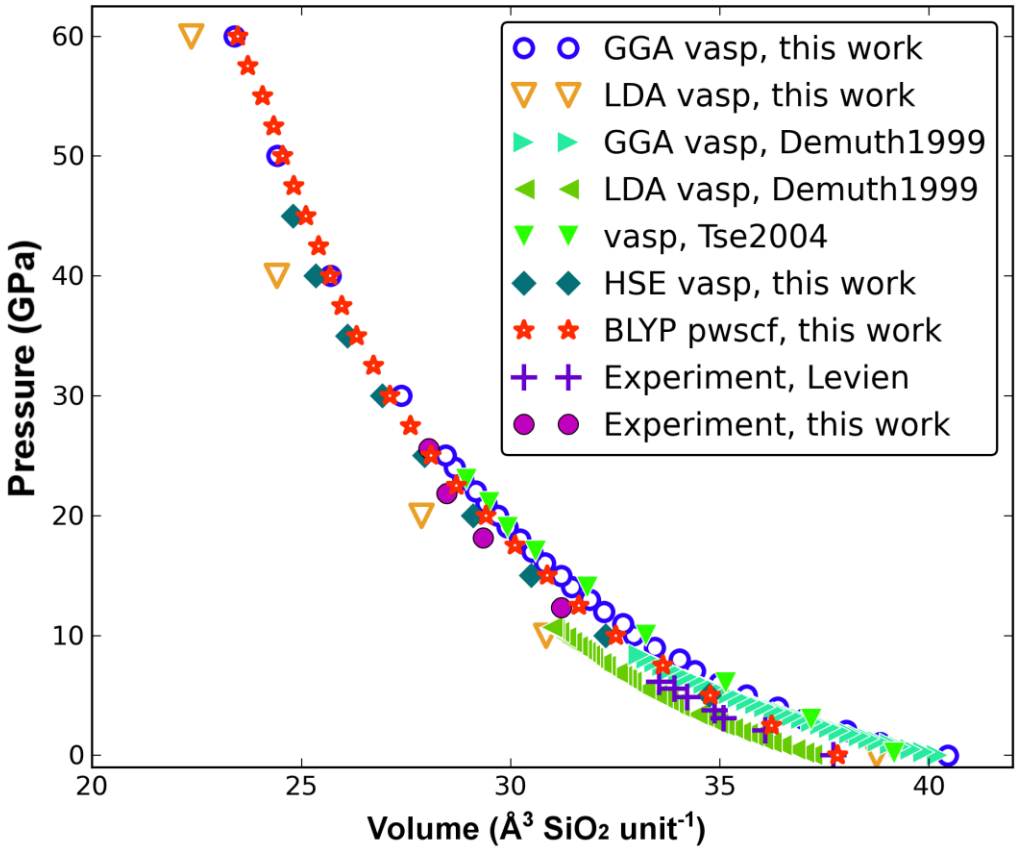

Figure 4.8. Equations of state of α-quartz from *ab initio* calculations and experiments. The data labeled in blue open circles employed the PAW pseudopotential with GGA parameterization and a 550 eV kinetic energy cutoff implemented in VASP. The yellow inversed triangles were taken from the LDA modeling of exchange correlation energy in VASP with the same cutoff as GGA. The red star markers were calculated from the BLYP type exchange-correlation functional in Quantum ESPRESSO. The brunswick green diamonds were calculated from the hybrid HSE functional implemented in VASP. The equations of state were compared with reference data[3,14] and experiments[15]. Based on the results, the BLYP parameterization is chosen for this work.

Finally, the BLYP parameterization with the gradient correction has both accurate lattice parameters prediction and reasonable energy difference between quartz and stishovite. The tests indicate that the BLYP type exchange-correlation functional is among the best to model α-quartz, with an accuracy of within 1% volume difference in comparison with the experiments, which also compares favorably with the high-accuracy hybrid HSE functional. Therefore the GGA pseudopotential with the BLYP-type exchange-correlation parameters is mainly used in this work. At high pressures (>20 GPa), the Perdew-Wang type GGA implemented in VASP is found to be on a par with the BLYP functional, which is used in the NEB calculations with VASP.

4.2.3 Equations of state of compressed α-quartz

The equations of state from first-principles simulations generally match well with the experimental data (Fig. 4.10). The experimentally refined cell volumes of α-quartz (green solid squares with error bars) are consistent with the volume changes from the simulation.

The quartz II and quartz III structures are both layered edge-sharing octahedral structures, linked by silicon tetrahedra. Both structures have octahedra versus tetrahedra number ratio of 2:1, showing the collapse of volume upon pressurization. The most compressed phase in this work, the post-stishovite phase, is around 18.7% denser than the α-quartz phase and 10.7% more compressed than the quartz II phase (compared at 30 GPa and 300 K). The post-stishovite phase appears at 25 GPa and can be fully identified above 35 GPa as a six-coordinated structure, which is considered as the stable Si-O polyhedral unit in Earth mantle-core pressure region. The large volume collapse from the

four-coordinated to six-coordinated system strongly influences the occurrence of earthquakes and plate movements.

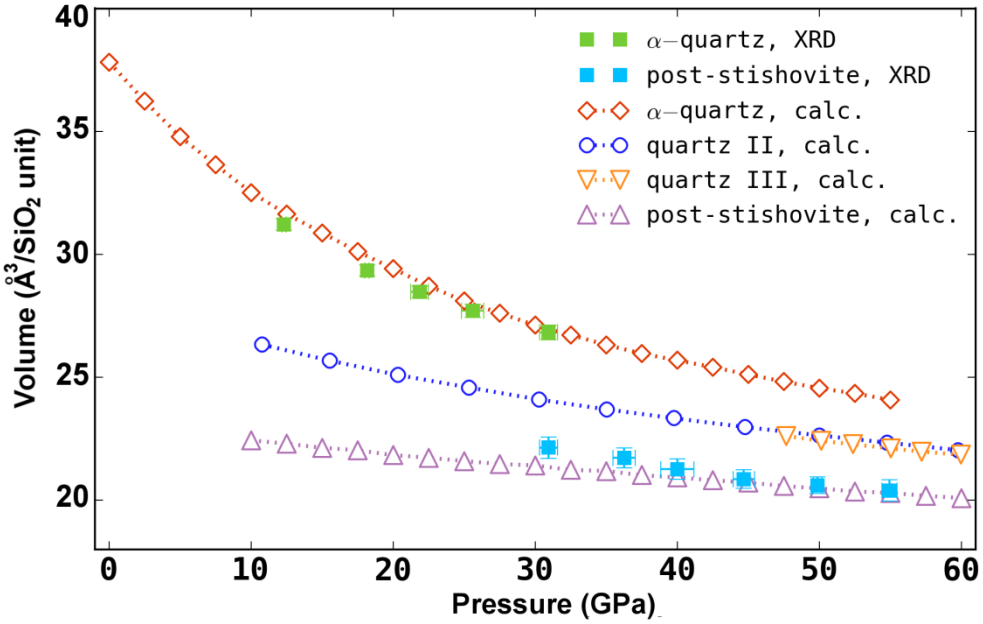

Figure 4.10. Specific volumes of silica polymorphs as a function of pressure. Experimental results (solid squares with error bars) are compared with the equation of states from simulation (dashed open circles): α-quartz (red, space group $P3_121$), quartz II phase (blue, space group P1), quartz III phase (orange, space group C222) and monoclinic post-stishovite (purple, space P2/c).

4.2.4 Change of enthalpy of silica polymorphs

The changes of enthalpy under pressure for many silica polymorphs are shown in Fig. 4.11. The enthalpy curves for three additional competing six-coordinated silica phases are provided: stishovite, the $CaCl_2$-type silica[19] and the α-PbO_2-type silica[20].

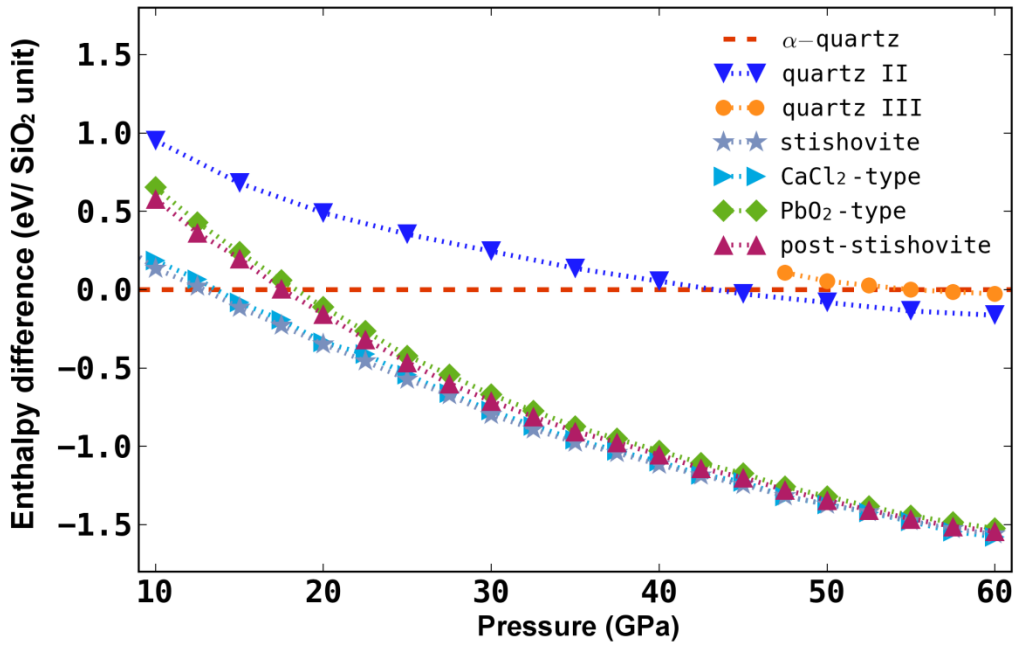

Figure 4.11. Changes of enthalpy of seven compressed silica polymorphs at different pressures: α-quartz (space group $P3_121$), quartz II phase (space group P1), quartz III phase (space group C222), monoclinic post-stishovite (space group P2/c), stishovite (light blue stars, space group $P4_2/mnm$), $CaCl_2$-type post-stishovite (space group Pnnm) and α-PbO_2-type post-stishovite (space group Pbcn). The enthalpies are presented with respect to α-quartz. Note that at the pressure range of 30-60 GPa, the enthalpies of the competing post-stishovite structures are virtually indistinguishable.

At low pressures (<10 GPa), α-quartz is more energetically favored among all the calculated silica polymorphs. However, the four-coordinated silica structure becomes less stable than its six-coordinated polymorphs at upper mantle pressure (*e.g.* stishovite is predicted more energetically favored above 12 GPa). In the range of 30-60 GPa, six-coordinated silica is energetically stable, however, the enthalpies of four competing highly coordinated silica phases are virtually indistinguishable. The more accurate results on the change of free energy, which contains vibrational energies at 300 K will be

illustrated in section 4.2.5. In order to reproduce the transition in the experiment, first-principles MD with metadynamics was performed at various pressures (30, 35 and 40 GPa). The results from metadynamics simulations are discussed in section 4.3.

As has been discussed in section 4.1.6, the phase transition from α-quartz to the post-stishovite phases is of a reconstructive type, where an intermediate quartz II phase which involves large atomic displacements. If such a transition is thermodynamically prohibited (*e.g.* compressed at very low temperatures), the calculations also predict a second enthalpy crossover at 50 GPa, where a new silica structure (named as quartz III here) is more energetically favorable. The thermodynamic driving force for such a structural transformation is discussed in chapter 4.4.

4.2.5 Free energy calculations

In order to establish a more accurate assessment on the phase stability of silica polymorphs, rigorous Gibbs free-energy calculations were performed by taking into account the vibration energy contribution. The Gibbs free energy $G(T,P,V)$ at certain pressure, temperature and volume can be derived as:

$$G = U_0 + F + PV \tag{4.1}$$

including cohesive energy $\boldsymbol{U_0}$, the vibrational energy term and the pressure-volume term. The vibrational free energy is estimated by assuming the quasi-harmonic approximation (QHA), which treats vibrations as if they do not interact. Under this approximation the system is equivalent to a collection of independent harmonic oscillators, establishing the quantum mechanical energy levels of the system. In the QHA, the vibrational free energy $\boldsymbol{F(T,V)}$ is computed from[21]:

$$F(T,V) = \frac{1}{2}\sum_{\mathbf{q},s} \hbar\omega(\mathbf{q},s) + k_B \sum_{q,s} \ln\left\{2\sinh\frac{\hbar\omega(\mathbf{q},s)}{2k_B T}\right\} \tag{4.2}$$

where $\omega(\mathbf{q},s)$ the phonon frequency of the *s*th mode for a given wave vector **q**; k_B is the Boltzmann constant, h Plank's constant and T the temperature. The pressure P is then calculated explicitly as a derivative of the free energy with respect to volume V.

$$P = -\frac{\partial(U_0 + F)}{\partial V}|_T \tag{4.3}$$

Based on the calculations of the free energy on a variety of pressures, the equation above can be used to interpolate the free energy over a wide range of pressures:

$$F_i = F_{i-1} - (U_{0i} - U_{0i-1}) - P_i(V_i - V_{i-1}) \tag{4.4}$$

The interpolated vibrational free energy F_i is propagated from its neighboring cohesive energy U_{oi} and volume V_i by the forward Euler method.

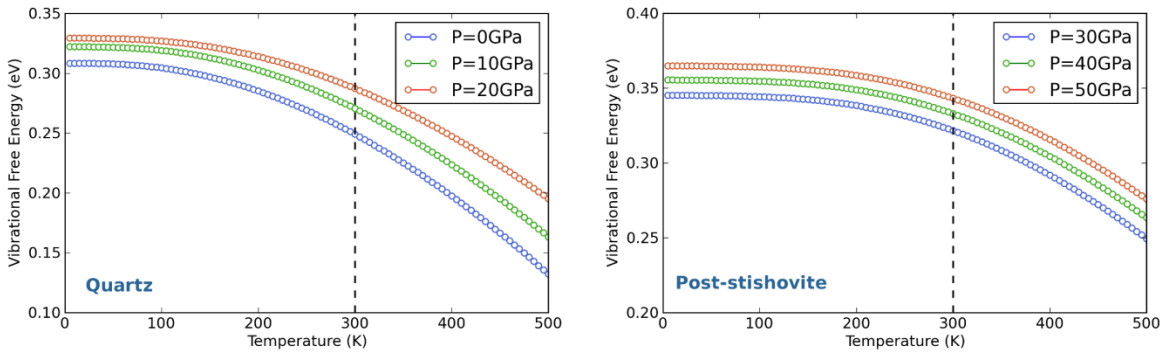

Figure 4.12. Temperature dependence of the vibrational free energy per SiO_2 unit for α–quartz and post-stishovite silica phases.

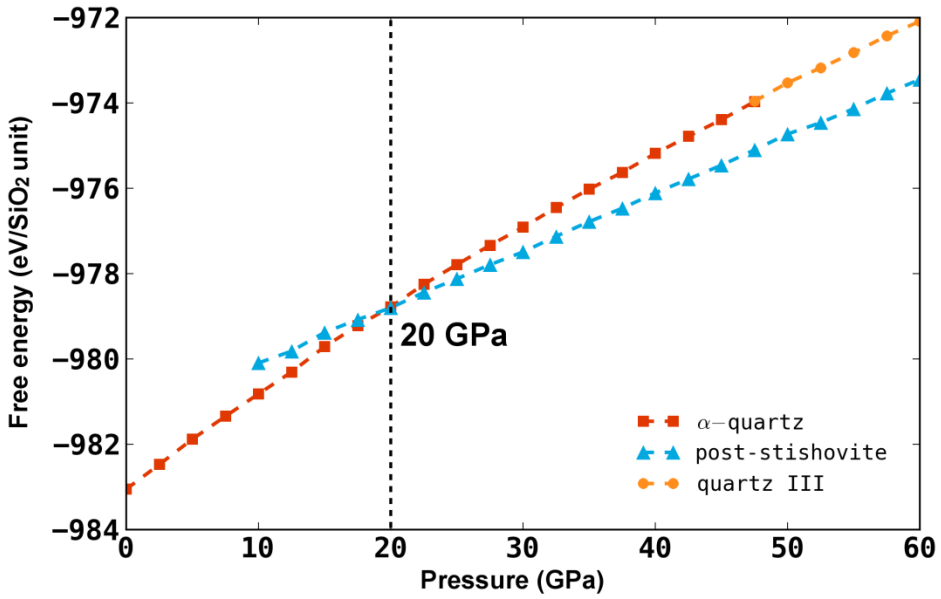

Figure 4.13. Pressure dependence of calculated Gibbs free energy for α-quartz (red squares), quartz III (orange dots) and post-stishovite (blue triangles). In addition to enthalpy, the vibration free energy is included as a part of the total Gibbs free energy. The transition pressure to post-stishovite is exactly at 20 GPa.

Fig. 4.12 shows examples of the vibration free energy for the α-quartz and post-stishovite phases at their equilibrated pressures. The vibrational contribution in the free energy increases as the system is more compressed, and is lowered as the temperature decreases. The vibration energy at 300 K and the interpolated values at the equilibrated pressures has been calculated for both α-quartz and post-stishovite phases (Fig. 4.13).

The driving force for the transition from α-quartz to post-stishovite was rationalized by assessing the Gibbs free energies of the phases from first-principles calculation. The thermodynamic analysis at 300 K (see Fig. 4.13) indicates that the free-energy crossover of the two phases occurs at 20 GPa. The post-stishovite is predicted to

be more stable than the α-quartz phase after the energy crossover. The theoretical prediction is in excellent agreement with the experiments where the stable monoclinic post-stishovite phase only appears at pressures at 20~25 GPa, signifying a *thermodynamic* catastrophe of α-quartz at room temperature.

4.3 Metadynamics

While thermodynamically permissible, the actual phase transition is dictated by its kinetics to overcome local energy barriers. Metadynamics simulations have been carried out as a barrier crossing method to survey the free energy landscape of the phase transition.

4.3.1 Metadynamics simulations for α-quartz

Metadynamics simulation was performed with the CPMD package[22] using the same BLYP type pseudopotential. A $2\times2\times1$ α-quartz supercell (36 atoms) was slowly compressed to three pressures, 30, 35 and 40 GPa, respectively. The simulation system was equilibrated for 2 picoseconds at 300 K with *ab initio* MD in an NPT ensemble. During *ab initio* MD simulation, the fluctuations of fictitious electron kinetic energy were restricted by a velocities scaling in a range of ±300 K while the nuclear degree of freedom was controlled by the Nosé-Hoover chain thermostats[23].

Table 4.3. Scaling factors and gaussian shape parameters for the metadynamics simulation at various pressures.

	α_1(a)	α_2(c)	α_3(coordination)	δ_s(a.u.)	$h(k_bT)$
30 GPa	3.5	4.5	2.0	0.08	1.0
35 GPa	4.0	4.0	2.0	0.06	1.0
40 GPa	4.0	4.0	2.0	0.05	1.0

For the metadynamics simulation of the phase transition from α-quartz to post-stishovite, numerous test runs were performed on many order parameters, and the most efficient CVs were extracted. The collective variables were eventually chosen to be the cell-edges (lengths) of the *a* and *c* axis as well as the average coordination number of silicon atoms. The values of the scaling factors and Gaussian shape parameters are listed in the Table 4.3.

The Gaussian shape, determined from the fluctuation of collective variables at the tested run, becomes shallower as simulation pressure increases. This is expected since the shrinkage of crystal volume constrains the thermodynamical fluctuation of crystal lattice. The optimized Gaussian shape is ensured to work efficiently until a phase transition is observed, where according to the prescription[24], the simulation should restart with a new set of parameters. However, in these cases, the restart is not necessary and the same set of variables is applied without any problems to study the whole sequence of transition.

4.3.2 Phase transformation to the quartz II structure

Through *ab* initio metadynamics simulation, we successfully map out and resolved

the structures of the intermediate quartz II phase and the monoclinic-type post-stishovite, and quantified the energy barriers for the transition. The phase transformation from α-quartz to quartz II (space group P1, see lattice parameters in Table 4.4) takes 52 metasteps at 35 GPa and 300 K to complete. Quartz II has alternating layers of six-coordinated octahedra and four-coordinated tetrahedral where the number ratio of octahedra and tetrahedral is 2:1 (Fig. 4.14c-f), characterized by its 3×2 kinks of octahedral chains (Fig. 4.14e). Oxygen atoms in the quartz II phase form an ordered C2 type of sublattice. The octahedra chains are forming along on the (100) plane, building up the layered structure (Fig. 4.14 a&b).

Table 4.4: Lattice parameters for the quartz II structure (space group P1) at 35 GPa. The structures are taken at the 70th metastep from my metadynamics simulation and are fully optimized for cell variable and atomic positions.

	Simulation, P=35 GPa
Space group	P1
Z	12
a (Å)	8.806
b (Å)	8.462
c (Å)	4.379
α	92.05
β	89.36
γ	119.48
ρ (g/cm^{-3})	4.21

In order to identify the transition sequence, the coordination number is calculated

along the trajectory of the metadynamics simulation. The coordination number of Si is calculated by counting the number of oxygen atoms around Si atoms with a 2.3 Å radial cutoff. The cutoff is taken from the first peak distance in the radial distribution function at each individual pressure.

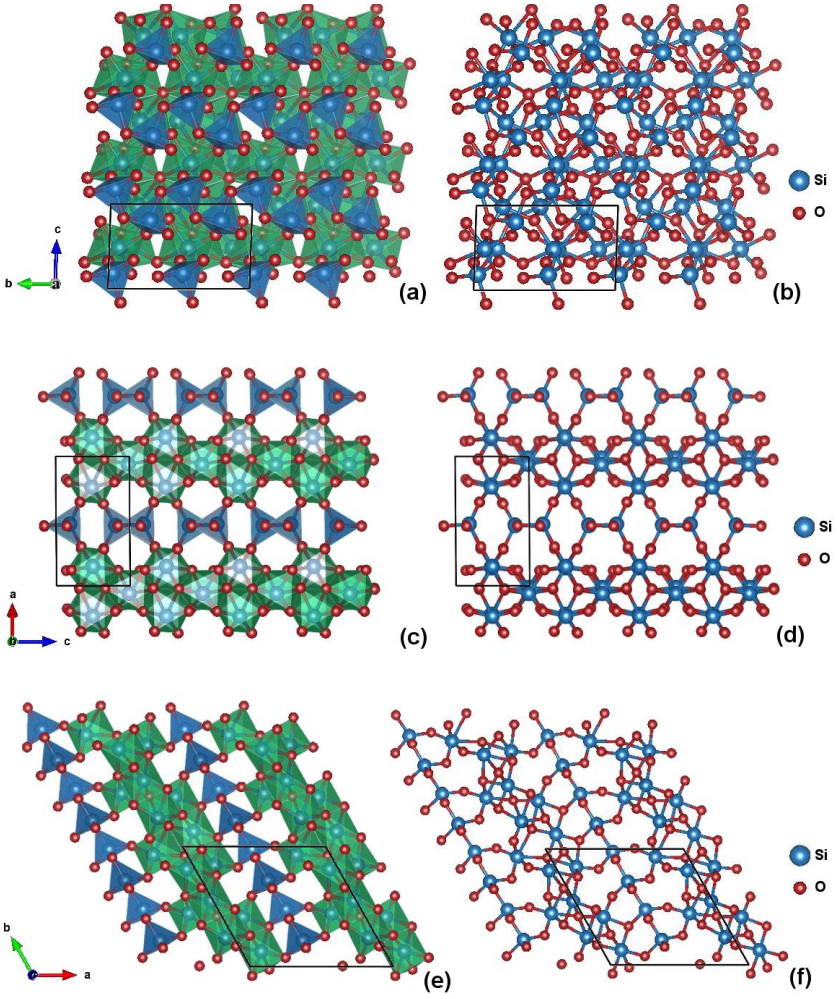

Figure 4.14. Snapshots of the quartz II (P=35 GPa) projected along the (a)(b) *a*-axis, (c)(d) *b*-axis and (e)(f) *c*-axis. The polyhedron representations are shown on the left panel, where four-coordinated tetrahedra are colored in blue and six folded octahedral are colored in green. One simulation unit cell of silica (32 atoms) is plotted in solid frame.

As shown in Fig. 4.15, the number of six-coordinated silicon atoms jumps to 8 at 57th metastep. During this transition, 2/3 silicon atoms become six-coordinated. The intermediate quartz II phase is the metastable phase. In the metadynamics simulation, it is stable for another 27 metasteps before transforming to the post-stishovite phase (Fig. 4.15 and Fig. 4.16c).

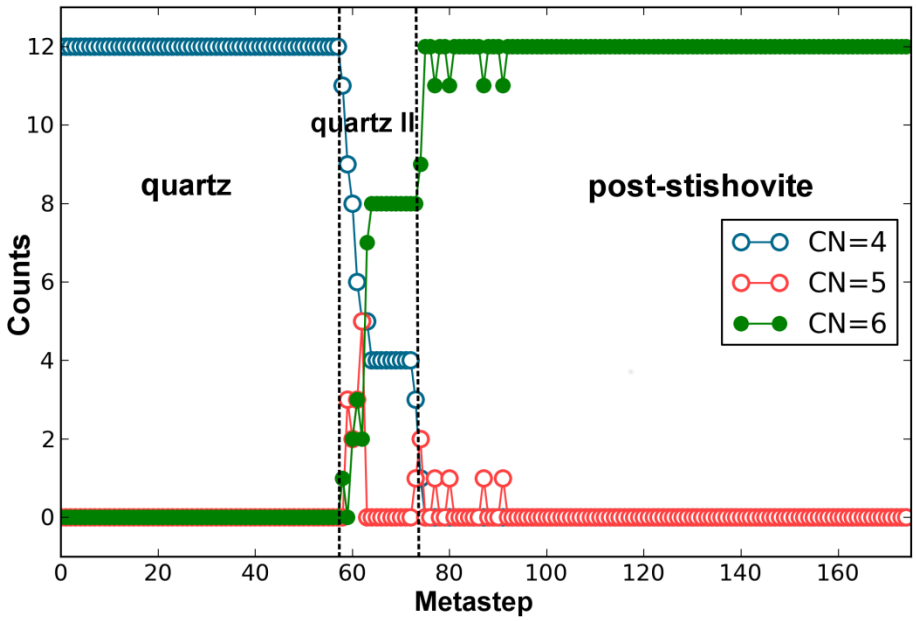

Figure 4.15. The evolution of the coordination number of Si atoms along the *ab initio* metadynamics simulation. The bond length threshold between Si and O was set to be the distance of first peak in the radial distribution function. The quartz II structure has mixed octahedra and tetrahedra in 2:1 ratio. With prolonged metadynamics steps, the coordination number of all Si atoms changes to six, indicating the formation of the new post-stishovite phase.

Different from the four metastable structures observed in compressed coesite, the

coexistence of other intermediate phases is not observed in quartz. The quartz II phase is reproduced in all the metadynamics runs.

4.3.3 Free energy landscape

Unlike the previously reported barrier free process[3], the transition from α-quartz to quartz II at 35 GPa and 300 K requires to overcome an energy barrier of ~1 k_bT. The energy barrier is estimated from the dip height of α-quartz on the reconstructed free energy surface (Fig. 4.16a).

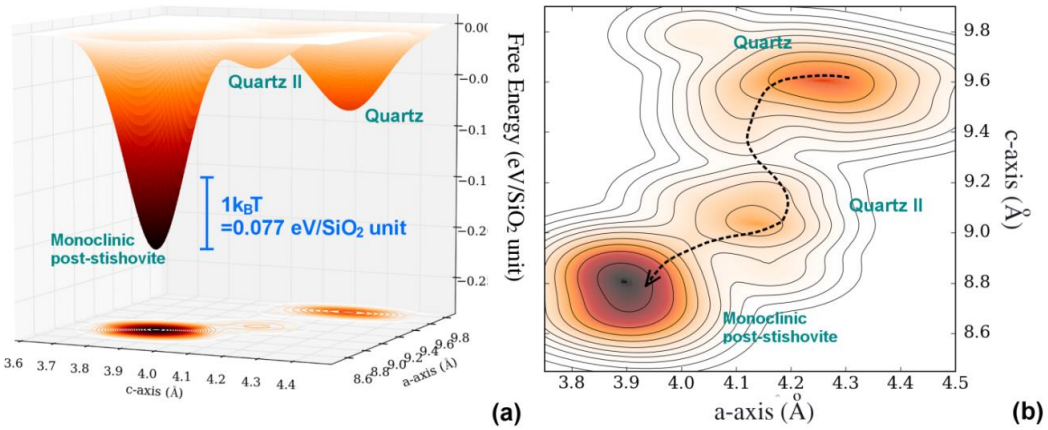

Figure 4.16. Reconstructed free-energy landscape showing the transition pathway from α-quartz to post-stishovite. The energy landscape is obtained from *ab* initio metadynamics simulation at 35 GPa and 300 K (see text) and is projected along the *a*- and *c*-axis of the SiO_2 simulation unit cell. A hypothetical transition pathway, corresponding to the minimum energy path, is shown in the right panel (dotted line). One local energy minimum, the metastable quartz II phase, is present between the stable α-quartz and post-stishovite phases. The mechanical stability of quartz II has been confirmed with phonon calculations, where no imaginary vibration modes is identified.

A minimum energy path is found on the free energy surface (Fig. 4.16b), qualitatively showing the changes of cell edges during the transition. The free energy landscape is also projected along another two combinations of collective variables (coordination number *vs.* cell edge *a* or *c*) (Fig. 4.17), where the heights of kinetic barriers are consistent with the height from Fig. 4.16. The evolution of enthalpy and lattice parameters is quantitatively shown in Fig. 4.18. During the process, the cell-edge of the *a*-axis is compressed by 8.7% while the *c*-axis is compressed by 7.0%, leading to a 10.9% volume collapse. The length of the *b*-axis of the simulation box, however, stays almost unchanged throughout the phase transition. The volume drop, achieved by the compression of the *a* and *c* axes, forms edge-sharing octahedra chains along the (100) plane in the quartz II phase (Fig. 4.14). The calculated diffraction patterns of quartz II are in good agreement with the experiments (Fig. 4.4), confirming the validity of the derived quartz II structure.

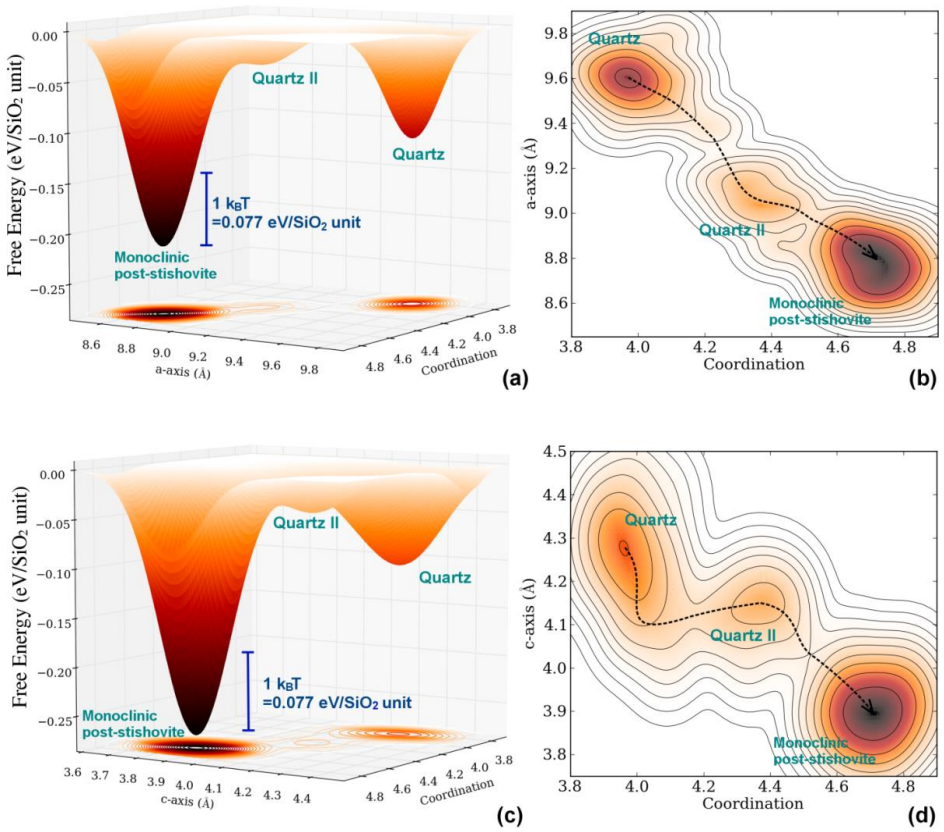

Figure 4.17. Reconstructed free-energy landscape with the changes of Si coordination number. The energy landscape is obtained from *ab initio* metadynamics simulation at 35 GPa and 300 K (see text) and is projected along the two combination of collective variables: (a)(b) *a-axis* and Si coordination number, (c)(d) *c-axis* and coordination number. One local energy minima, the metastable quartz II phase, is present between the stable α-quartz and post-stishovite phases. The height of the kinetic barrier from quartz to quartz II is consistent with the energy landscape projected along the *a* and *c* axis.

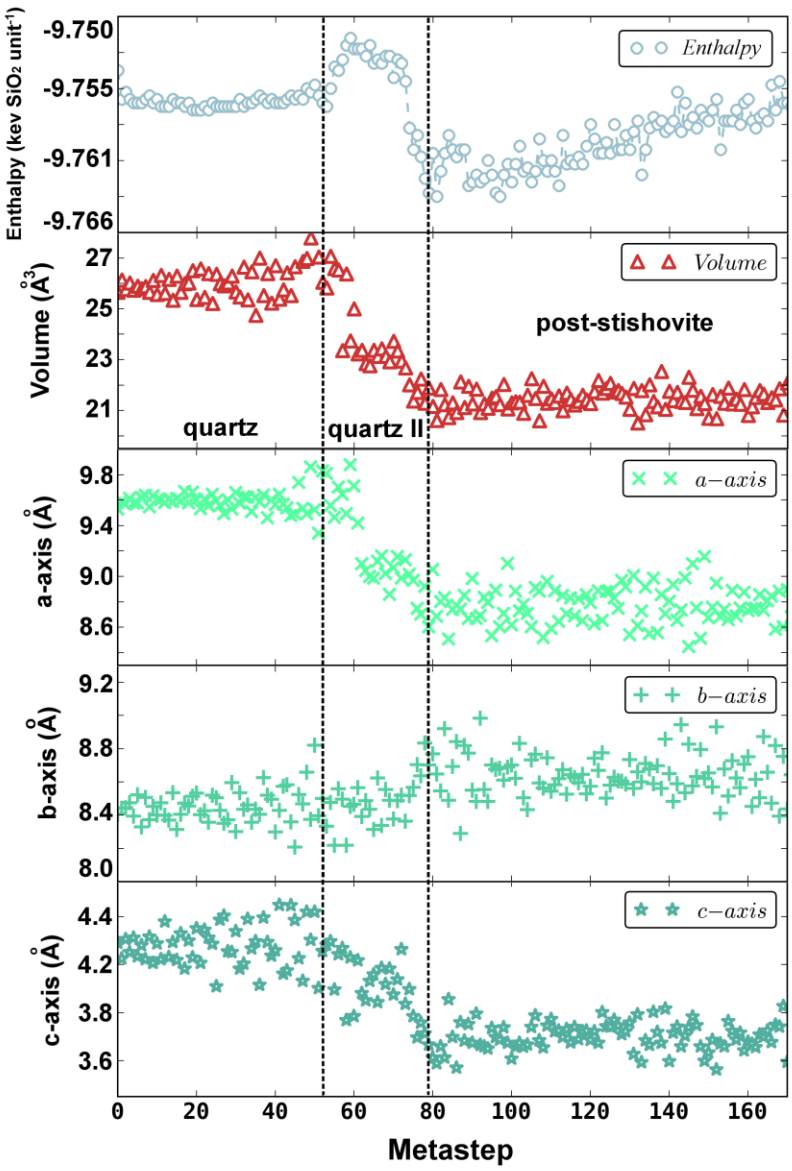

Figure 4.18. The evolution of enthalpy, volume and lattice parameters of SiO_2 (starting from α-quartz) along the *ab initio* metadynamics simulation sampling the potential energy surface. The simulation was carried out at 300 K and 35 GPa.

4.3.4 Phase transition to the post-stishovite phase

With prolonged metadynamics simulation (*e.g.*, 79 metasteps at 35 GPa, Fig. 4.15-18), the system is able to escape from the energy well of quartz II, and transforms into the stable monoclinic-type post-stishovite phase (P2/c), which has the same structure as I have observed in the experiment. Since no further phase transitions are observed after another 300 hundred metasteps, I stop the metadynamics simulation where the difference in deposited energy for the α-quartz and post-stishovite matches what they have been predicted from thefree energy calculations (Fig. 4.13). During the phase transition from quartz II to the more stable post-stishovite phase, a large enthalpy drop is observed after overcoming a small free energy barrier (0.5 k_BT from Fig. 4.18). Volumes continue to drop by 8.7%, mainly contributed by compression of *a*-axis (4.4%) and in *c*-axis (12.2%), which agrees well with the experimental EOS in Fig. 4.10.

The monoclinic type post-stishovite structure has edge-sharing octahedra arranged along the [100] direction of the original simulation box (Fig. 4.19). The unit cell, which contains four silicon atoms and eight oxygen atoms, is checked for mechanical stability by phonons calculations on the fully optimized structure at 35 GPa (see Fig. 4.20). No negative modes are identified, confirming it is truly mechanically stable. The crystallographic data of the post-stishovite structure matches reasonably well the experimental results, shown in Table 4.1.

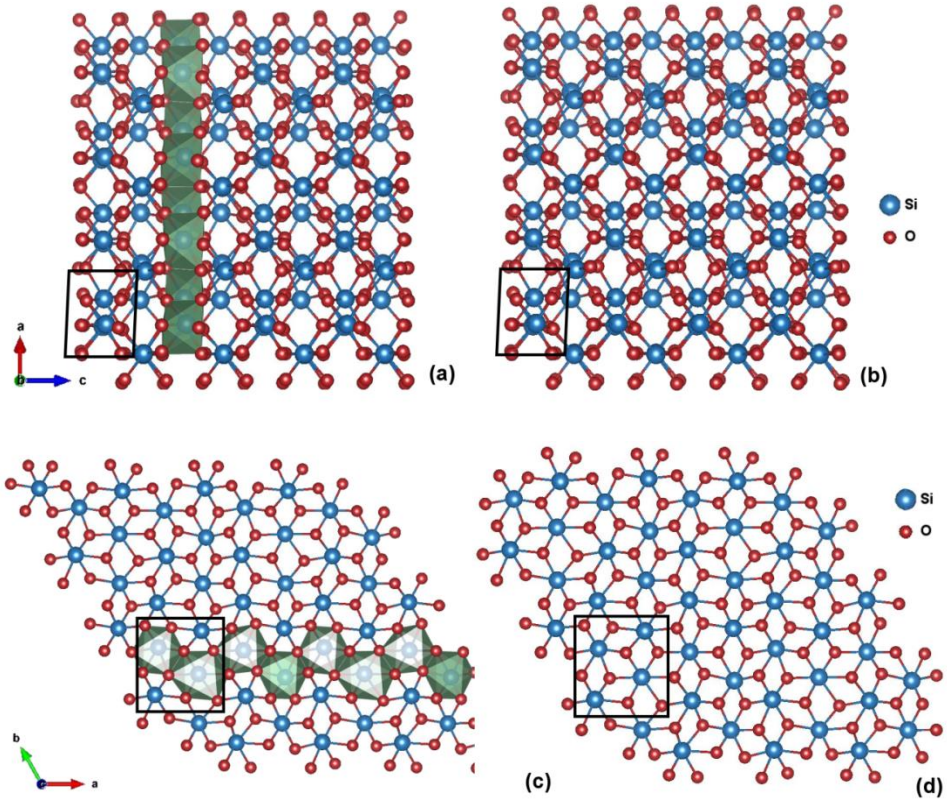

Figure 4.19. Representations of the post-stishovite structure projected on the (a)(b) (010) plane and (c)(d) (001) plane. The structures are taken from *ab initio* metadynamics at 35 GPa and 300 K. The left-hand figures show the formation of edge sharing octahedra chains (colored in green). The figures on the right show the stacking layers of six-folded silicon-oxygen frameworks. One unit cell of monoclinic type post-stishovite (space group P2/c, 12 atoms per unit cell) is sketched in the black solid box.

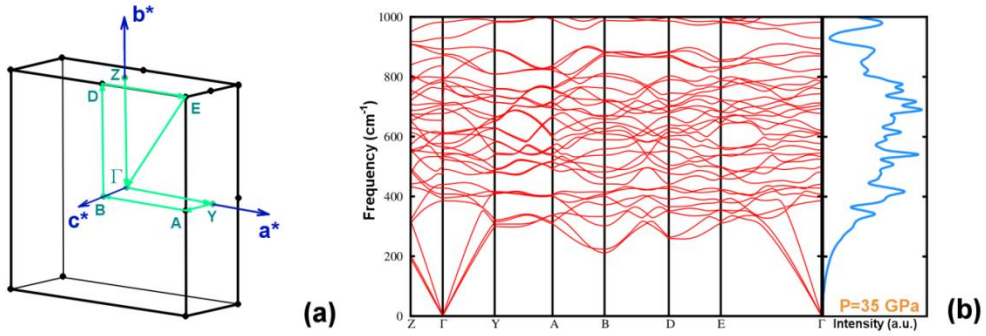

Figure. 4.20. Phonon dispersion curves and total vibrational density of states for monoclinic post-stishovite at 35 GPa. (a) Dispersion sampling direction in the monoclinic Brillouin zone along the high symmetry points. (b) Phonon dispersion curve with phonon density of states for the monoclinic post-stishovite at 35 GPa. The post-stishovite is extracted from metastep 150 of the metadynamics simulation and convert to a monoclinic-type lattice unit.

4.3.5 Pressure dependence of the transition pathways

The same phase transition is also reproduced at 30 GPa and 40 GPa using the same computational methods (Fig 4.21). The phase transformation from α-quartz to post-stishovite requires significant rearrangement of both anions and cations, corresponding to a thermally activated process. At room temperature, the thermal energy is not enough for the system to overcome the kinetic energy barrier quickly, and consequently, compressed silica undergoes a sluggish kinetic process, manifested by the coexistence of multiple phases over a wide pressure range, which is exactly what have been observed in the experiment. The amount of energy triggering the rearrangement, relative to the free energy barrier, significantly increases at higher pressure (*e.g.* at 40 GPa, Fig. 4.21d).

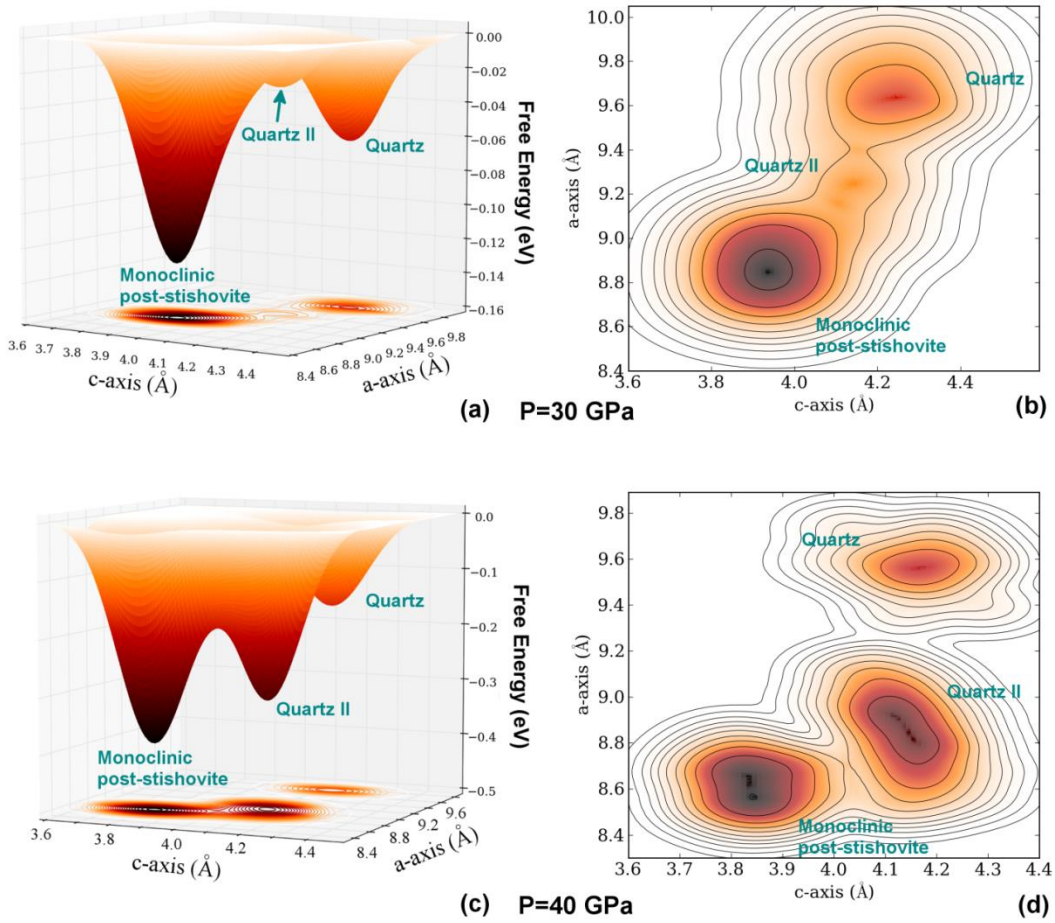

Figure 4.21. Reconstructed free-energy landscape at 30 and 40 GPa. (a)(b) 30 GPa and (c)(d)40 GPa. The energy landscape is projected along *a-axis* and *c-axis*. The dip height of the compressed quartz and the quartz II phase significantly increases at 40 GPa, indicating the energy barrier is much higher in a close-packed system. The order parameters monitored during the phase transition (the coordination number, *a* and *c*-axis) at all pressures are comparable, as the same intermediate quartz II phase is observed and the final post-stishovite phase has the same space group at 35 GPa.

4.3.6 Mechanical instability examined by phonon calculations

The mechanical stability of the quartz II phase was checked in two steps. After

extracting the structure from the metadynamics simulation, a set of *ab initio* MD simulation has been carried out to study its thermal instability (*e.g.* 10^5 MD steps, equal to 2.4 picoseconds, at 300 K). The equilibrated structure is shown in Fig. 4.14, where the original atomic positions in quartz II are well kept. The quartz II structure was then completely optimized for atomic position, volume and cell shape using a Quasi-Newton algorithm to reach the local minimum energy state.

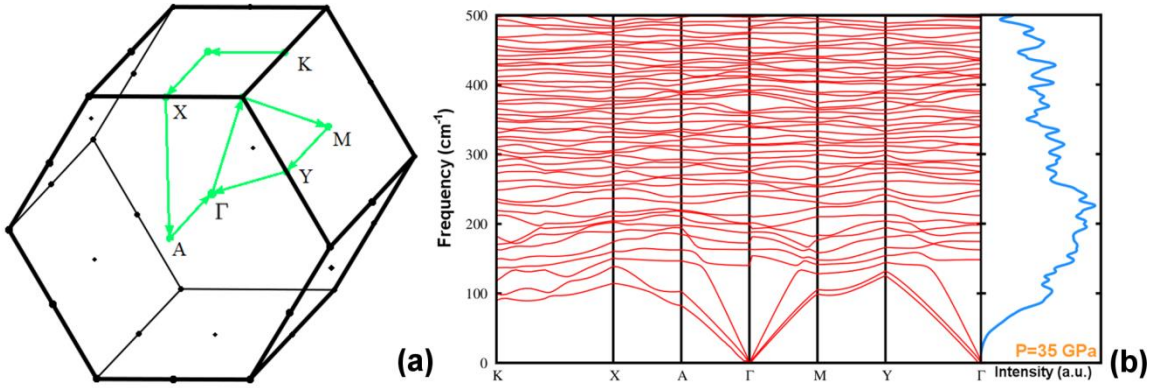

Figure 4.22. Phonon dispersion curves and total vibrational density of states for quartz II structure at 35 GPa. (a) Dispersion sampling direction in the Brillouin zone of the simulation cell. (b) Phonon dispersion curve with phonon density of states for the quartz II phase at 35 GPa. The post-stishovite structure was extracted from metastep 70 of the metadynamics simulation. Phonons were calculated for the fully optimized structure at the same pressure.

The mechanically stability was further tested by calculating the phonon dispersion curves (Fig 4.22). The simulation used the above mentioned BLYP-type pseudopotential and a plane wave cutoff of 200 Ry. A 2×2×2 Monkhorst-Pack mesh was adopted to

ensure that the geometric optimized simulation cell achieves an energy convergence to 2.1×10^{-9} eV, and the forces acting on each atom less than 0.05 eV/Å. The vibrational frequencies were collected by finding the eigenvalues of the interatomic force constant matrices on a grid of *q*-vectors same as the k-point mesh. Then the Fourier interpolation is performed to calculate the modes along the high symmetry points in the Brillouin zone.

No negative modes are identified at 35 GPa, implying the intermediate quartz II phase is mechanically stable. The X-ray diffraction patterns (Fig. 4.7) also support the observation of quartz II phase in pressure range of 25-45 GPa, reproducing the simulation results.

4.4 *Ab initio* molecular dynamics

The transition from α-quartz to the post-stishovite phase requires significant rearrangements of both cations and anions. This reconstructive phase transition of α-quartz is a thermally activated process. At room temperature, the thermal energy is not enough for the system to overcome the kinetic energy barrier rapidly, and consequently, compressed silica undergoes a sluggish kinetic process, manifested by the coexistence of multiple phases over a wide pressure range, which is exactly what have been observed in the experiment.

Naturally, if the phase transition described above is kinetically prohibited, *e.g.*, at very low temperatures where the kinetic energy is far below the phase transition energy barrier, the α-quartz phase will be trapped in the local energy minimum of the potential well, being kept metastable to even higher pressures. As such, the ultimate stability of α-

quartz is controlled by a new transition mechanism.

4.4.1. Computational details

First-principles MD is highly computationally demanding, *e.g.* the classic Born-Oppenheimer MD (BO-MD)[25] requires self-consistency calculation on each time step. BO-MD with 10^5 timesteps in magnitude is approaching the computational limit using state-of-the-art computational hardware, which is still too short to ensure system running at equilibrium conditions. Therefore we performed *ab initio* MD on the Car-Parrinello scheme[26,27] in CPMD for the following considerations: (i) The BLYP type pseudopotential used in CPMD predicts the correct equation of state of silica at low pressures (Fig. 4.8), however it is not as much computationally demanding as the hybrid HSE potential, which also produced simulational results that match the experiments. (ii) Though the BLYP type exchange-correlation functional requires a much higher plane wave cutoff (a typical cutoff of is 170 Ry, which is four times what is used in VASP), the nuclear and electronic coordination are separated in CPMD, significantly reducing the overall computational time. The simulation of the phase transition can thus be achieved at a reasonable computational cost. (iii) CPMD has comprehensive supports for barrier crossing algorithms, like metadynamics. The same GGA type pseudopotential with the BLYP parameterization was employed for α-quartz simulations in CMPD. However, a 170 Ry kinetic energy cutoff is needed to ensure accurate evaluation of pressure and lattice parameters. A $2\times2\times1$ α-quartz unit cell was gradually compressed to 50 GPa under a NPT ensemble (constant particle number, pressure and temperature[28]). The temperature was conserved at 300 K by the Nos é-Hoover thermostat[23].

We performed first-principles MD (without running metadynamics) for this purpose. The results discussed here are based on regular *ab initio* simulation, which turns out to be inefficient in overcoming the energy barrier at low temperatures (e.g., 300 K) and certain pressures (e.g., 40 GPa). In the following sections, I will illustrate that the transition actually becomes a barrier-free process at room temperature and high pressure.

4.4.2. Lattice distortion of α-quartz

At 40 GPa, the signature six-member ring structure is distorted but the tetrahedra framework is still kept (Fig. 4.23a&b). As reported by many pioneering works[29-31], the distortion involves simultaneous rotation of all SiO_4 helical spiral along the [110] axis and the Si-O-Si bond angle approaches to 120 °upon lattice compression (Fig. 4.24).

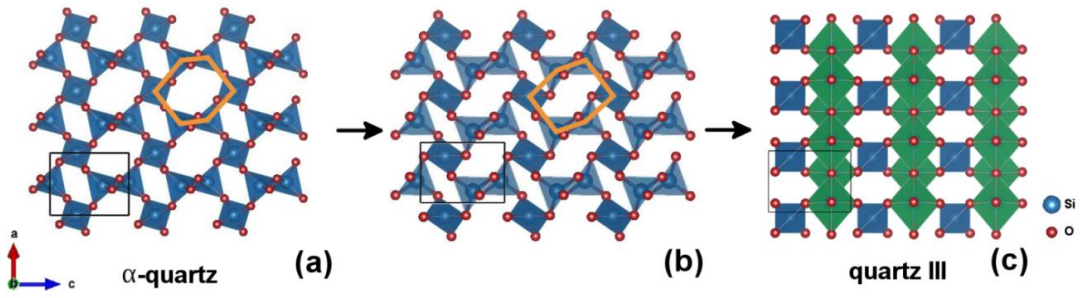

Figure 4.23. Structural representation with polyhedrons of (a) quartz (P=1 bar), (b) distorted quartz (P=35 GPa) and (c) quartz III (P=50 GPa) structures projected along the *b*-axis. The cornered sharing tetrahedra are colored in blue and edge sharing octahedra are colored in green. One computational unit cell of silica is sketched in black solid frame. The signature six-member ring in α-quartz (labeled in orange solid lines) is stretched along the [101] axis under pressure, forming the layered six-coordinated octahedra structure above 50 GPa.

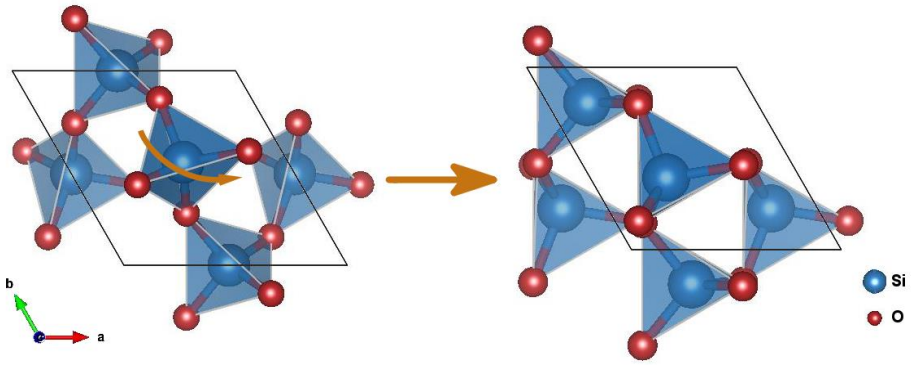

Figure 4.24. Structural changes of distorted α-quartz. The distortion involves the rotation of silicon polyhedron along the [110] axis.

4.4.3. Formation of the quartz III structure

It is interesting to point out that beyond 50 GPa the edge-sharing octahedra are found forming along the (100) plane, gradually transforming into a new post-quartz phase that has not been reported before (the structural representations projected along three coordination axes are shown in Fig. 4.25-4.27). The new post-quartz phase (space group C222) has alternating layers of tetrahedra and octahedra. The projected plane along the *a*-axis clearly shows the close-packed octahedra (Fig. 4.25). The planes of edge-sharing octahedra are linked by layers of silicon tetrahedra, as shown in Fig. 4.26 & 4.27 where the atomic structure is projected along the *b* and *c* axis, respectively.

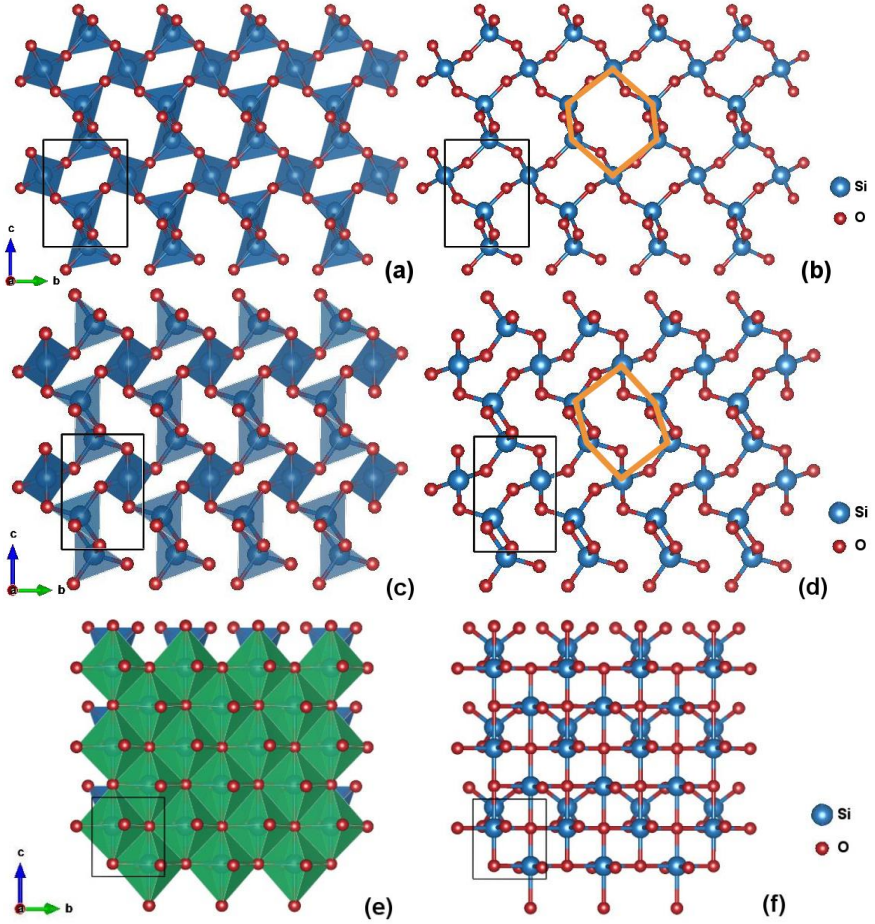

Figure 4.25. Snapshots of (a)(b) quartz (P=0 GPa), (c)(d) distorted quartz (P=35 GPa) and (e)(f) quartz III (P=50 GPa) structures along the *a*-axis. The polyhedron representations are shown on the left panel, where four-coordinated tetrahedra are colored in blue and six folded octahedral are colored in green. One unit cell of silica is plotted in the solid frame.

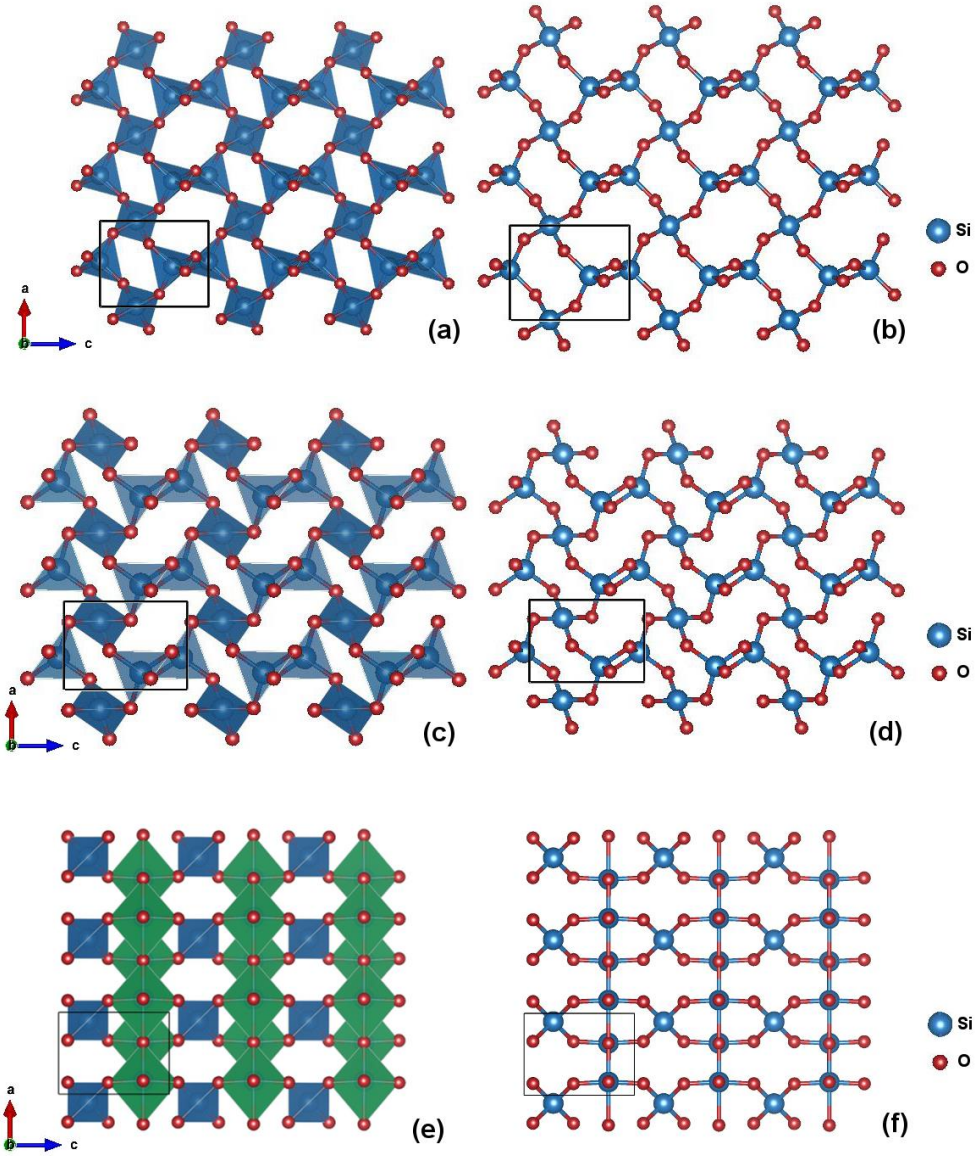

Figure 4.26. Snapshots of (a)(b) quartz (P=1 bar), (c)(d) distorted quartz (P=35 GPa) and (e)(f) quartz III (P=50 GPa) structures along the *b*-axis. The polyhedron representations are shown on the left panel, where four-coordinated tetrahedra are colored in blue and six folded octahedral are colored in green. One unit cell of silica is plotted in the solid frame.

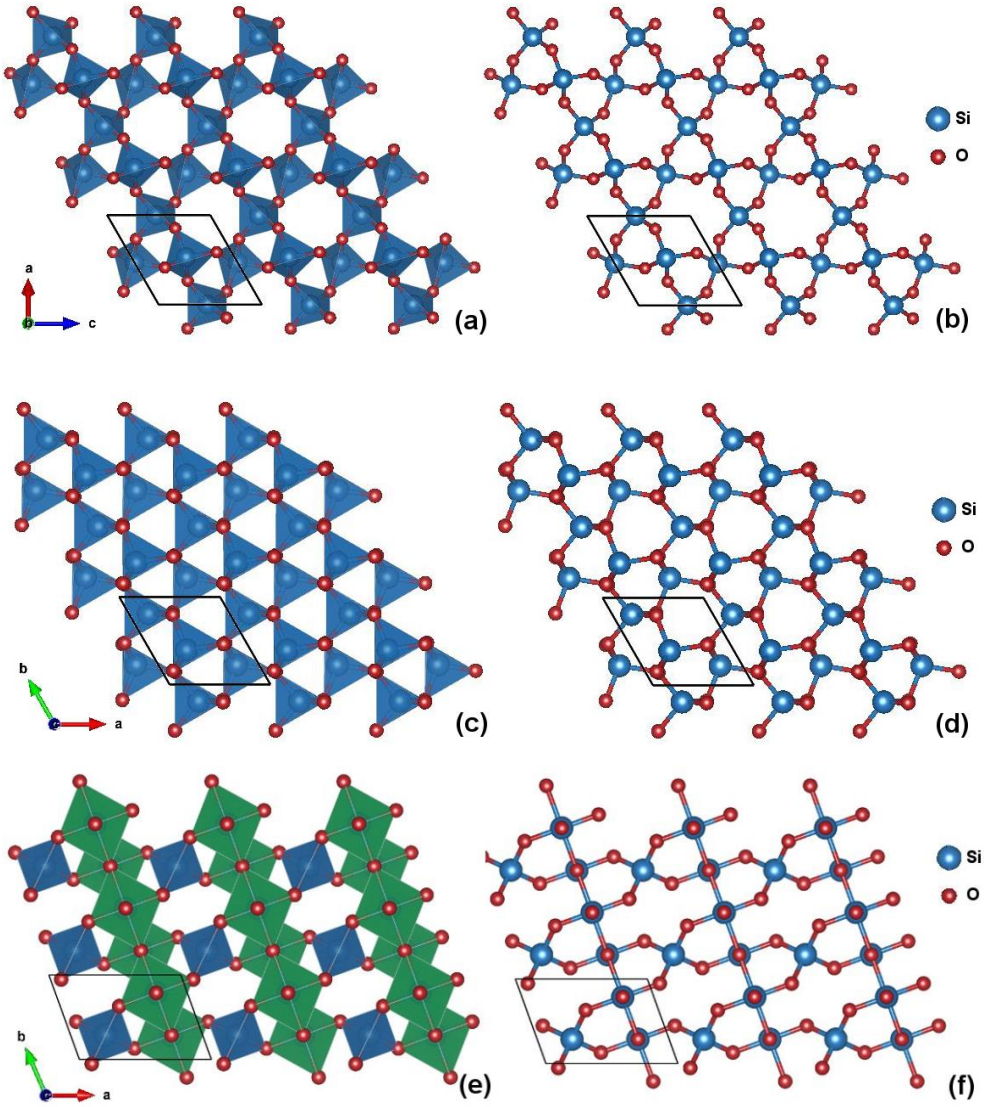

Figure 4.27. Snapshots of (a)(b) quartz (P=1 bar), (c)(d) distorted quartz (P=35 GPa) and (e)(f) quartz III (P=50 GPa) structures along the *c*-axis. The polyhedron representations are shown on the left panel, where four-coordinated tetrahedra are colored in blue and six folded octahedral are colored in green. One unit cell of silica is plotted in the solid frame.

We also calculated the geometrically optimized lattice parameters and atomic coordinates at 50 GPa (Table 4.5). The new phase, named as quartz III here, is only

metastable above 50 GPa and 300 K. It recovers to the distorted α-quartz structure after releasing pressure below 50 GPa without an obvious pressure hysteresis. Experimentally, however, the observation of the phonon instability may be preempted or obscured by other transitions pathways occurring at lower pressures. The volume change as a function of pressure has already been shown in Fig. 4.9 & 4.10.

Table 4.5: Crystallographic data for the quartz III structure (space group C222) at 50 GPa. The structures are extracted from first principles MD simulation and geometric optmized for its cell variable and atomic positions at fixed pressures employing the same pseudopotentials in the eqations of states calculations. Atoms are at its Wyckoff positions. The X-ray diffraction spectrum is calcualted with labels in Fig. 4.28.

	P=50 GPa	Wyckoff positions from simulation			
Space group	C222				
Z	6		x	y	z
a (Å)	3.637(4)	Si1 (x,y,z)	0.250,	0.250,	0.740
b (Å)	10.067(9)	Si2 (x,y,z)	0.000,	0.000,	0.000
c (Å)	3.698(7)	O1 (x,y,z)	0.250,	0.250,	0.260
ρ(g/cm^{-3})	4.42(1)	O2 (x,y,z)	0.748,	0.092,	0.243

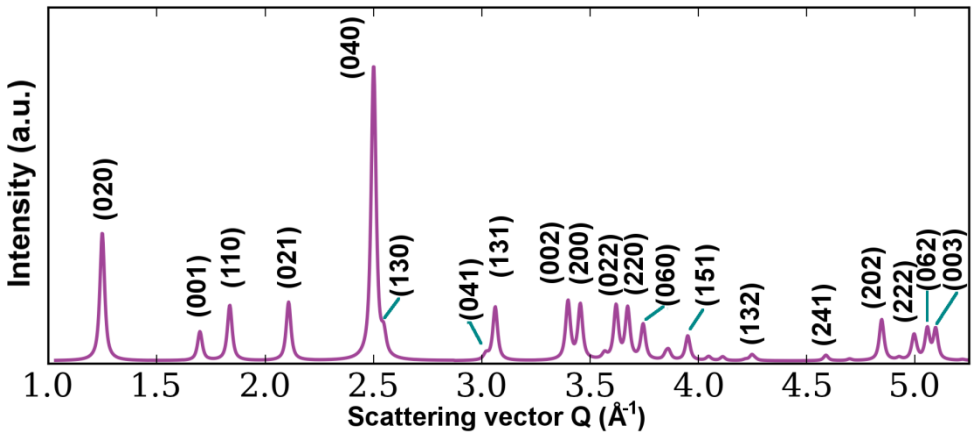

Figure 4.28. Calculated X-ray diffraction specturm for the quartz III phase at 50 GPa. The miller indices labeling are shown at each diffraction peaks.

4.4.4. Phonon calculation of α-quartz and quartz III

At very low temperatures where the kinetic energy is far below the phase transition energy barrier, the α-quartz phase will be trapped in the local energy minimum of the potential well, being kept metastable to even higher pressures. Under this circumstance, it is shown that the ultimate stability of α-quartz is controlled by the phonon softening at the K point (1/3, 1/3, 0) of the Brillouin zone boundary.

Phonon calculation was performed with the Quantum Espresso code with 200 Ry kinetic energy cutoff. All structures (quartz and quartz III) were completely relaxed at various pressures. The dynamical matrix was calculated on the 4×4×4 wave vector grid in reciprocal space, from which the interatomic force constant matrix was derived. The long-range dipole-diploe interactions were taken into account separately using the calculated dielectric tensor. Fourier interpolation was used to calculate the modes along

the high symmetry points in the Brillouin zone. The calculated LO-TO splittings at the gamma point are in good agreement with literature[34,35].

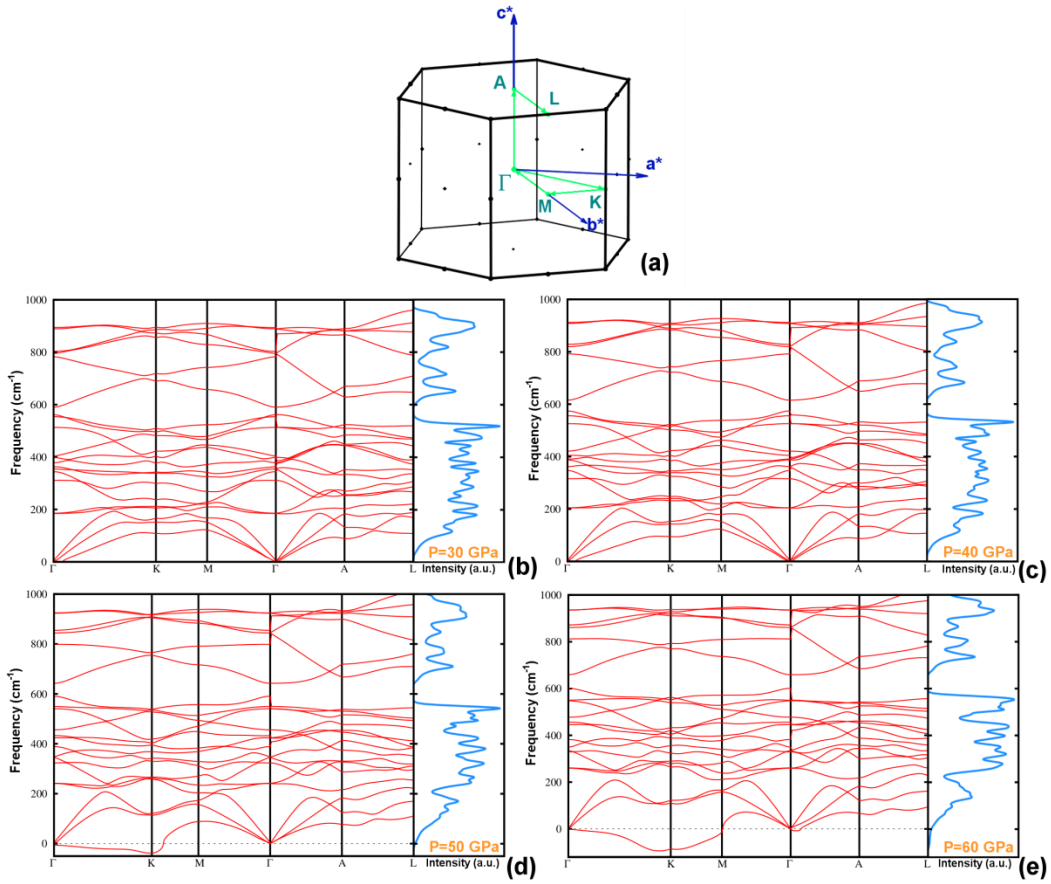

Figure 4.29. Phonon calculation of compressed α-quartz. (a) Dispersion sampling direction in the trigonal Brillouin zone along the high symmetry points. (b)-(e) Phonon dispersion curves of compressed quartz from 30-60 GPa. The Γ is the center of the Brillouin zone and other points like K, M and A are located at the zone boundary. Imaginary modes were found around K point above 50 GPa, where four-coordinated Si-O structure were no longer mechanically stable.

The phonon dispersion curves of α-quartz have been theoretically calculated in Fig.

4.29. Noticeable of the phonon dispersion curves is the phonon softening of the K point with increasing pressure, which is illustrated in Fig. 4.30. The K-point phonon instability is clearly seen when the pressure reaches as high as 49 GPa. Above 49 GPa, the negative vibrational modes around the K point indicate that atomic vibrations along the K point will destabilize the α-quartz structure, leading toward the formation of a new phase without thermal excitation (Fig. 4.31).

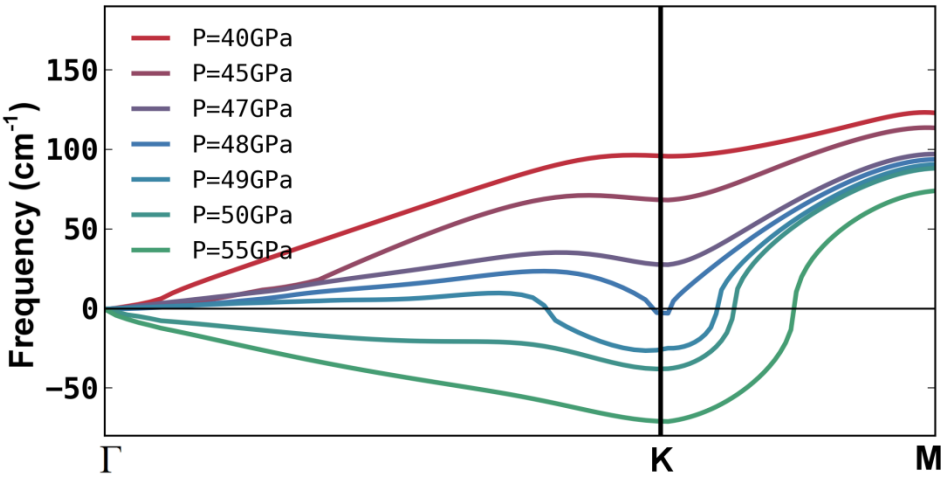

Figure 4.30. Softening of phonons at K point in the Brillouin zone. The α-quartz structures are slowly compressed over 50 GPa and are fully optimized before the phonon calculation. Negative phonon mode is observed above 49 GPa at K point, where the new quartz III is formed.

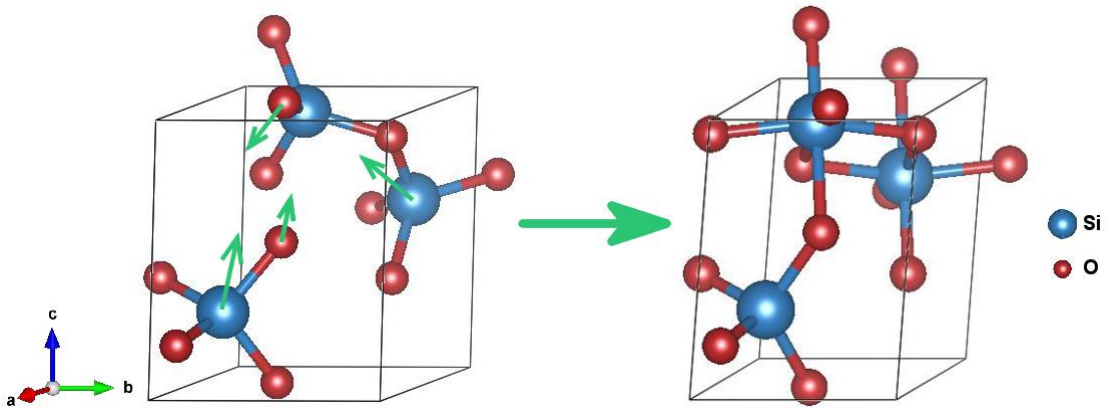

Figure 4.31. Atomic shuffling in the phase transition from quartz to the quartz III structure. The green arrows in the left figure indicate the eigenvectors of atom movement, calculated from the negative phonon modes 50 GPa.

Such a transition process involves short-distance atomic shuffling, as shown in Fig. 4.31, belonging to a diffusionless transformation process. The newly formed phase after lattice collapse has a C222 structure where anions form close-packed b.c.c like structures and one third of cations occupy the tetrahedral sites of O atoms and two thirds of the cations occupy the octahedral sites. This post-quartz phase has been previously predicted to form, but the results show this athermal process occurs at much higher pressure (above 49 GPa). The new structures are also checked for their mechanically stability at 50 and 60 GPa (Fig. 4.32), where no negative modes are recognized. The crystallographic data of the resulting post-quartz structure (see Table 4.5) is distinctly different from the quartz II phase seen in the experiment.

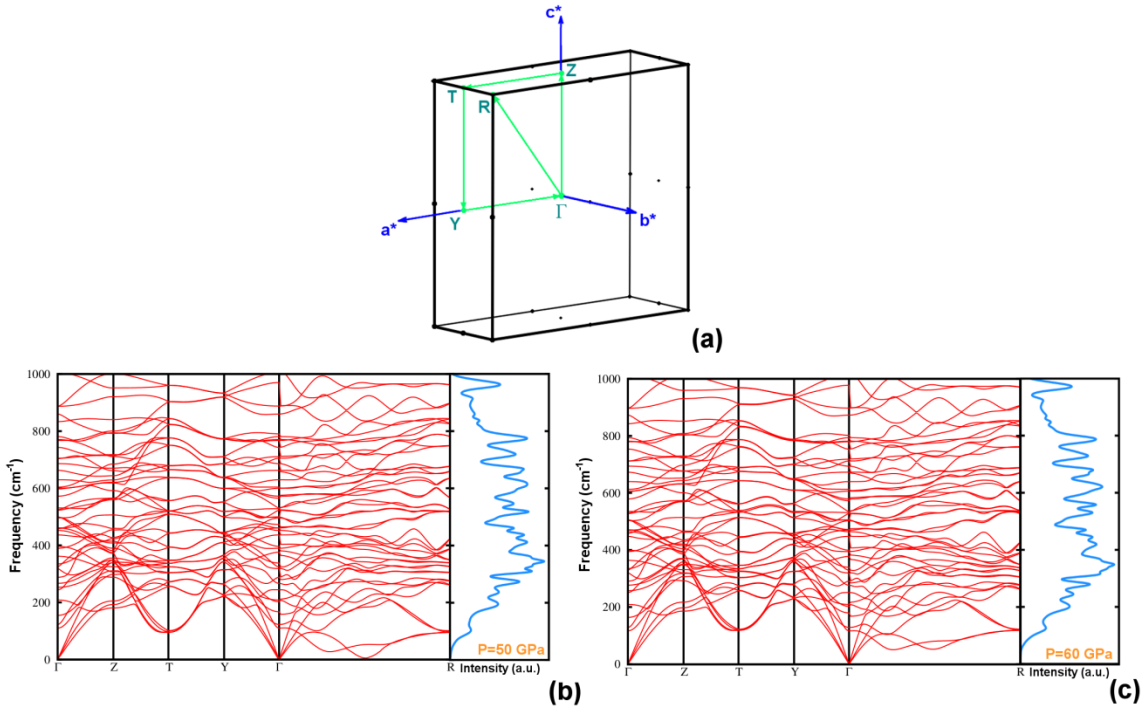

Figure 4.32. Mechanical stability for the quartz III structures. (a) Sampling dispersion path in the orthorhombic Brillouin zone. (b) Phonon dispersion curve with phonon density of states of quartz III with the C222 structure at 50 GPa and (c) 60 GPa. The post-quartz structure was geometrically optimized before calculating phonon dispersion (red curves) and total phonon density of states (blue vertical curves).

4.4.5. Transition path studied with the nudged elastic band method

To corroborate the mechanism of phonon-softening, the energy barrier separating α-quartz and the post-quartz (termed as quartz III) phase was analyzed using the solid-state nudge elastic band method[34].

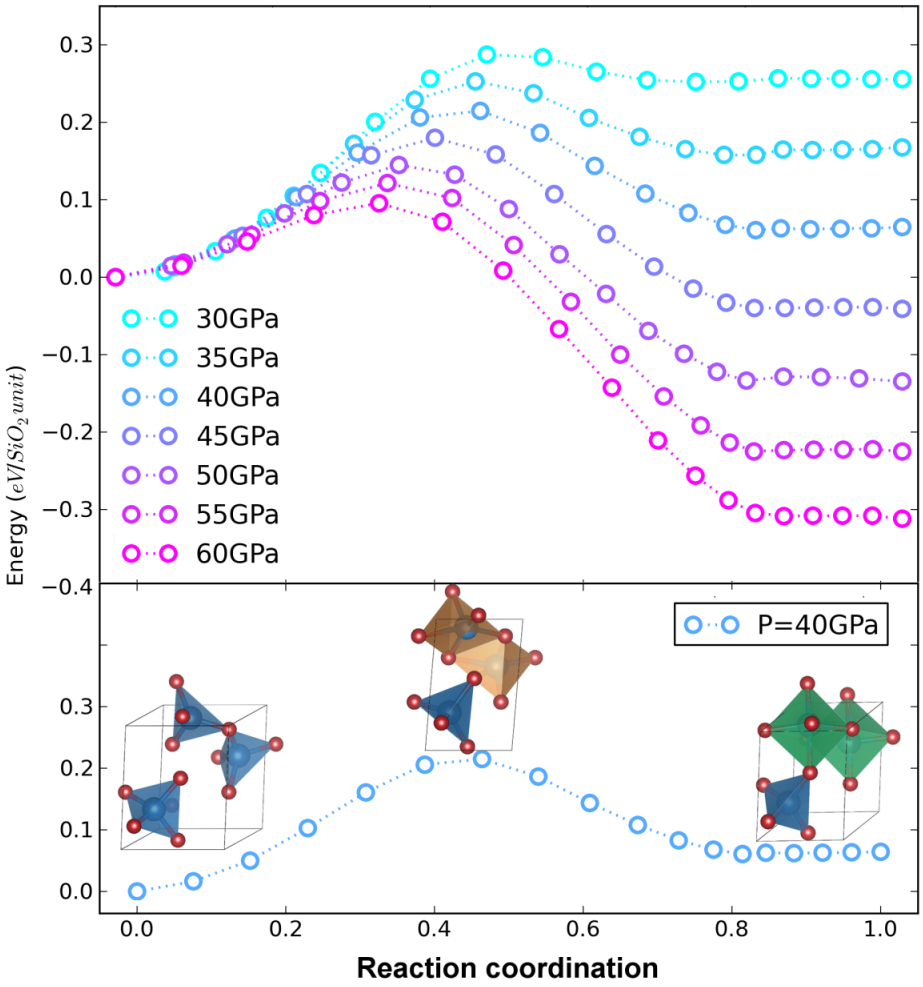

Figure 4.33. The cohesive energy values on the transition path from α-quartz phase to the quartz III phase calculated by ssNEB. The first-principles calculations predict quartz III phase is more energetically favorable than α-quartz above 45 GPa. The energy barrier from the prospective of potential energy is greatly lowered upon pressurization. The lower panel shows the structural changes along the transition pathway. The initial and final structures are α-quartz and quartz III respectively. The middle snapshot was taken from the saddle point of the transition path, where two silicon atoms are five-coordinated.

Since α-quartz is metastable at high pressure, the Hessian based geometrically

optimized method is employed so that it is possible to optimize the structure into local saddle points without transforming into the quartz III phase. Similarly, low pressure structures of quartz III were optimized under the same treatment. A total number of 16 replicas were initialized as the geometric intermediates for α-quartz and quartz III phase. The convergence of force is the signature of finding the minimum-energy path (MEP), and the energy and force of the system are calculated at each ionic step until it satisfied the preset convergence criterion (0.05 eV/Å on each atom).

The change of cohesive energy on the transition pathway is plotted in Fig. 4.33. The quartz III phase is more energetically favorable than α-quartz above 45 GPa. Also the height of potential energy barrier is much lower at higher pressure (decrease by 73% at 60 GPa compared with 30 GPa). The energy barrier in this figure may be indicative of the energy difference caused by different stacking schemes of atoms. However, the free energy change caused by the volume collapse (*i.e.*, the volume contribution) is not included. In order to survey the pressure effects in this transition, enthalpy was calculated on the same transition pathway (Fig. 4.34). At 30 GPa, compressed α-quartz needs to overcome an energy equal to 1.05 k_BT (at 300K). It is evident from the calculation that the free energy barrier disappears when the pressure reaches the critical value of ~49 GPa. Such a phase transition can be directly observed in *ab* initio MD simulations at 300 K.

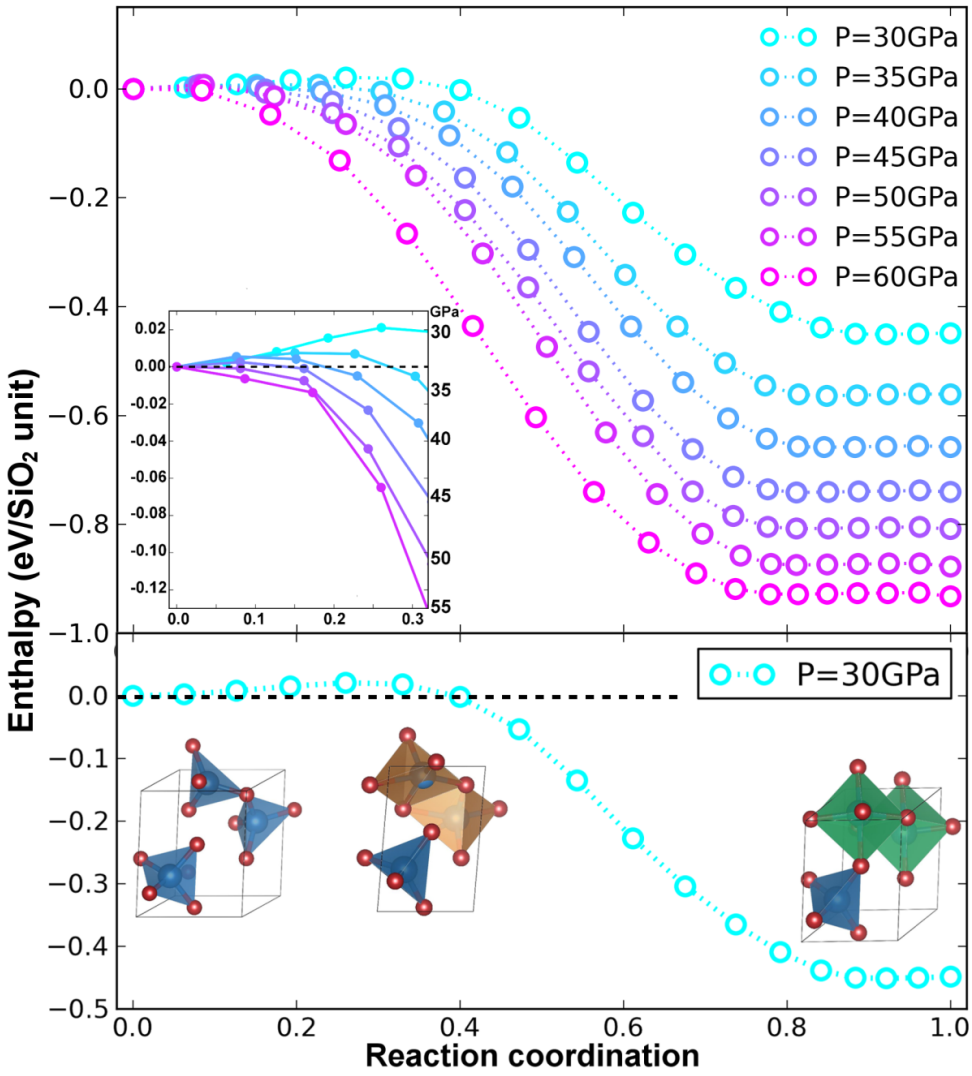

Figure 4.34. The enthalpy values on the transition pathway from the α-quartz phase to the quartz III phase calculated by the ssNEB method. The inset in the figure shows the decrease of the enthalpy barrier from 30~55 GPa, where above 50 GPa the energy barrier vanishes, and α-quartz spontaneously transforms to the quartz III phase. The results coincide with the phonon-instability rationale illustrated in the text. The lower panel shows the structural changes along the transition pathway. The initial and final structures are α-quartz and quartz III respectively. The middle snapshot was taken from the saddle point of the transition path at 30 GPa, where two silicon atoms in the unit cell are five-coordinated.

4.5 Conclusion and discussion

In summary, densification of silica can follow multiple transition pathways, greatly affected by its pressurization conditions. The transition from α-quartz to monoclinic post-stishovite is clarified by the single-crystal X-ray diffraction experiments and simulation, where pressure is applied relatively slowly. Such a slow compression process leads to an intermediate quartz II phase as a structural intermediate. If this transition is thermodynamically prohibited, *i.e.* by fast loading or compressing α-quartz at very low temperatures, our first-principles MD supports the existence of a new quartz III phase above 49 GPa.

Mechanism-wise, it is demonstrated that the two above-mentioned transitions are controlled by distinct transition mechanisms: a reconstructive transition pathway from α-quartz to monoclinic post-stishovite involving an intermediate phase, as opposed to a displacive transition from α-quartz to a new quartz III phase induced by phonon instability. The ultimate pressure limit for the existence of α-quartz is predicted to be 49 GPa. The new high-pressure phases discovered in this work are among the many possible polymorphs of silica, whose polyhedra building blocks are arranged in unique patterns that would require specific pathways to achieve. Such competing mechanisms may be operative simultaneously under certain experimental conditions and may give rise to complicated phase behaviors as seen in previous experimental works. Our findings point to the fact that, akin to the superheating limit of crystals[35], solid-state transformation under high pressure follows a succession of structural stability limits arising from thermodynamic, kinetic and mechanical considerations, resulting in a hierarchy of

structural transition pathways, which is believed to be common to a wide range of crystals with relatively open structures.

REFERENCES

1 Dera, P., *et. al.* High pressure single-crystal micro X-ray diffraction analysis with GSE_ADA/RSV software. *High Pressure Res.* 33, 466-484 (2013)

2 Kingma, K. J., R. J. Hemley, H. K. Mao & D. R. Veblen, New high-pressure transformation in alpha-quartz, *Phys. Rev. Lett.*, **70**, 3927-3930 (1993)

3 Campañá, C. Müser, H. M., Tse. J. S. & Schöffel D. H. Pressure-induced phase transition of quartz and the relation between the three hypothetical post-quartz phases. *Phys. Rev. B* **70**, 224101 (2004)

4 Choudhury, N. & Chaplot, S. L. *Ab inito* studies of phonon softening and high-pressure phase transition of α-quartz SiO_2. *Phys. Rev. B* **73**, 094304 (2006)

5 Holland, T. J. B. & Redfern, S. A. T. UNITCELL: a nonlinear least-squares program for cell-parameter refinement and implementing regression and deletion diagnostics. *J. Appl. Cryst*. **30**, 84 (1997)

6 Kawai, N. & Endo, S. The generation of ultrahigh hydrostatic pressures by a split sphere apparatus. *Rev. Sci. Instrum.* **41**, 1178-1181 (1970)

7 Giannozzi P., *et. al*. QUANTUM ESPRESSO: a modular and open-source software project for quantum simulations of materials. *J. Phys. Condens. Matter.* **21**, 395502 (2009).

8 Lee, C., Yang, W., & Parr, R. G. Development of the Colle-Salvetti correlation-energy formula into a functional of the electron density. *Phys. Rev. B,* **37**, 785. (1988).

9 Becke, A. D. Density-functional thermochemistry. III. The role of exact exchange. *J. Chem. Phys.* **98**, 5648 (1993).

10 Perdew, J. P., *et al*. Erratum: Atoms, molecules, solids, and surfaces: Applications of the generalized gradient approximation for exchange and correlation. *Phys. Rev. B* **48**, 4978 (1993).

11 G. Kresse & D. Joubert. From ultrasoft pseudopotentials to the projector augmented-wave method. *Phys. Rev. B* **59**, 1758 (1999).

12 G. Kresse & J. Furthmüller. Efficiency of *ab*-initio total energy calculations for metals and semiconductors using a plane-wave basis set. *Comput. Mat. Sci.* **6**, 15 (1996).

13 Paier, M., Marsman, K., Hummer, G., Kresse, I. C. & Gerber, J. G. Ángyán, Screened hybrid density functionals applied to solids. *J. Chem. Phys.* **124**, 154709 (2006).

14 Demuth. Th., Jeanvoine, Y., Hafner, J. & Ángyán, J. G. Polymorphism in silica studied in the local density and generalized-gradient approximations. *J. Phys.: Condens. Matter* **11**, 3833 (1999).

15 Levin, L., Prewitt, C. T. & Weidner, D. J. Structure and elastic properties of quartz at pressure. *Am. Mineral.* **65**, 920 (1980).

16 Holm, J. L., Kleppa, O. J. & Westrum, E. F. Thermodynamics of polymorphic transformations in silica. Thermal properties from 5 to 1070 °K and pressure-temperature stability fields for coesite and stishovite. *Geochim. Cosmochim. Acta.* **31**, 2289-2307 (1967).

17 Akaogi, M & Navrotsky. A, Calorimetric study of high-pressure polymorphs of $MnSiO_3$. *Phys. Earth. Planet. Inter.* **36**, 124 (1984).

18 Hamman, D. R. Generalized gradient theory for silica phase transitions. *Phys. Rev. Lett.* **74**, 660-663 (1996).

19 Andrault, D., Fiquet, G. F, Guyot, F. & Hanfland, M. Pressure-induced Landau-type transition in stishovite. *Science* **282**, 720-724 (1998).

20 Miyahara, M., *et al*. Discovery of seifertite in a shocked lunar meteorite. *Nat. Commun.* **4**, 1737 (2013).

21 Dove, M. T. *Introduction to lattice dynamics.* Ch. 5, (Cambridge University Press, New York, 2010).

22 Andreoni, W. & Curioni, A. New advances in chemistry and materials science with CPMD and parallel computing. *Parallel Comput*. **26**, 819-842 (2000).

23 Martyna, G. K., Klein, M. L. & Tuckerman, M. Nosé-Hoover chains: the canonical ensemble via continuous dynamics. *J. Chem. Phys.* **97**, 2635-2643. (1992).

24 Ensing, B., Laio, A., Parrinello, M. & Klein, M. L., A recipe for the computation of the free energy barrier and the lowest free energy path of concerted reactions. *J. Phys. Chem. B* **109**, 6676-6687 (2005).

25 Born. M. & Oppenheimer. R. Zur quantentheorie der molekeln. *Annalen der Physik (IV. Folge)*, **84**, 457-484 (1927).

26 Car. R. & Parrinello. M. Unified approach for molecular dynamics and density-functional theory. *Phys. Rev. Lett.* **55**, 2471-2474 (1985).

27 Mermin. N. D. What's wrong with this Lagramgean? *Phys. Today* **41**, 9 (1988).

28 Martyna G. J., Tobias D. J. & Llein M. L. Constant pressure molecular dynamics algorithms. *J. Chem. Phys*. **101**, 4177 (1994).

29 Chelikowsky, J. R., King, Jr. H. E., Troullier, JN., Marins, J. L., & Glinnemann, J. Structural properties of α-quartz near the amorphous transition. *Phys. Rev. Lett.* **65**, 3309 (1990).

30 Tse, T. S. & Klug, D. D. Mechanical stability of quartz: A molecular-dynamics study. *Phys. Rev. Lett.* **67**, 3559-3562 (1991).

31 Hazen, R. M., Finger, L. W., Hemley, R. J., & Mao, H-K, High-pressure crystal chemistry and amorphization of α-quartz. *Solid State Commun.* **72**, 507. (1989).

32 Gonze, X., Allan, D. C. & Teter, M. P. Dielectric tensor, effective charges, and phonons in α-quartz by vibrational density-functional perturbation theory. *Phys. Rev. Lett.* **68**, 3603 (1992).

33 Choudhury, N. & Chaplot, S. L. *Ab initio* studies of phonon softening and high-pressure phase transitions of α-quartz SiO_2. *Phys. Rev. B* **73**, 094304 (2006).

34 Sheppard, D., Terrell, R. & Henkelman, G. Optimization methods for finding minimum energy paths, *J. Chem. Phys.* **128**, 134106 (2008).

35 Tallon, J.L. A hierarchy of catastrophes as a succession of stability limits for the crystalline state. *Nature* **342**, 658 - 660 (1989).

BIOGRAPHY

Qingyang Hu graduated from Hangzhou Senior Middle School, Hangzhou, Zhejiang Province, China in 2005. He received his Bachelor of Science from Beijing Jiaotong University, Beijing, China in 2009. He received his Master of Science in Computational Science from George Mason University in 2013.